

Laser Generation and Applications of Micron and Submicron Scale Features on Metals

A thesis submitted to The University of Manchester for the degree of

Doctor of Philosophy

In the Faculty of Materials Science

2010

Robert William Lloyd

School of Materials

Corrosion and Protection Centre

Declaration

No portion of the work referred to in this thesis has been submitted in support of an application for another degree or qualification of this or any other university or other institute of learning.

Copyright Statement

i. The author of this thesis (including any appendices and/or schedules to this thesis) owns any copyright in it (the “Copyright”) and she has given The University of Manchester the right to use such Copyright for any administrative, promotional, educational and/or teaching purposes.

ii. Copies of this thesis, either in full or in extracts, may be made **only** in accordance with the regulations of the John Rylands University Library of Manchester. Details of these regulations may be obtained from the Librarian. This page must form part of any such copies made.

iii. The ownership of any patents, designs, trade marks and any and all other intellectual property rights except for the Copyright (the “Intellectual Property Rights”) and any reproductions of copyright works, for example graphs and tables (“Reproductions”), which may be described in this thesis, may not be owned by the author and may be owned by third parties. Such Intellectual Property Rights and Reproductions cannot and must not be made available for use without the prior written permission of the owner(s) of the relevant Intellectual Property Rights and/or Reproductions.

iv. Further information on the conditions under which disclosure, publication and exploitation of this thesis, the Copyright and any Intellectual Property Rights and/or Reproductions described in it may take place is available from the Head of School of Materials (or the Vice-President) and the Dean of the Faculty of Life Sciences, for Faculty of Life Sciences’ candidates.

Acknowledgements

For giving me the opportunity to pursue a PhD, I would firstly like to thank my Supervisor, Dr. Zhu Liu as well as the powers that be at the EPSRC who approved and funded the project. For taking me under their wing and guiding me throughout my time in Manchester, I would like to thank Amin Abdolvand, Dave Whitehead and Marc Schmidt. Their expertise and mentorship has been invaluable from start to finish. I would also especially like to thank Greg Chabrol, Ana Pena and Med BenYezzar for their friendship and intelligent conversation during this time and in the future. This is not to say that these are the only people to whom I am grateful. Completing this PhD would not have been possible without the help of countless mentors, colleagues, family, housemates and friends. I thank you all. Most of all I owe my thanks to my Mum and Dad. They have encouraged me in everything I do.

ABSTRACT

This thesis describes the formation of and applications of self-assembled structures on metals. Primarily the focus of this PhD project is on the formation of surface structures on stainless steel (AISI 304) but other metals have been studied. Laser generated surface structures have been applied to the modification of wettability and reflectivity with a view towards developing these processes for industrial applications. Compared to conventional techniques for the modification of wettability, lasers offer the advantage of being a relatively simple technique for the modification of surface structure, reducing the need for complex processes. It is hoped that investigations into the reduction of surface reflectivity will have applications in the conversion of solar energy into useable power in the form of solar thermal energy.

The production of self assembled structures is demonstrated using diode pumped solid state (DPSS) Nd:YVO₄ lasers operating at wavelengths of 532 and 1064 nm. It is shown that the production of surface microstructures is highly dependant on the correct laser fluence and requires multiple pulses and processing passes. At 1064 nm wavelengths, it has been found highly reproducible surface structures can be formed by carefully controlling laser fluence and scanning speed while keeping the optical arrangement relatively simple. In addition to microstructure formation, the use of ultrafast femtosecond lasers, operating at 400 and 800 nm wavelengths has verified the production of laser induced periodic surface structures. Additionally, the stationary method used to produce these surfaces has been adapted to cover large surface areas with sub wavelength ripple structures with periods of ~295nm and 600nm.

Applications of laser surface microstructures on metals have been studied in an effort to produce hydrophobic and superhydrophobic surfaces on metals. It has been found that the roughness change produced by laser processing induces composite wetting when water droplets are introduced to the surface. Contact angle measurements and small angle XRD analysis of laser processed stainless steel (AISI 304) have shown that surface wettability decreased over a period of approximately one month, leading to steady contact angles of over 140° . This is attributed to the formation of a magnetite (Fe_3O_4) oxide layer in the period after laser processing.

The effect of surface microstructure on surface reflectivity has also been studied. It was found that laser induced surface microstructures on copper can decrease surface reflectivity by almost 90%. A comparative study of the effects of surface roughness and chemistry on the optical absorption of copper is given, finding that these surfaces are competitive with contemporary coatings.

1	Introduction	1
1.1	The Research Project	1
1.2	This Thesis	3
2	Literature Review	5
2.1	Introduction	5
2.2	The Laser	6
2.3	Characteristics of Laser Light	11
2.3.1	Divergence	15
2.3.2	M^2 and Beam Quality	16
2.3.3	Pulse Duration	17
2.3.4	Energy and Power of Lasers	18
2.4	Gaussian Beam Optics	19
2.5	Laser Interaction with Materials	21
2.5.1	The Effects of laser Heating	26
2.5.2	Laser Heating	26
2.5.3	Laser Melting	27
2.5.4	Laser Vaporization (Ablation)	27

2.5.5	Ablation Threshold	28
2.6	Review of Laser Surface Topography Modification	30
2.6.1	Self Assembly Methods of Laser Surface Topography Modification	33
2.6.2	Producing sub-micron features using interference	37
3	General Methods	40
3.1	Laser Control and Processing	40
3.2	Analysis Tools	43
3.2.1	Microscopy	43
3.2.2	Scanning Electron Microscopy	45
3.2.3	MEX	47
3.2.4	White Light Interferometry	50
3.2.5	Goniometry	52
3.2.6	Spectrophotometry	53
3.2.7	X-Ray Diffraction.	55
4	Laser Generation of Surface Structures	57
4.1	Experimental Methods	57
4.2	Laser Micro-topography Modification using 532 nm Violino Green Marker	59

4.2.1	Comparing Production of Microstructures in Gaseous and Liquid Environments.	60
4.2.2	Change in microstructure with increasing numbers of pulses in air	63
4.3	Laser Micro-topography Modification using 1064 nm EU Marker	68
4.3.1	Change of microstructure as scanning speed is changed.	68
4.3.2	Effect of average laser power on structure formation.	71
4.3.3	Influence of Hatch Distance on Structure Formation	73
4.3.4	The Effect of Different Laser Scanning Patterns	75
4.3.5	Production of angled structures on stainless steel	80
4.4	Laser Micro-topography Modification using Spectraphysics YHP40	87
4.4.1	The Effect of pulse duration on microstructure formation	87
4.5	Laser Processing using Coherent Libra Femtosecond Amplifier	90
4.5.1	Damage Thresholds of AISI 304 Stainless Steel under Femtosecond Irradiation	92
4.5.2	Microstructure Production using Femtosecond Lasers	94
4.5.3	Production of Sub-Wavelength Structures using Femtosecond Lasers	101
4.5.4	Sub-wavelength features over large areas.	103
4.6	Surface Structure Formation Mechanisms	107

4.6.1	One dimensional heat flow model	107
4.7	Conclusions	110
5	Modification of Wettability	113
5.1	Contact Angles and Wettability	113
5.1.1	Wetting on rough surfaces	116
5.1.2	Contact Angle Hysterisis	120
5.2	The Lotus Effect	122
5.2.1	Physical Basis of the Lotus Effect	122
5.2.2	How and Why the Lotus Leaf is Self Cleaning	123
5.2.3	The breakdown of the lotus effect.	124
5.2.4	Artificial Low Wettability Surfaces.	125
5.3	General Experimental Methods	126
5.4	The effect of Laser Scan Speed the Total Number of Pulses Applied	126
5.5	Development of Contact Angles Over Long Time Periods	129
5.6	Contact Angles of Angled Structures	132
5.7	Conclusions	134
6	Modification of Surface Reflectivity	136

6.1	Introduction	136
6.2	Reflectivity of Laser Processed Stainless Steel and Copper.	138
6.3	Preparation and Characterisation of Surface Microstructures for Solar Energy Harvesting	142
6.3.1	Introduction	142
6.3.2	Experimental	142
6.3.3	Reflectivity of Surfaces	145
6.3.4	Identification of oxide species.	148
6.3.5	Surface Roughness	150
6.3.6	Back Reflection	152
6.3.7	Heating of Samples by White Light.	153
6.3.8	Conclusions	154
7	Conclusions	156
8	Future Work	162
	References	165
	Appendix A: Publications	174

Figure 2.1. Stimulated emission for an atom with two energy levels (Adapted from [32]).	8
Figure 2.2. Simplified Schematic of a laser resonator	10
Figure 2.3 The Electromagnetic Spectrum [35]	12
Figure 2.4. Transverse Electromagnetic (TEM) modes which can be present in a laser resonator [39].	14
Figure 2.5. Graph to show the irradiance profile of a Gaussian beam (Adapted from [36]).	15
Figure 2.6. The measurement of an embedded (theoretical) Gaussian beam in comparison to a real beam.	17
Figure 2.7. Usually, pulse durations are measured as the temporal pulse width at half of the peak value.	18
Figure 2.8. Common terms used to describe various features of laser pulses.	18
Figure 2.9 The reflectivity of Aluminium, Nickel, Copper and Steel over a range of laser wavelengths [11].	23
Figure 2.10 Schematic of depths below a target surface where optical absorption and heat diffusion processes are present.	25
Figure 2.11 a) large absorption coefficient, α_1 , with high volumetric energy loading, (b) small absorption coefficient, α_2 , with small volumetric energy loading. This assumes the same input fluence.	29

Figure 2.12. Examples of direct writing of micro-features on metals using Gaussian beams [13].	31
Figure 2.13 Microstructures ablated in polymers by static mask projection	32
Figure 2.14. Microchannels produced with (a) a triangle mask, (b) a 'T'-shaped mask	32
Figure 2.15. Polyimide after machining with a KrF (248nm) laser [65]	34
Figure 2.16. Brass in Ethanol And Water. Nd:YAG (1064nm), ~16 J/cm ² , >10 ⁴ Pulses, Spot Size ~40μm. Scale bar 100μm [58].	35
Figure 2.17. Single Crystal Ge in Vacuum, Cu Vapour (510.6nm), $\tau = 20\text{ns}$, ~1J/cm ² , 10 ⁴ Pulses. Spot Size ~ 40μm [58]	35
Figure 2.18. An example of the types of surface topography that can be created using Surfi-Sculpt [®] . Scale bars 200μm (A) and 1mm (B)	36
Figure 2.19. Examples of surfaces produced using interferometry. The three figures show structures formed using two beam interferometry (A) [68] and three beam interferometry (B and C). The difference between structures seen in B and C [12] [69] are due to differing interference geometries.	37
Figure 2.20. Scanning electron micrograph of an array of microfeatures etched in N-BK7 glass using an F ₂ laser beam after propagation through a transmission mask [71]	38
Figure 2.21. Demonstrations of LIPSS formed within the confined of a laser spot. It can be seen from both figure a and b that structures form perpendicular to beam polarization (indicated) and have almost the same period. [84].	39

Figure 3.1 Schematic of a scanning head	41
Figure 3.2 Three Axis Aerotech stage with focusing optics and target holder	42
Figure 3.3 Arrangement of an optical microscope	44
Figure 3.4 Arrangement of a Scanning Electron Microscope (SEM)	46
Figure 3.5 Orientation of samples needed for the production of MEX digital electronic models.	48
Figure 3.6 An example of a digital electronic model (DEM) created in MEX [®] (bottom) using three source images similar to the SEM image shown (top) .	49
Figure 3.7 (a) Annotated photograph of the Wyko NT1100 (b) schematic diagram of the inside of (a), both taken from the Wyko techniques manual .[85]	50
Figure 3.8. Arrangement of sessile drop contact angle measurements using a video tensiometer.	52
Figure 3.9. Schematic diagram of a single beam spectrophotometer	53
Figure 3.10 Schematic of an integrating sphere which	54
Figure 4.1 The enclosure which houses the Violino Marking System	59
Figure 4.2. Stainless Steel machined in a) Ethanol and water b) Air	61
Figure 4.3. Structures produced in water (A) and Air (B). In these images, the scale bars are 20 and 50 μ m respectively. This change in feature size is related to the environment	

in which the surface is processed. Indeed this is believed to be the case when discussing the orientation of features also. 62

Figure 4.4. Scanning electron microscopy (SEM) images (view tilt 45°) of the target sites where the number of pulses per spot, N_T , have been changed (laser wavelength 532 nm, intensity 1.5 GW/cm², beam spot diameter $\sim 50\mu\text{m}$, distance between the subsequent lines $\sim 25\mu\text{m}$). From top to bottom, N_T is (a) 10500, (b) 7500, (c) 4500, and (d) 1500, with average tip-to-tip distance of 50, 41, 35, and 30 μm , respectively. Inset (e)—view tilt 75° is the enlarged part of the Fig. 5.04a. Exposed areas look like black regions on a bright steel surface 64

Figure 4.5 SEM Image of microstructures formed in Air when $N_T=10500$. This Image illustrates the position of structures below the datum of the surface. Scale bar $50\mu\text{m}$. 65

Figure 4.6 SEM images showing the evolution of surface microstructures over nine passes (A – H) with each pass being its own image. The surface is viewed at an angle of 45° 66

Figure 4.7 SEM image of the surface resulting from approximately 15000 pulses per spot being fired in a raster scanned pattern at a fluence of 3.93 Jcm^{-2} 67

Figure 4.8 a-f. Development of Microstructures as 5000 pulses are deposited onto Stainless steel as the laser scan speed is increased. Left to right, top to bottom, 1, 5, 10, 20, 40, 60mm/s. Scale Bars $50\mu\text{m}$ 69

Figure 4.9 Development of Microstructures as 5000 pulses are deposited onto Titanium as the laser scan speed is increased. Scanning speeds A – F are 1, 5, 10, 20, 40, 60mm/s respectively. Scale Bars $50\mu\text{m}$ 70

Figure 4.10 A-F, Samples of stainless steel raster scanned at average powers of 0.67, 1.06, 1.84, 2.62, 3.40 and 4.18W. Scale Bar 200 μ m	72
Figure 4.11. Diagram to show the meaning of the hatch distance, d.	73
Figure 4.12 Development of Microstructures as 2500 pulses are deposited onto stainless steel as the hatch distance, d, between scan lines is increased. A – G d = 10,20,30,40,50,60 μ m respectively. Scale Bars 50 μ m	74
Figure 4.13. Different Scanning patterns used to produce microstructures.	75
Figure 4.14 shows the results of the HLSR. Comparing (a) and (g), it is evident that increasing the hatch distance between the consequent lines, from 10 μ m to 70 μ m, resulted in much lower ablation. (e), (f) and (g) represent the situation where there were no overlaps between the scanned lines. In these pictures ablation of the material in the scanned path can be clearly seen.	77
Figure 4.15 The results of processing in the cross hatched regime. As with the HLSR surfaces, above hatch distances of 20 μ m, the period of structures correlates to the hatch distance. Voids at the centre of structures in F & G are because no overlap occurs between scan lines in either direction.	78
Figure 4.16 Schematic of experimental arrangement to show the change in shape and area of focal spot size as a target sample is tilted by angle θ .	80
Figure 4.17 Angled Microstructures on stainless steel produced using the line scanning method. Left to right, samples tilted by 15, 30 and 45 degrees. Scale Bars 50 μ m	82

-
- Figure 4.18 Angled Microstructures on stainless steel produced using the cross hatching method. Left to right, samples tilted by 15, 30 and 45 degrees. In all cases the hatch distance is 70 μ m. Scale Bars 50 μ m 83
- Figure 4.19 Angular dependence of focal spot fluence for target tilt angles between 0 and 90 degrees. 85
- Figure 4.20. SEM images of Stainless steel targets processed using the Nd:YAG Laser. Fluence is varied from 53 Jcm⁻² (a) to 15 Jcm⁻² (h) in increments of 5 Jcm⁻². 88
- Figure 4.21 Overview of Coherent Libra Ti:Sapphire femtosecond laser system. Two lasers, the Vitesse and Evolution provide the source and pump beams respectively. The regenerative amplifier and stretcher compressor then manipulate these outputs into femtosecond output. 91
- Figure 4.22. Schematic of the Stretcher/Compressor module shown in Figure 4.21. Ultrashort pulses are achieved using this chirped pulse amplification method in the Coherent Libra System. 91
- Figure 4.23 Ablation depth per pulse relationship for AISI 304 Stainless steel during femtosecond ablation at 40 and 800 nm. 94
- Figure 4.24. Stainless steel targets after ~50, 100 and 150 pulses have been fired a) to c) respectively. Both microstructure and nanostructure are present within the laser spot diameter. 95
- Figure 4.25. Structures produced after 1 pass at scan speeds of 1,2,3 and 4 mm/s. These can be seen in a) to d) respectively. 97
-

Figure 4.26. Structures produced after 2 passes at scan speeds of 1,2,3 and 4 mm/s. These can be seen in a) to d) respectively.	98
Figure 4.27. Structures produced after 3 passes at scan speeds of 1,2,3 and 4 mm/s. These can be seen in a) to d) respectively.	99
Figure 4.28. Structures produced after 4 passes at scan speeds of 1,2,3 and 4 mm/s. These can be seen in a) to d) respectively.	99
Figure 4.29 The effect of femtosecond laser processing after ten pulses at fluences of 4.06Jcm^{-2} (a) and 0.09Jcm^{-2} (b)	101
Figure 4.30 Example of laser induced periodic surface structures (LIPSS) produced using an 800nm femtosecond laser at an average power of 8mW and twenty applied pulses.	102
Figure 4.31 Profile of ablation crater obtained using white light interferometry	102
Figure 4.32. Mean period of LIPSS generated using 800nm femtosecond light.	103
Figure 4.33 Laser induced periodic surface structures formed by translating a stainless steel sample with a speed of 1mm/s at a fluence of 0.022Jcm^{-2}	104
Figure 4.34 Laser induced periodic surface structures formed at 1mm/s and a fluence of 0.001Jcm^{-2} . Structure period is found to be $\sim 295\text{nm}$	105
Figure 4.35. Laser induced periodic surface structures formed by the superposition of two processing passes. Importantly, during the second pass, initial structures are not destroyed at the edges of the beam path.	106

Figure 4.36. Change of surface temperature with time of stainless steel surfaces subjected to 7ns pulses of laser radiation at 532 and 1064nm	109
Figure 5.1. Three regimes of contact angles when a droplet is formed on a surface.	114
Figure 5.2. Interfacial forces acting on a liquid droplet at rest on a surface.	115
Figure 5.3. Water droplet at rest under the assumptions of Wenzel, left and Cassie and Baxter, right.	117
Figure 5.4. Comparison of contact angle values from the theoretical work of Wenzel (a) and Cassie-Baxter Theories (b)	118
Figure 5.5. Advancing and receding contact angles of a liquid droplet on an inclined surface.	120
Figure 5.6. Advancing and receding contact angles on rough surfaces [106].	121
Figure 5.7 a) SEM image of the surface structure of a lotus leaf (right). b) Photograph of liquid droplets at rest on a lotus leaf (left)[108].	123
Figure 5.8. Schematic of the way in which particles are removed from super-hydrophobic surfaces by liquid droplets [4]	124
Figure 5.9. Graph to show contact angle measurements as a function of laser scan speed at various numbers of pulses on microstructured stainless steel. Time between laser processing and contact angle measurement, 15 days	128

Figure 5.10. Graph to show contact angle measurements as a function of laser scan speed at various numbers of pulses on microstructured titanium. Time between laser processing and contact angle measurement, 14 days	128
Figure 5.11. Graph to show the increase and development of contact angle measurement on laser textured stainless steel over long time periods in comparison to an untreated sample. The structured sample was processed at a fluence of 3.6Jcm^{-2} . Approximately 10^3 pulses were applied per spot during four processing passes at a speed of 10mm/s .	129
Figure 5.12. XRD data of a laser processed Stainless steel sample after a three month period	131
Figure 5.13. Contact Angles of Angled structures on stainless steel. Insert; Visualisation of Surface structure and viewpoints.	133
Figure 6.1. Visualization of specular and diffuse reflectivity [96]	136
Figure 6.2 Beam paths of light rays incident onto three cavity shapes at normal incidence.	137
Figure 6.3 Stainless steel surface after one pass has been made in an effort to modify reflectivity. Inset: The same surface at higher magnification. Due to the low number of pulses used, only a periodic trough and peak structure can be seen.	139
Figure 6.4 Copper surface after three passes have been made in an effort to modify reflectivity. Inset: The same surface at higher magnification. As the number of passes increases, more individual structures begin to develop	139

Figure 6.5. Diffuse and specular reflectivity spectra of reference and a laser processed (fig.3.21) stainless steel surface. Reflectivity is reduced by upto 45%. Diffuse and specular reflectivity are almost identical post processing due to high roughness of microstructure. 140

Figure 6.6. Diffuse and specular reflectivity spectra of reference and a laser processed (fig.3.22) copper surface. Most interesting in this case is the reduction in reflectivity at wavelengths about 600nm. In this region most of the energy which would otherwise be reflected is absorbed by the sample. 140

Figure 6.7. Arrangement of equipment used to measure thermal response. Temperature was measured using a K-type thermocouple attached to the back of the 0.8mm thick sample. Back-reflected light was measured from an arbitrary point. The temperature data was captured using a Keithley Instruments 2701 digital multimeter equipped with a M7706 data acquisition module. 144

Figure 6.8. A comparison of the output of the artificial light source used and optical solar radiation. The output spectra of these sources have been normalised. The loss of spectral data in the UV wavelengths (<400nm) for solar radiation is due to the attenuation of these wavelengths by an optical filter which was a necessary part of the experimental arrangement. 144

Figure 6.9. Reflectivity spectra of four samples shows overall a decrease in reflectivity before and after processing. This was observed at a translation speed of 5mm/s, in Air and Argon atmospheres. The samples processed in air exhibit a fairly similar absorption to those coated with a carbon based black coating (Carbon Black) 146

-
- Figure 6.10. SEM Micrographs of Copper surfaces processed under air (A) and Argon (B) atmospheres. The same parameters, 5mm/s, 7.4 J/cm^{-2} are used to produce each. Differences in surface structure occur due to oxide formation between processing passes. 147
- Figure 6.11 XRD data from copper samples processed in an atmosphere of Air. 149
- Figure 6.12 XRD data from the analysis of Copper samples which have been laser processed in an Argon atmosphere. 150
- Figure 6.13. The surface roughness ratio of samples processed in Air (left), that is the ratio between the projected and true surface areas, is generally lower than those processed in Argon (right). This is due to the formation of an oxide layer after the first processing pass, leading to the occurrence of more surface heating and less ablation. 151
- Figure 6.14. As the translation speed increases, it can be seen that the difference in relative backreflections are more pronounced in air than in an argon atmosphere. The light reflected from laser processed surfaces gives a good indication that the presence of an oxide layer improves absorption over the whole spectrum. 152
- Figure 6.15 Thermal energy of various copper samples in response to an optical impulse. 153

1 INTRODUCTION

1.1 The Research Project

The need for surfaces that have properties differing from those which occur at the time of initial manufacture can greatly enhance their usefulness in the modern world. More and more often in recent times, scientists have taken their inspiration for new surfaces from biology [1, 2]. Mimicking biology, biomimetics, is not a new concept [3]. However, as scientific investigation increases our understanding of how nature performs such feats of engineering, our ability to replicate these natural technologies with man made materials, structures and devices must keep pace.

One particular example of a remarkable natural surface is that of the lotus plant [2]. Thriving in muddy environments, the lotus plant, *Nelumbo nucifera*, has developed self cleaning leaf surfaces [4]. These surfaces display a contact angle with water of over 160° , allowing water droplets to roll off their surface rather than slide. This property is advantageous because dirt and debris is removed from the surface. The reason for this increase in water repellent, or superhydrophobicity, is as a result of the double scale roughness with both micron and sub-micron features present [5].

To produce these new materials, new technology has also had to be developed. When interest in the fabrication of these new surfaces began the adaptation of many techniques was carried out. Chemical etching [6], plasma etching [7, 8] and moulding [9] of surfaces have all had impressive results. Unfortunately, many of these techniques are reliant on technologies which involve vacuum chambers, large amounts of chemical

processing and cleaning. Although this is not abhorrent, it would be preferable if other tools and techniques could be found which simplify the production of such surfaces. The laser is one technology which falls into this category. Developed in the last fifty years [10], for the past thirty it has been used as a tool for the marking and cutting of materials [11]. One of the advantages of this technology, with the aid of computer control and automation, is that a surface can be modified with a high degree of accuracy and with little or no excess equipment needed.

This project deals with the production and applications of micro and nano scale topographies which are produced using lasers. Various methods already exist for the production of micron scale surface topography on metals [12, 13] but these are mainly reductive methods. More recent developments have shown that it is possible to produce self organised structures on metals using lasers [14-17] that remove less material from surfaces and produce modified topography at the same level or above the original surface. Additionally the development of work already published on the formation of sub-wavelength nanostructures [15, 18, 19] is also developed to cover large areas on metals.

This project is primarily focused on stainless steel (AISI 304) and copper. Although many attributes of these newly formed surfaces could be investigated those chosen to be concentrated on were the modification of the wettability and reflectivity of the surfaces. On the modification of wettability, an effort has been made to produce surfaces with properties similar to that of the lotus leaves. In addition to this application, it is also shown that it is possible to increase the amount of light which is absorbed by copper

surfaces by laser processing. This is done in an effort to produce new surfaces to aid in the harvesting of energy from solar radiation

1.2 This Thesis

This thesis is structured in a way so that the reader will have a good knowledge of the subject matter before new experiments and observations are introduced. In chapter two, a review of previous literature on the subjects of lasers and their use as tools for surface topography modification is discussed. Other literature specific to individual applications of the surfaces which are produced by this project are given attention in the chapters relating to that work. Attention has been paid to the physical principles of lasers and laser processing.

To understand the changes which are brought about by laser processing, the various analysis tools and techniques which this project utilises are introduced in chapter three. Although many of these techniques are standard scientific tools some new techniques are included which warrant discussion.

Chapter four embodies the work which is central to this project. Beginning with experiments which evaluate the previous work done in the field of laser generated, self assembled topography on metals, this chapter goes on to describe experimental results from experiments on the formation of various micron and sub-micron structures. The mechanisms of formation are discussed and new surfaces are introduced. The majority of the work will be dealing with diode pumped solid state lasers [11, 20, 21]. Also the use of ultrashort laser pulses has been shown to be a attractive option for high quality micromachining of many materials and their ability for minimal damage and precise

processing has been researched for a number of years [22-24]. The later part of Chapter 4 describes ultrashort laser interactions to form microstructures and nanostructures

Chapter five begins with a discussion of the modification of wettability on rough surfaces. This is done to give the reader an insight into the current status of the subject and discuss the methods by which surfaces can be engineered to modify their wettability. Continuing from this, results are given describing how the laser processed structures produced in chapter four can modify the wettability of metallic surfaces.

Chapter six describes the application of laser generated structures for the modification of bulk reflectivity of stainless steel and copper. Here, special attention has been paid to the effect that increased absorption of light has on the heating of surfaces. This is done through the use of a light source acting as an analogue for solar radiation. It is hoped that this type of surface may find a use in the harvesting of energy from solar radiation.

Chapter seven is the conclusion of this PhD thesis and contains a summary of all results found, linking together the work which makes up this project. This is followed by a short proposition of the future works which would further develop this project.

Finally, the general conclusions reached from this work and possible additional application of microstructures and nanostructures surfaces are discussed in Chapter 8.

2 LITERATURE REVIEW

2.1 Introduction

This literature review will discuss the pertinent techniques and past progress in the field of lasers and laser processing. This is done to give the reader a full understanding of the generation of micron scale topography which will later be used to produce new structures on metals and modify the wettability and reflectivity of the surfaces. This project begins with the development of new surfaces and then explores the applications of these surfaces. To fully understand the methods by which structures are produced on metals, it is first necessary to discuss the tools with which these structures are formed. In this case, the laser.

Section 2.2 to 2.5 of this review concentrates on the theory and practice of laser processing. This is not a complete introduction to the theory of laser processing and micromachining but the contents of these sections are necessary for the complete understanding of this project. Section 2.6 is a review of laser surface topography modification techniques. This begins with more traditional techniques and moves on to previous work which has been reported on the formation of self-assembled micro and nanostructures on various materials using lasers.

To simplify the flow of this thesis, the two main applications of the surface structures produced by this project are discussed individually in their own chapters. Chapter five concentrates on modification of wettability and modification of reflectivity is discussed in Chapter six. This includes reviews of previous work reported in their subject areas.

2.2 The Laser

The first laser was built 50 years ago in 1960 [10]. Laser stands for *Light Amplification by Stimulated Emission of Radiation*. Today, lasers have become a mature technology and are at the heart of many new industrial processes. These processes range from communications to novelty toys and surgery to the measurement of gravitational waves [25]. The main benefits of laser interaction compared to other techniques are:

- Energy is delivered in a highly directional and precise beam of light, which leads to high resolution and accuracy.
- Lasers are non-contact and highly flexible
- Lasers have the ability to machine a wide range of materials and selectively ablate composite materials.
- Lasers have high processing speeds, which are needed for industrial applications.

In short the range of uses for lasers is diverse. In this chapter the underlying principles of lasers are discussed. Their inception in the early 20th century, the practical realities of building a laser and how the light produced can be controlled and utilised for laser processing applications.

There are several individuals who are responsible for the initial ideas and concepts that give rise to the laser, as we know it. The first of these is Max Planck [26]. In 1900 he discovered that light could be broken down theoretically into discrete quanta later to be called photons. These photons have a total energy;

$$E = h\nu$$

2.1

where h is Planck's constant ($h=6.626 \times 10^{-34}$ Js), an empirically derived value, and ν is the frequency of the light [27]. Together with Rutherford's model of the atom and Bohr's work on quantization of energy states [28], this theory showed that in a then imaginary laser resonator, only a finite number of frequencies would be allowed to propagate through a resonator. Unfortunately the method of producing the light within the resonator was still not understood. In 1917, Einstein [29] produced an elegant representation of a solid material surrounded by electromagnetic radiation. Einstein formulated this thought experiment as a way to confirm Planck's theory of discrete quanta.

At that time, the concept of spontaneous emission was understood. The first part of the spontaneous emission process is when a photon interacts with an atom. Here, the energy of the photon can be imparted to the atom in a discrete transaction, changing the configuration of the electron cloud and allowing an electron to sit in a higher orbit of the nucleus. For the atom to return to its stable configuration, the excess energy that the electron possesses must be shed somehow. This is done by the spontaneous emission of a photon.

For example, assuming the active medium contains atoms with only two possible quantum energy levels E_2 (higher) and E_1 (lower), then the incident radiation frequency must satisfy [30]:

$$E_2 - E_1 = \nu h$$

2.2

If this equation is satisfied then the lasing medium can absorb photons of energy, thus raising the energy of the atom from the ground state E_1 to the excited state E_2 . The excited atom exists in this excited state for a short limited time, before returning to the ground state via two different mechanisms. One way is via ‘spontaneous emission’ where the atom decays and emits a photon of wavelength, λ [30, 31]:

$$\lambda = \frac{hc}{E_2 - E_1} \quad 2.3$$

Where c is the velocity of light (2.99×10^8 m/s). Alternatively, stimulated emission can occur. Fortunately for the laser physicists of today, almost 50 years before the invention of the first working laser, Einstein took his thought experiment one step further and imagined what would happen if a photon was incident on an atom already in an excited state. This introduced the concept of stimulated emission [29]. If a photon with frequency, ν , interacts with the excited atom it may cause the atom to release a second photon with the same frequency, phase and polarisation as the first photon. This stimulated emission is illustrated in Figure 2.1.

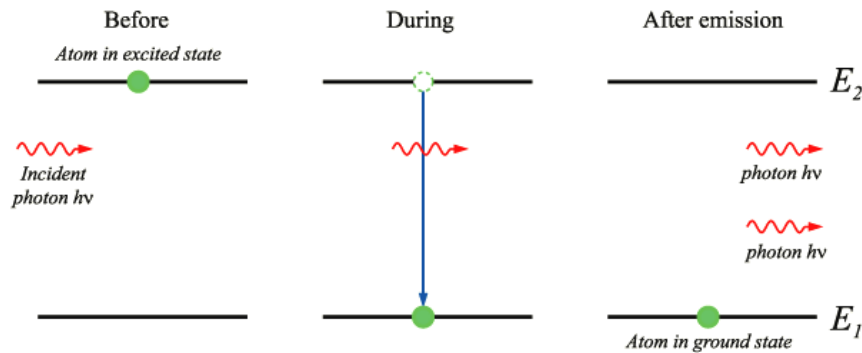


Figure 2.1. Stimulated emission for an atom with two energy levels (Adapted from [32]).

The previous example is based on an atom with only two energy levels. In reality, the atoms can be excited to a level that is two or three levels above the ground state. For the phenomenon of stimulated emission to be useful in a lasing device, the material in which the laser light is produced, the gain medium, must be so heavily saturated with electromagnetic radiation that a highly excited state called population inversion is brought about. Population inversion is most easily explained by thinking of its opposite, the ground state. When a gain medium is not under the influence of external excitation the majority of its electrons will be in there lower energy, ground state. Only a small percentage will be in higher orbits. The opposite of this is true for population inversion. Here, the majority of electrons are in higher orbits. This means that stimulated emission is the dominant process for releasing energy as the orbits of electrons decay. The population of electrons at any energy state can be described by the Boltzmann equation [28]:

$$\frac{N_2}{N_1} = \exp - \left(\frac{E_2 - E_1}{k_b T} \right) \quad 2.4$$

Where N_1, N_2 = electrons at energy states E_1 and E_2 respectively, T = absolute temperature of the medium, k_b = Boltzmann's constant ($1.38 \times 10^{-23} \text{ J K}^{-1}$). When N_2 is statistically greater than N_1 , this is known as population inversion. As the photon emitted through stimulated emission is identical to the incident one optical amplification can then occur.

Lasers have been in use as a scientific tool since the 1960's. The first laser, a pulsed Ruby laser operating at a wavelength of 694nm, was produced by Maiman et al [10]. The reason for a 40 year gap between the concept of a laser and its first incarnation is

that the laser is reliant on technologies which were themselves being developed. To utilise the quantum mechanical phenomenon of stimulated emission, other laser components are necessary. The following components are essential in a modern laser:

Lasing (active) material: A suitable active material must be present that provides appropriate energy levels for spontaneous and stimulated emission.

Energy Source: To achieve population inversion the atoms need to be ‘pumped’ to a higher energy level. This can be achieved by many methods (i.e. flash lamp pumping) depending on the type and power of the laser [33].

Resonant cavity: The resonant cavity or ‘resonator’ enables the optical amplification to occur. The resonator forms an optical oscillator using totally reflective and partially reflective mirrors [11]. The lasing material is situated on the optical axis between the mirrors and amplifies the light oscillations by stimulated emission. There are various configurations of resonator cavity [34] and a simplified diagram of a laser system can be seen in Figure 2.2.

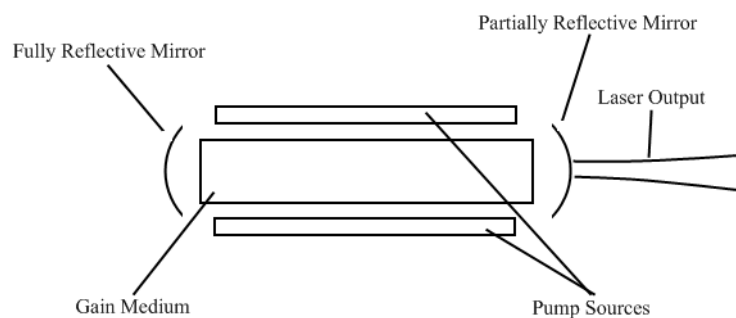


Figure 2.2. Simplified Schematic of a laser resonator

The main features of the laser resonator are the pump source, gain medium and the resonator, in the form of two mirrors. In most modern lasers, the resonator consists of

two mirrors. One of which is fully reflective and the other is only partially reflective. Other arrangements can be used, but they all rely on the same basic principles for operation.

2.3 Characteristics of Laser Light

Compared with other light sources, the unique characteristics of laser light enable it to be used for a vast number of applications. From medical applications to industrial material processing lasers are becoming an increasingly integral part of every day life. The name given to the continuum of wavelengths at which electromagnetic waves, variations in magnetic and electric fields, propagate is the electromagnetic spectrum. It ranges from high energy Gamma rays to the long frequency waves. The UV, visible and IR regions of this spectrum occupy only a small proportion of this spectrum. An illustration of the range of frequencies present in the electromagnetic spectrum can be seen in Figure 2.3.

The majority of laser systems operate in the ultraviolet (UV), visible and infrared (IR) region of the electromagnetic spectrum. Wavelengths are commonly measured in nanometers (10^{-9}m) or microns (10^{-6}m). The visible spectrum extends from approximately 400 – 700nm. Longer wavelengths, up to 1000 μm is considered the infrared region and is broken up into near infrared (0.7 - 2 μm), middle infrared (2-15 μm) and far infrared. Wavelengths shorter than 400nm are generally classified as ultraviolet. This region extends down to wavelengths of approximately 1nm. At this point, the energy of a photon is high enough for it to be considered as a soft X-ray [35].

These regions are not exact, however they serve as a useful approximation for transferring knowledge.

White light consists of a large range of wavelengths propagating in unison. Laser light is unique because only a discrete number of wavelengths are produced. The bandwidth or linewidth of a laser source is a measurement of how monochromatic the light that emerges from the resonator.

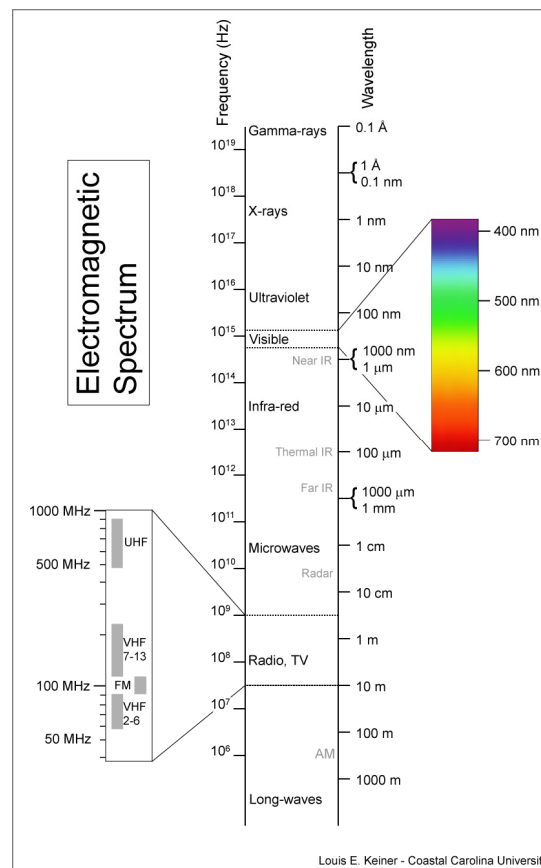


Figure 2.3 The Electromagnetic Spectrum [35]

Although lasers usually have their wavelengths quoted to nanometer resolution, this is usually the mean wavelength with a spread of wavelengths present to either side. As a rule of thumb, lasers with single mode outputs such as Gaussian beams usually have a small linewidth, multimode outputs such as excimer beams will have a larger linewidth.

The effect of this spread of wavelengths present in the output is noticed when the coherence of the beam is studied [36]. The two types of coherence in question are the temporal coherence, the time period over which the laser output is coherent, and the coherence length, the distance light travels during the coherent time period. The coherence length, l_{coh} , is given by:

$$l_{coh} = \frac{\lambda^2}{\Delta\lambda} \quad 2.5$$

Where $\Delta\lambda$ is the linewidth (FWHM) of the laser output and λ is the mean wavelength. From this, the calculation of the coherence time, t_{coh} , is simply:

$$t_{coh} = \frac{l_{coh}}{c} \quad 2.6$$

Although these calculations may seem relatively trivial if the laser is to be used as a raw beam when interacting with a material, if techniques such as interferometry are to be used, increased coherence length gives more leeway when arranging apparatus.

As well as producing a coherent beam, the stimulated emission phenomena can produce a highly polarised beam [37]. If a preference for one polarisation exists in the laser cavity then a polarised beam will result. The beam can be polarised in several different ways:

<i>Linear polarisation</i>	All of the electric vectors of the radiation are aligned perpendicular to the direction of propagation.
<i>Random polarisation</i>	A mixture of all polarised states.
<i>Circular polarisation</i>	A mixture of two waves of the same wavelength but travelling at right angles with each other. The waves are out of phase by $\frac{1}{4}$ of the common wavelength.

As well as the presence of longitudinal mode inside the laser cavity, Transverse Electromagnetic (TEM) modes are also present. In lasers where the symmetry is controlled by a polarising element, rectangular TEM patterns are formed [38]. These modes are designated TEM_{mn} with m and n being the horizontal and vertical orders of the pattern. The control of modes which are present in the optical output of a laser can have a great influence on the beam quality. The TEM_{00-33} modes can be seen in Figure 2.4.

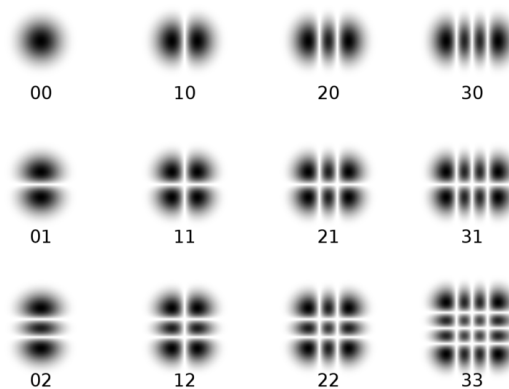


Figure 2.4. Transverse Electromagnetic (TEM) modes which can be present in a laser resonator [39].

The most notable of all the mode structures mentioned in Figure 2.4 is the TEM_{00} mode, which is more commonly known as a Gaussian beam profile [36]. Gaussian beams are

characterised by there irradiance profiles; these can be described mathematically by Equation 2.7 an example of this can be seen in Figure 2.5.

$$I(r) = I_0 \exp\left(\frac{-2r^2}{\omega^2}\right) = \frac{2P}{\pi\omega^2} \exp\left(\frac{-2r^2}{\omega^2}\right) \quad 2.7$$

Where I_0 is the peak intensity, r is the distance from the centre of the beam, ω is the beam half width and P is the power.

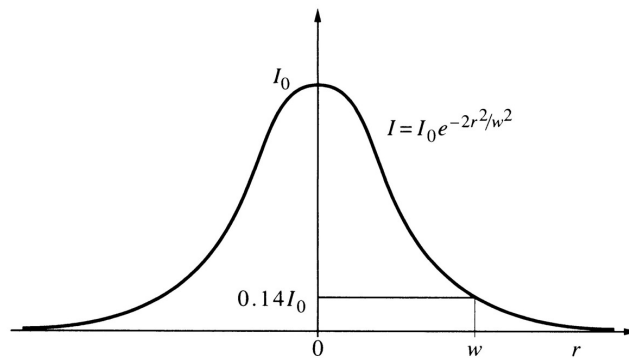


Figure 2.5. Graph to show the irradiance profile of a Gaussian beam (Adapted from [36]).

A large number of lasers have outputs which approximate the TEM₀₀ modes. Other classes of lasers such as excimer lasers have outputs which fit different spatial beam profiles. Most common is the top-hat shape, so called because intensity is uniform across the beam. The top-hat intensity profile occurs because there are a large number of TEM modes present in the beam.

2.3.1 Divergence

The divergence of a beam gives a measure of the amount the laser beam spreads out as it propagates in free space. This value is the half angle of the amount a beam spreads, or

diverges, as it propagates into the far field. Given that the laser wavelength and focal spot size, ω_0 are known, mathematically, the divergence, θ , of a Gaussian beam can be defined as [39, 40]:

$$\theta = M^2 \frac{\lambda}{\pi \omega_0} \quad 2.8$$

Where M^2 is a quality factor that will be discussed shortly and all other variables have their usual meaning. In the ideal case, the divergence of a laser beam would be zero, however, the world is not ideal and the divergence is usually expressed in milliradians (mrad). For Gaussian beams, divergence values of ~1mrad are common and multimode beams can have divergences as high as 20mrad [41].

2.3.2 M^2 and Beam Quality

One of the most commonly used measures of beam quality is the M^2 value [40, 42]. This parameter is dimensionless and can be used when quantifying the quality of approximately Gaussian beams and also multimode beams. For a diffraction limited beam, the M^2 value is 1. In reality, this is a physical impossibility.

The concept of a dimensionless beam propagation parameter arises from the fact that for all laser beams, the product of the beam waist radius and far field divergence are a constant. However, given that most laser beams are not truly Gaussian in shape, there will be differences in comparison to the theoretical Gaussian as the beam propagates

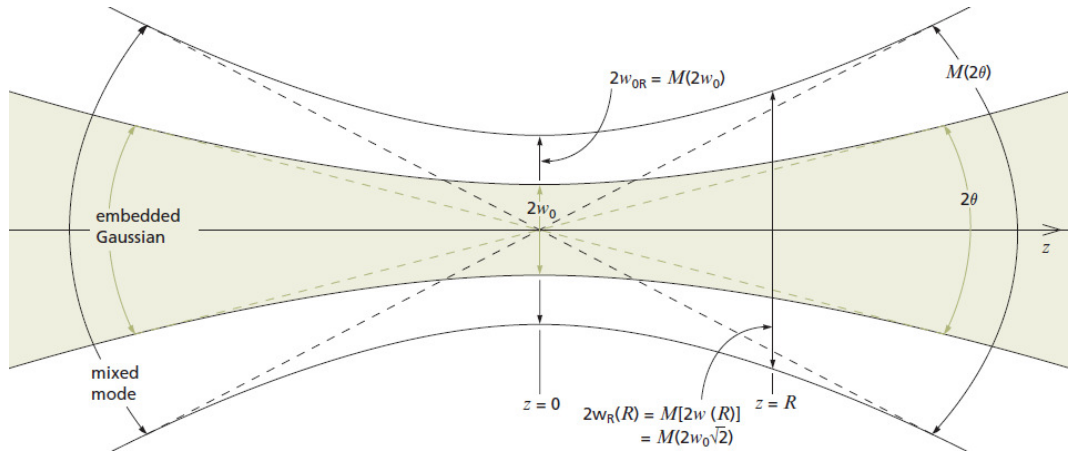


Figure 2.6. The measurement of an embedded (theoretical) Gaussian beam in comparison to a real beam.

through an optical system. These are summarised in Figure 2.6 and from these measurements, the value of M^2 for any laser beam can be calculated by:

$$M^2 = \frac{\omega_{0R} \theta_R}{\omega_0 \theta} \quad 2.9$$

Where ω_{0R} and θ_R are the beam waist and far field divergence of the real beam, respectively.

In addition to the quality of laser light produced, the way the light is delivered is also an issue. If a pulsed laser is used, there are several parameters, which are time dependant such as the pulse duration, average power, and peak power. These factors in turn yield other properties such as fluence, intensity and brightness.

2.3.3 Pulse Duration

The duration of an optical pulse can vary in a huge range. These time periods can range from the millisecond (10^{-3} s) regime to the extremely short attosecond (10^{-18} s). Pulses are not usually a square shape and for this reason the most frequently used definition for

a pulse duration is based on the full width at half-maximum (FWHM) of the optical power versus time.

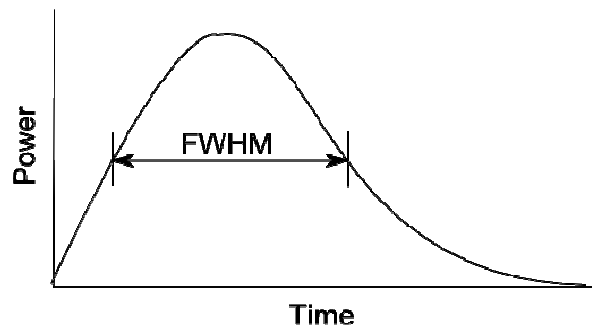


Figure 2.7. Usually, pulse durations are measured as the temporal pulse width at half of the peak value.

2.3.4 Energy and Power of Lasers

Considering a train of pulses with a repetition rate $\nu = 1/T$ as seen in Figure 2.8. Assuming the energy, E_p , contained within each pulse is constant then defining the energy change with time can give the power.

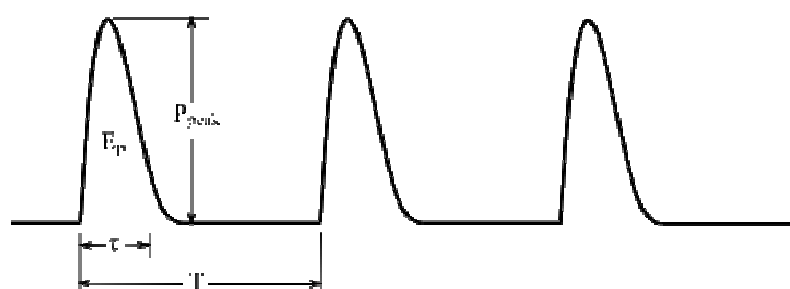


Figure 2.8. Common terms used to describe various features of laser pulses.

The peak power, P_{peak} , defines the energy flow within a single pulse and average power, P_{avg} , the energy flow over one period, T . These powers can be described mathematically as;

$$P_{peak} = \frac{E_p}{\Delta\tau} \quad 2.10$$

And

$$P_{avg} = \frac{E_p}{T} = E_p \nu \quad 2.11$$

In a laboratory it is more usual that the average power of a laser system is measured. This means that it is more useful to define the peak power in the form;

$$P_{peak} = \frac{P_{avg}}{\nu\Delta\tau} \quad 2.12$$

This also leads to the relationship;

$$E_p = P_{peak} \Delta\tau \quad 2.13$$

2.4 Gaussian Beam Optics

Although raw laser beams can be used to machine materials, it is often required that the light being emitted from the laser aperture is controlled in some way. This is where optics are needed. It is assumed that the reader of this document will have an understanding of the fundamental laws of optics, and for this reason these will not be commented on but further reading is available [40, 43, 44]. However, it would be advantageous to discuss Gaussian optics.

The theory of Gaussian beams is a common part of laser applications [45]. However, it is useful to recap some of the basic equations and relationships that result from the theory. When beams with a Gaussian profile are focussed using optics, because of their irradiance profiles, equations can be applied that describe certain properties and parameters of the beam such as beam waist, minimum focal spot size, Rayleigh range and depth of focus.

To achieve small spot sizes when focussing Gaussian beams, it is necessary to understand the relationship between input beam size, lens focal length and wavelength. The relationship between the minimum beam waist and the focal length is given by:

$$\omega_0 = \frac{f\lambda}{\pi\omega} \quad 2.14$$

Where f is the focal length of the lens [40]. The spot size of a laser beam at the focal point is given by $2\omega_0$. A trade off which occurs with the reduction of spot size is the reduction of the depth of focus. The depth of focus is calculated as twice the Rayleigh range, Z_R . The Rayleigh range is the region of the beam over which the radius of the beam increases by less than a factor of $\sqrt{2}$ [36]. This is also the point at which the area of the beam doubles. This region extends to each side of the focal plane, hence the concept of depth of field. The Rayleigh range, Z_R at the focal point of a lens can be calculated by:

$$Z_R = \frac{\pi\omega^2}{\lambda} \quad 2.15$$

The theoretical radius of a Gaussian beam can be calculated at any point along the optical axis using Equation 2.16 [39]. This can be done when the radius of the beam at the laser aperture, ω , is known. As well as the distance along the optical axis, Z , and the Rayleigh range, Z_R .

$$\omega(z) = \omega_0 \sqrt{1 + \left(\frac{Z}{Z_R}\right)^2} \quad 2.16$$

These equations can be used to describe how a laser beam will behave in various scenarios. These same equations are used when modelling many of the applications where Gaussian beams are present, inside or outside the laser cavity. In this case, they are used to model the way a beam will react when it is focused through a lens.

2.5 Laser Interaction with Materials

The primary focus of this project was to manipulate the surface topography of metals using lasers. This means that an understanding of how a laser interacts with matter is crucial. This section will discuss the interaction between light and matter, specifically those factors which affect laser material processing.

To understand the interaction of laser light with materials, it is first necessary to understand the basic principles of the way any light interacts with a material. As has been mentioned previously, light is delivered to a surface in discrete wave-like particles named photons. The reason for this wave-particle duality still occupies some of the greatest minds and could take up the entirety of this thesis. However, it is enough to say

that photons can act either as a wave or a particle. This means that in the case of stimulated emission, a packet of energy can be received completely by an electron in its excited state and stimulated emission can begin. Yet curiously, if the same photon were sent through a small gap, it would experience diffraction.

In the simplest terms, absorbed photons excite electrons, they give them energy. This energy is usually turned into heat. However the amount of absorption which occurs depends on the chemistry of the absorbing medium and, in this case, the wavelength of the particular laser system which is used.

All materials absorb and reflect light differently. This is what gives them colour. The frequencies of light which are absorbed and reflected can be mapped in an absorption spectrum. This gives a laser user wishing to modify a material a good idea of how effectively energy will be coupled from laser beam to material at any given wavelength. A typical reflectivity spectrum for a range of metals can be seen in Figure 2.9. Since $A=1-R$, this type of spectrum can be used practically as the inverse of an absorption spectrum.

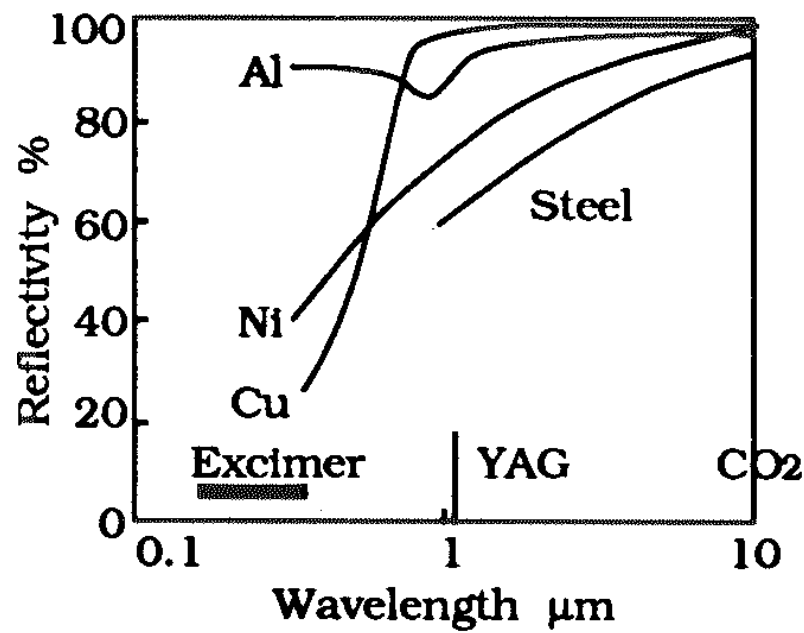


Figure 2.9 The reflectivity of Aluminium, Nickel, Copper and Steel over a range of laser wavelengths [11].

From Figure 2.9 it can be seen that there is a good reason for choosing the correct laser for a particular material. If a material is very reflective at the wavelength of the laser used to machine it then only a small amount of its energy will be coupled into the target. This can incur other problems also, such as damaging the laser itself as the reflected light returns along the same optical path as the incident beam.

As would be expected, when a laser beam interacts with a material, not all of the radiation is absorbed. Some of the radiation will be reflected and some may be transmitted. The Beer-Lambert law (2.21) describes the attenuation of a laser beam of intensity, I_0 , in terms of the transmitted intensity, I , at a depth in the material, z in relation to the absorption coefficient, α which will be discussed later and is dependant on the material, wavelength and beam intensity [46, 47].

$$I = I_0 \exp(-\alpha z) \quad 2.17$$

When measuring the absorptance (A), the ratio of absorbed radiation to the incident radiation, of a material it is normal to measure the reflectance (R) that is the ratio of reflected radiation to incident radiation. From this it can be deduced that;

$$A = 1 - R \quad 2.18$$

If we concentrate on metals, it is known that a laser beam primarily interacts with the ‘cloud’ of free electrons that are not associated with the majority of atoms forming the metal. When the laser interacts with these electrons, they oscillate and then re-radiate their excess energy. This is what gives metals their high values of reflectivity.

Laser heating primarily happens in a thin layer at the surface of the target material [48].

This optical penetration depth is related to the absorption coefficient in the form:

$$\delta = \frac{1}{\alpha} \quad 2.19$$

a heat affected zone (HAZ), which is very large in comparison to the optical penetration depth, can be formed if the radiation from the laser is better transmitted through the lattice. This occurs more often in materials when the heating, which occurs due to the laser-material interaction, is caused by diffusion of energy through the material.

The thermal diffusivity, D of a material is a way of predicting how a material will behave when it interacts with a heat source such as a laser beam. It is described mathematically by [11, 47, 48]:

$$D = \frac{k}{\rho c} \quad 2.20$$

Where k is the Thermal Conductivity, c is the heat capacity and ρ is the density of the material. Although this equation can be applied to any material, the way a material will react to the heating varies. It can be seen from Figure 2.13 that there are two distinct regions, which are affected by the incident laser radiation. These two regions are those which are heated due to optical absorption and heat flow/diffusion. Depending on the material, the heat affected zone (HAZ) during ablation can be dictated by the optical absorption length or the heat flow.

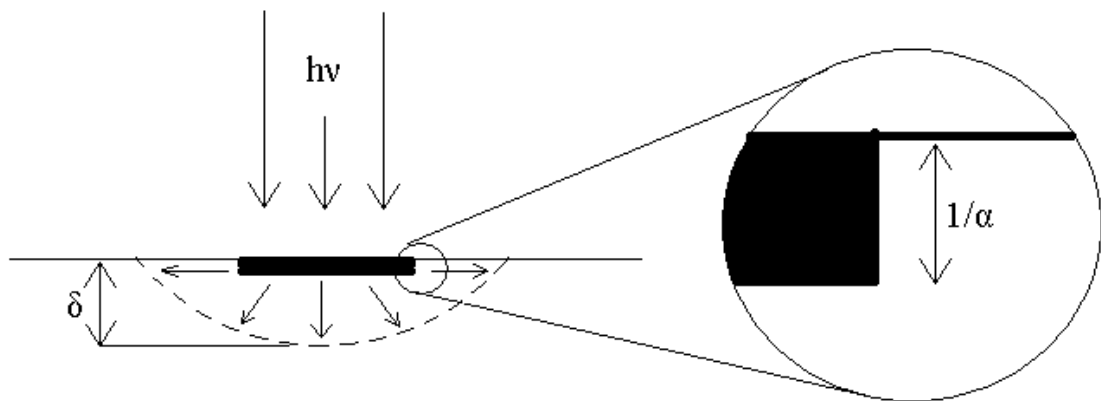


Figure 2.10 Schematic of depths below a target surface where optical absorption and heat diffusion processes are present.

In fig.5.1 the laser heated volume of the material is defined by the heat flow rather than the optical absorption of the material. The depth of the heat flow, δ is given by $\delta = 2\sqrt{Dt}$, where D is the thermal diffusivity and t is the duration of the pulse.

2.5.1 The Effects of laser Heating

The emission for a laser is simply coherent electromagnetic (EM) radiation. Due to its properties, this light can be focused into very small areas where its intensity can be raised into the GWm^{-2} regime, if only for a short period of time. The effect this EM radiation has on a material can range from simple heating of a few degrees to explosive vaporization called ablation. The way in which the laser light interacts with a material depends on various factors. These include the laser wavelength, the laser interaction time with the material, the reflectivity of the material and also the type of bonds which are present within the material. This PhD is primarily interested in metals, so it is this type of material which we will concentrate on.

The topic of laser interaction with materials is extensive. This is because not only are there a large number of materials, there are also a large number of laser parameters that can be varied. Fortunately, there are several principles, which apply to all forms of laser interactions. The first of these that should be mentioned is laser heating.

2.5.2 Laser Heating

Although heating can occur when the light of a desk lamp is applied to a material, the heating that would occur if a laser of the same power was applied would, more than likely, be greater. This is because laser light is coherent and of a single or small spread of wavelengths. In this case, because of the coherence, the laser radiation is introduced to the surface of a material in waves rather than a randomly distributed spread. In addition to this, laser beams can be focused to very small focal spots which have very

high powers and intensities. A metallic material under the influence of laser heating experiences a temperature rise because the energy delivered by photons is transferred to electrons in the metal structure. As the energy of these electrons increases they begin to collide with others, transferring their energy. In this way, the heat affected zone described earlier can be formed. When the power is increased so that the material is close to its melting point we move into the next regime.

2.5.3 Laser Melting

Due to the nature of laser radiation, especially when it is delivered in a very short pulse, heating is usually achieved very quickly and the material changes phase. At a temperature which varies from one material to another, the atoms in a crystalline structure stop vibrating in the solid state and enter a state of free rotation. This is the point at which a material enters a molten, or liquid, phase. Generally, materials with high bond strength have higher melting temperatures.

2.5.4 Laser Vaporization (Ablation)

If a material is heated with a laser past the point of melting and towards the heat of vaporization slowly, the same type of transition which occurred at the boundary between solid and liquid will occur between liquid and gas phases. However, again because of the high power densities which are present during laser processing, it is possible to increase the temperature of a target material so rapidly that explosive vaporization, or ablation, occurs. Ablation is usually referred to as the volumetric

removal of material. The power density at which there is a change directly from a solid material to vapor is a threshold value for each material.

2.5.5 Ablation Threshold

One of the early discoveries while investigating laser materials processing was that there is a linear correlation between the amount of material removed during laser ablation and the energy density on the target surface [46, 49]. The fluence of a laser beam is a measure of this energy density and usually has the units Jcm^{-2} . As a derivation of the Beer-Lambert law (2.17), it was found that plotting the depth of material removed for a set number of laser pulses against the natural logarithm of the laser fluence, both the effective absorption coefficient and the threshold fluence for the material at that wavelength could be determined [14, 46, 50]. The derivation is:

$$d = \frac{1}{\alpha_{\text{eff}}} \ln \frac{F}{F_T} \quad 2.21$$

where d is the depth of material removed per pulse, α_{eff} is the effective absorption coefficient, F is the laser fluence and F_T is the threshold fluence for laser ablation [46, 50, 51] which is additionally given by $F_T = \rho c((T_D - T_R)/\alpha(1 - R))$, R is the reflectivity, ρ is the density of the material, c is the specific heat capacity, T_R the initial temperature and T_D is some critical temperature at which rapid thermal degradation occurs. Since a large effective absorption coefficient implies efficient coupling of light energy into a material this means the energy is absorbed into a small volume so the temperature increase is significant. For a small absorption coefficient the light is

absorbed into a greater volume therefore the energy loading is small and the resulting temperature rise is modest (at least in the absence of multiphoton processes). Figure (a) shows a large efficient absorption coefficient and (b) shows a small effective absorption coefficient.

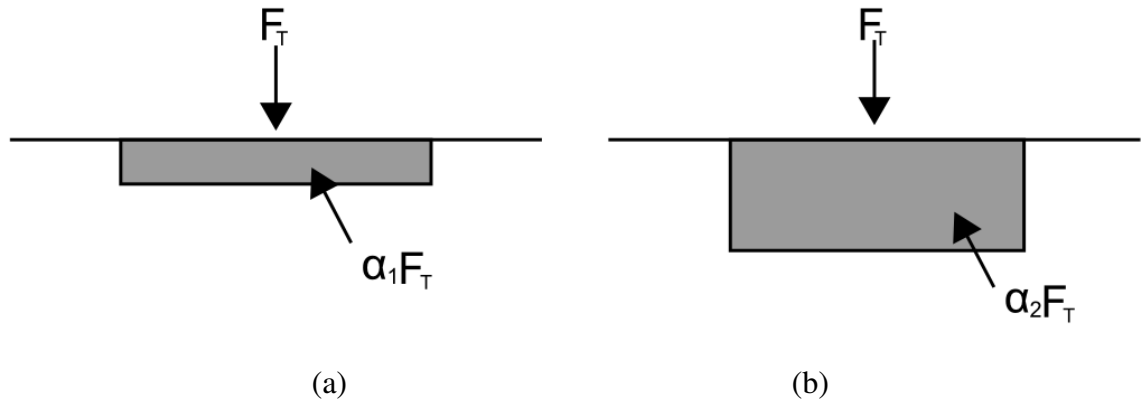


Figure 2.11 a) large absorption coefficient, α_1 , with high volumetric energy loading, (b) small absorption coefficient, α_2 , with small volumetric energy loading. This assumes the same input fluence.

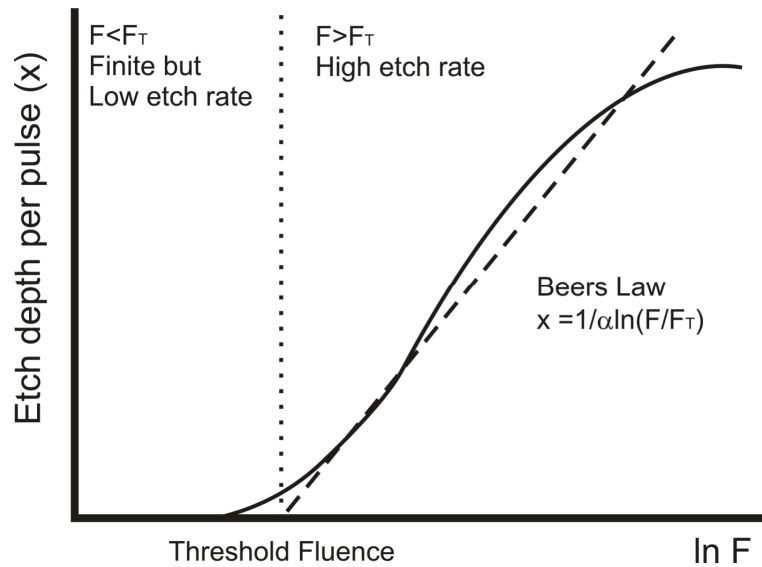


Figure 2.12. Example of the etch rate of a polymeric material [52]. The solid curve is a representation of experimental data, while the dashed line represents the ideal case, which fits the form of Beer's law given in equation 2.21.

Despite the insight obtained from Equation 2.21, the experimental etch depth as a function of the logarithmic fluence often deviates from the ideal case as illustrated in Figure 2.12. The solid line shows the experimental data, and eqn. 2.21 is represented by

the dotted line. At higher fluence it has been found [53] that the etch rate becomes curved with respect to an increase in fluence. The saturation of the etch rate at high fluence has been attributed to absorption or scattering in the plume thus attenuating part of the incident pulse before it reaches the sample surface [54].

2.6 Review of Laser Surface Topography Modification

Lasers are widely used as tools for manufacturing, there are a large number of techniques, which can be used to create micron scale topographical structures. Many of these have been highly developed and are now used in industrial processes. The creation of microstructures is usually dependant on optical arrangements and there are two basic methods. The first of these is direct writing. This method is the simplest to comprehend because it can be used in much the same way as a pen is used on paper. The difference is that rather than depositing material onto the surface, the target material is removed by ablation. There are many techniques which can be used to enhance the effectiveness of direct writing. Obviously, the first of these is the method of translation used to address different points on the target surface. The two main methods are target translation, using a mechanical stage, and beam translation, using a scanning system using prisms or mirrors. In this case, two mirrors which are controlled by software on a control computer are rotated in either the X or Y plane and focused using a flat field lens. Some examples of microstructures produced using direct writing can be seen in Figure 2.13 below [13].

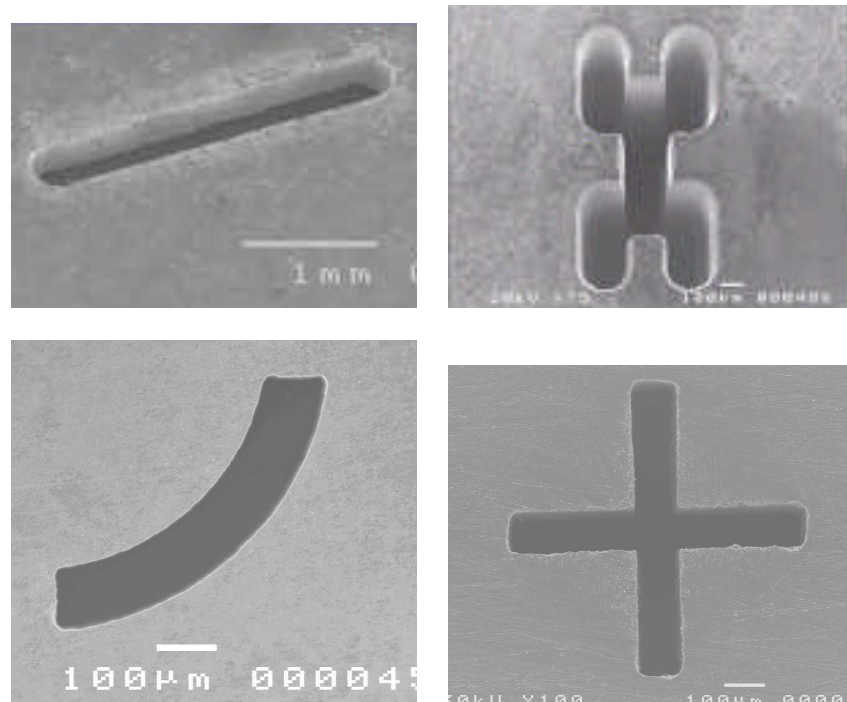


Figure 2.13. Examples of direct writing of micro-features on metals using Gaussian beams [13].

The resolution of features produced using direct writing is limited by the accuracy of the beam delivery system and the quality of the optical arrangement which is used. For this reason, one of the necessities for direct writing of microstructures is a good beam quality, usually a Gaussian beam. If this is not so, then uniform machining will not occur and the resultant structures may be distorted. To make use of low quality laser beams, another method of micromachining must be used. Direct writing is probably the most used form of laser processing. Depending on the power used, the direct writing technique can be used to ablate the surface to create microstructure or, at higher powers, for the drilling and cutting of materials with a high degree of accuracy.

Mask imaging can be a very useful technique when dealing with multimode beams or those with a low beam quality. Another advantage of using mask imaging is that large areas can be processed in a relatively short time if the technique is used in conjunction with system to address different points on the target, such as a translation stage. Some

examples of the types of features that can be produced using excimer beams to create microstructures can be seen in Figure 2.14 and Figure 2.15.

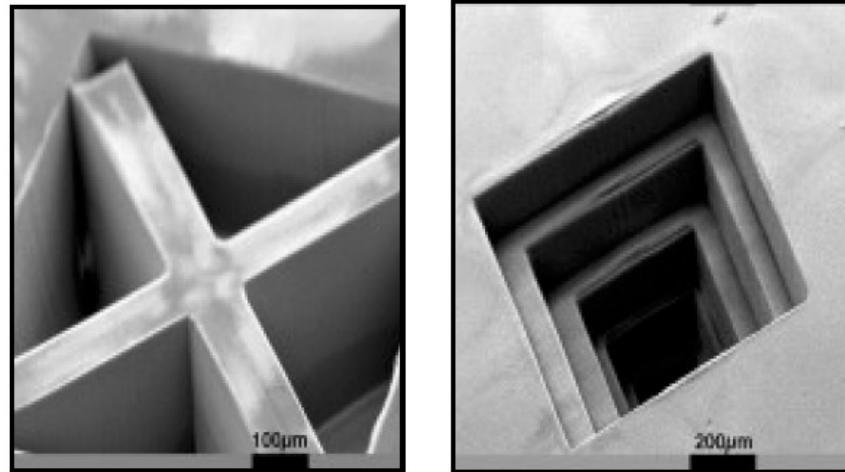


Figure 2.14 Microstructures ablated in polymers by static mask projection

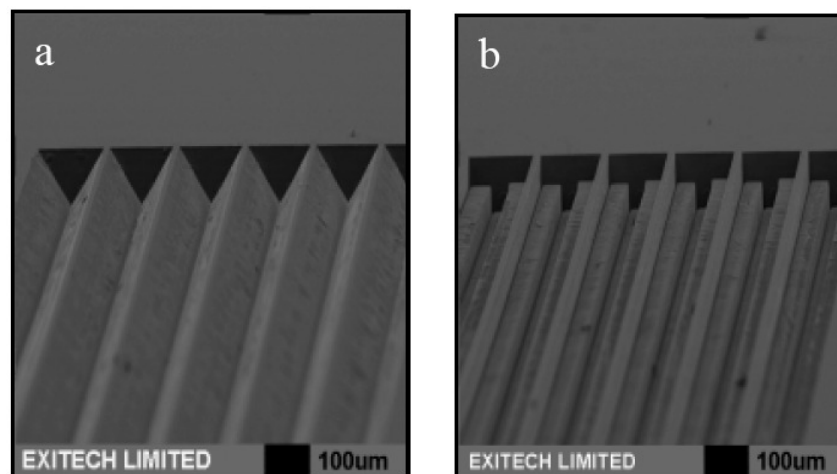


Figure 2.15. Microchannels produced with (a) a triangle mask, (b) a 'T'-shaped mask

The resolution of the features which can be produced using mask imaging are dependant on the wavelength of the laser being used, the quality of the optics and the size of the mask. It is particularly important the no diffraction occurs due to the apertures present in the mask.

These techniques have been discussed briefly so that the reader has an insight into the kind of practices which take place regularly. In this project the method used for surface topography modification is most akin to direct writing however a slightly different approach to surface topography modification using lasers is taken. Rather than removing material to directly form surface topography at specific points, this project produces topographical changes over desired areas.

2.6.1 Self Assembly Methods of Laser Surface Topography Modification

The use of lasers for the direct writing of micron scale topographical features is common practice in the field of materials processing. However, the use of lasers to produce self-assembled structures is a less exploited area. Over the past several years, there have been several reports of laser generated self-assembled microstructures on metals [12, 16, 55-59], semiconductors [16, 17, 56], and polymers [14, 50, 60-64]. These structures are designated as self-assembled because although the area in which features are desired is designated, the exact distribution is not. Initial work on this subject concentrated on polymers. It was found that the slope angle of microcones is related to the ablation threshold for individual materials [14]. Suggestions as to how these structures develop on polymers have also been given [14, 65] and are the result of small

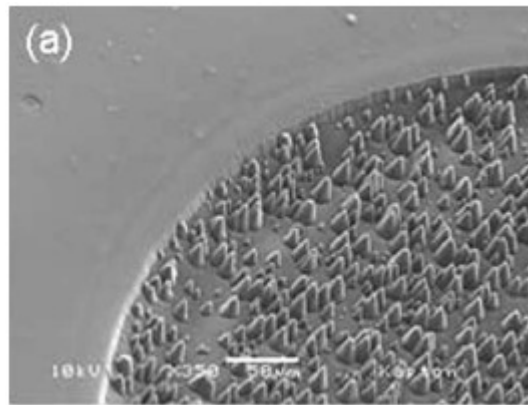


Figure 2.16. Polyimide after machining with a KrF (248nm) laser [65]

particles that are deposited on the surface either from the ablation process or the environment. An example of the types of topographic structures that are seen on polymers can be seen in Figure 2.16. Unlike conical structures that have been reported on laser machined polymer surfaces, the process by which microcones and alike are produced on a metallic and semiconductor substrates is thought to be a melt flow dominated process rather than an ablation process. Previous results have shown that when a large number of laser pulses are delivered to various metal targets, self-assembled arrays of microstructures, with a period of 30-50 μm , can be formed [17, 57]. It has also been shown in similar studies that structure formation can occur in liquid environments [58]. It is also hoped that this project will address reports that the self-assembled structures which are under discussion align themselves with the incoming laser beam. This has been shown to some degree by Dolgaev *et al* [17]. However, it is not clear if a systematic study of this effect has taken place. This group has also shown that silicon microcones can be produced by laser machining in an SF_6 environment. As self-assembled microstructures are not exclusively produced in exotic gas environments, it would seem reasonable that such surfaces can be produced in a gaseous

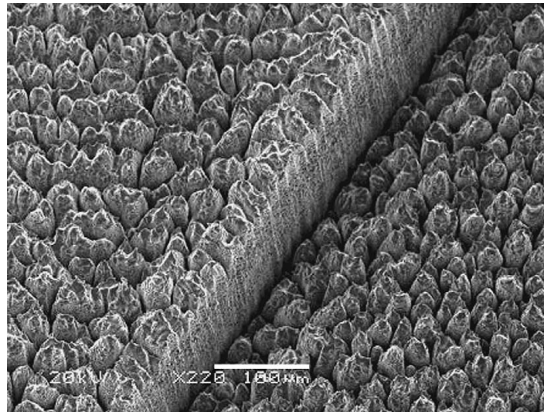


Figure 2.17. Brass in Ethanol And Water. Nd:YAG (1064nm), ~16 J/cm², >10⁴ Pulses, Spot Size ~40μm. Scale bar 100μm [58].

environment such as air. The production of such features has been shown to have applications in the fields of surface reflectivity[66], wettability, microbiology and biomedicine. Some examples of self assembled structures produced in various environments can be seen in Figure 2.17 and Figure 2.18.

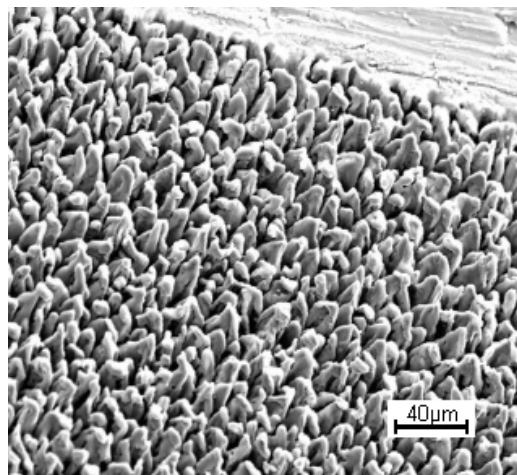


Figure 2.18. Single Crystal Ge in Vacuum, Cu Vapour (510.6nm), $\tau = 20$ ns, ~1J/cm², 10⁴ Pulses. Spot Size ~ 40μm [58]

There have also been relatively recent developments in the modification of surface topography at larger scales. Continuing work done using electron beams [67], The Welding Institute (TWI) has developed a process named Surfi-Sculpt[®]. An example of

the type of surface features that can be made using this technique can be seen in Figure 2.19.

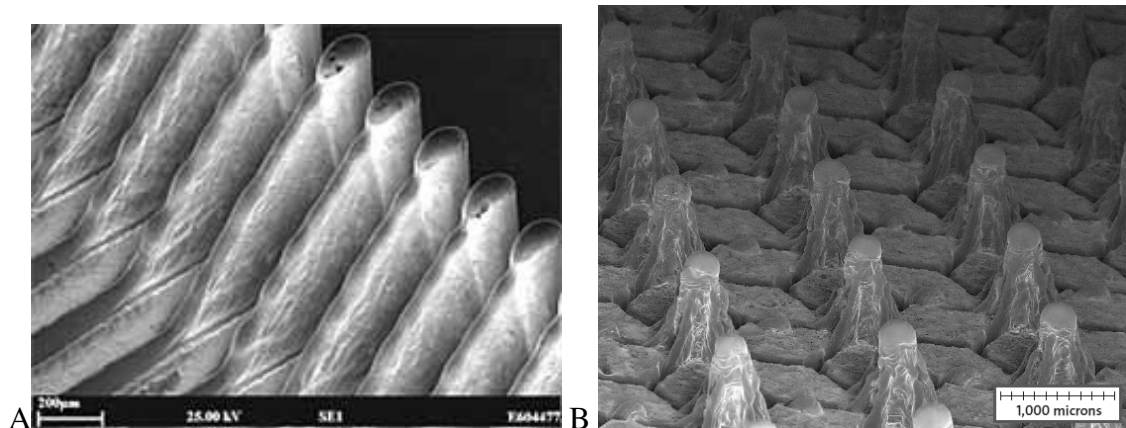


Figure 2.19. An example of the types of surface topography that can be created using Surfi-Sculpt®. Scale bars 200µm (A) and 1mm (B)

These structures are grown by the careful control of the surface temperature as an electron beam or CW laser beam is scanned rapidly over the surface. At the heart of this process is the interplay between surface tension as the laser scan path is cooled and the pressure from the vapourised material from the scan path. This has the effect of displacing material in a direction opposite to the beam's direction of travel. Larger features are created by repeatedly scanning over the same area, making the feature grow a little with each pass. Unfortunately, there is very little literature relating the Surfi-Sculpt® directly as it is the intellectual property of TWI.

Another method of changing the topography of a material is the use of interferometry. By interfering one or more beams, the constructive and destructive interference that occurs at their intersection allows a large number of different ablation patterns to be produced. Figure 2.20 shows examples of surfaces formed using various geometries of two and three beam interference. This type of surface topography modification is more

suited to the formation of submicron features, this is because the period of feature formation relies heavily on the wavelength of the laser light used.

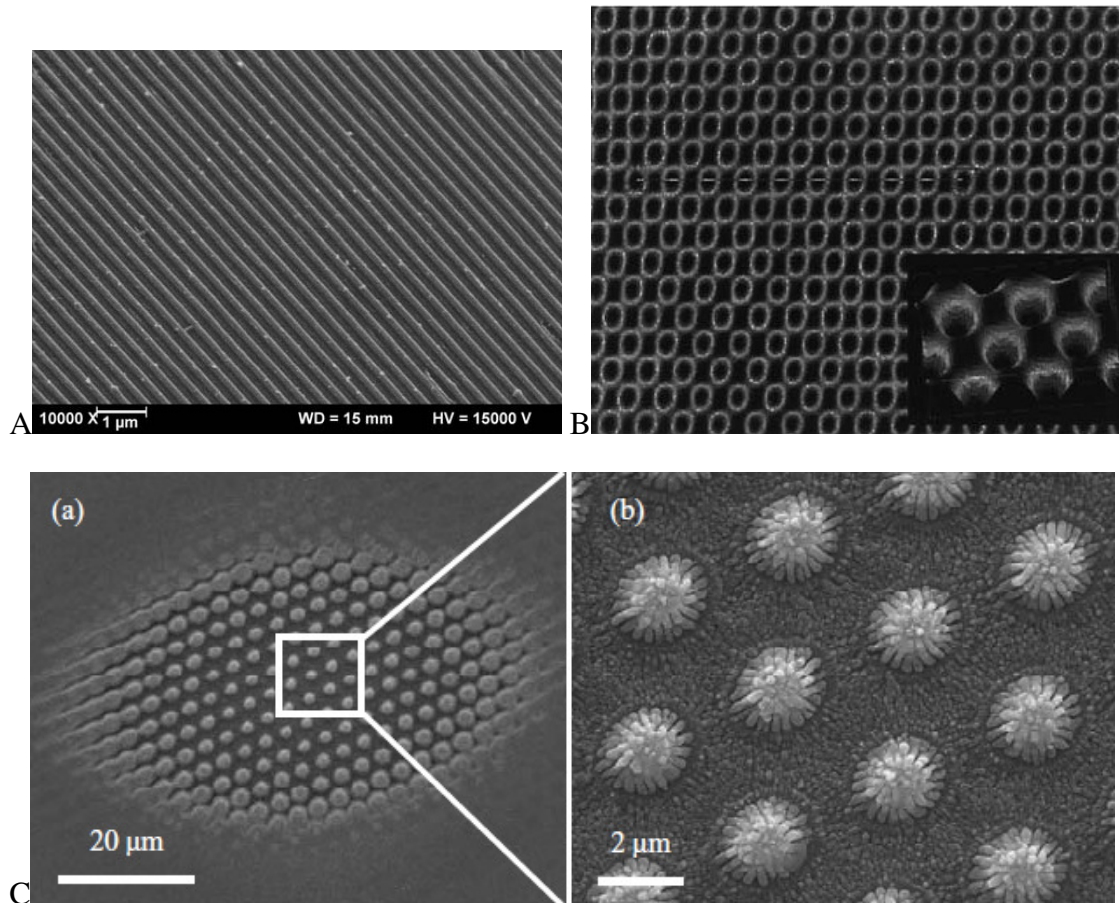


Figure 2.20. Examples of surfaces produced using interferometry. The three figures show structures formed using two beam interferometry (A) [68] and three beam interferometry (B and C). The difference between structures seen in B and C [12] [69] are due to differing interference geometries.

2.6.2 Producing sub-micron features using interference

Due to the resolution limit of conventional optics, fabrication of structures which are in the sub-micron and nano scales must be created by manipulating the intensity of light. There are several successful techniques which utilise interference to control the intensity distribution of laser light used to produce sub micron structures. Commonly these techniques use variations in optical intensity produced by interference to

selectively ablate surfaces. Figure 2.21 shows the microstructures which can be produced by taking advantage of the way a multimode excimer beam diffracts through an amplitude mask consisting of an array square apertures with a spacing of approximately 20 μm . The intricate intensity distribution is the result of near field diffraction [70].

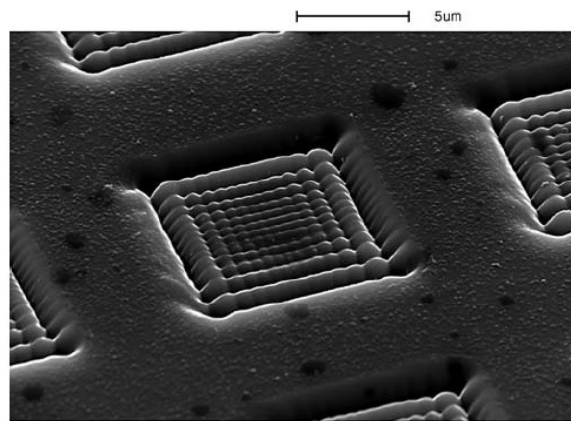


Figure 2.21. Scanning electron micrograph of an array of microfeatures etched in N-BK7 glass using an F_2 laser beam after propagation through a transmission mask [71]

Other techniques to produce sub-micron structures can involve the interference of two or more [69, 72, 73] coherent beams allow the production of lines with a very small spacing which is below the wavelength of the laser used to machine them [74] and the use of three beams can facilitate the production of three dimensional structures [12, 73]. Unfortunately this technique requires a complicated experimental apparatus.

Another type of topographical feature which is a known side effect of laser processing with pulsed lasers at low powers are laser induced periodic surface structures (LIPSS) [15, 18, 62, 75-83]. Again these structures were noted on polymers before metals but in both cases it is found that they are formed by interference between the incident laser beam and light scattered from the surface after reflection. It is simpler to produce these structures on surfaces and they can be confined to the area affected by laser pulses. An

example of this type of structure can be seen in Figure 2.22. Additionally, it is known that LIPSS form in a direction perpendicular to the direction of polarization of the laser beam unless it is circularly polarised [84].

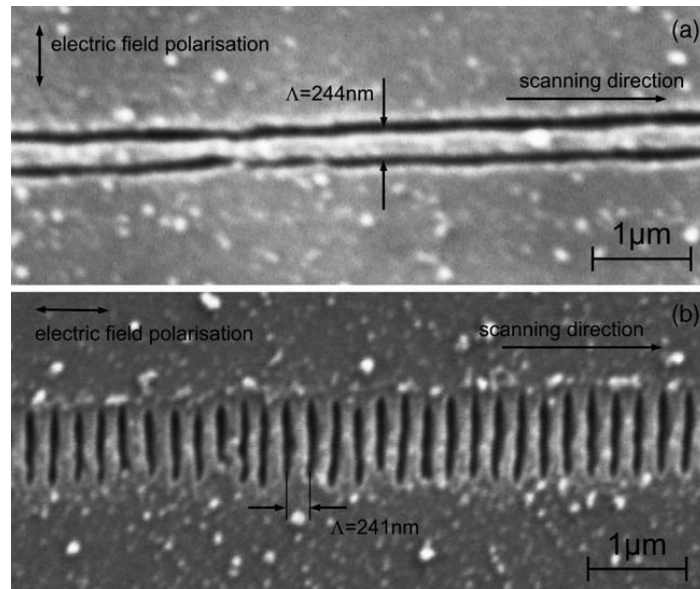


Figure 2.22. Demonstrations of LIPSS formed within the confined of a laser spot. It can be seen from both figure a and b that structures form perpendicular to beam polarization (indicated) and have almost the same period. [84].

3 GENERAL METHODS

As important as understanding the theoretical background of a subject is, the production, measurement and analysis of parameters and results is crucial. Although the physical principles which have already been discussed are explored in this PhD, the tools with which this is done are worth discussing in their own right. This chapter will briefly discuss many of the main technologies and analytical tools which are used in this project. Methods of delivering a laser beam to a target surface are discussed but the main focus here is on the analysis tools, which are used.

3.1 Laser Control and Processing

Very few of the laser processes carried out in this project can be controlled manually. The accuracy needed to control the synchronization of laser output and beam/target position is simply too high to be completed without the aid of control software. Some lasers have their own software to control various parameters of the laser output. These are generally custom made by the system manufacturer. Fortunately, this software can usually be overlooked as once they are set, changes do not often take place during a process. Indeed, the laser systems in this project require an external trigger to fire the laser. In laser materials processing, this external trigger is given by the control system which accurately synchronises the laser pulses and delivers the output beam to the correct position on a target.

During this project, two beam delivery systems were used. The first of these is a galvo scanning head. These devices operate by steering an incoming beam using mirrors to

manipulate the laser beam in the x and y planes of the target surface. The beam is then focused by a flat field lens. This type of lens focuses incoming light to a plane rather than a single focal point. An illustration of the scanning head used in this project can be seen in Figure 3.1.

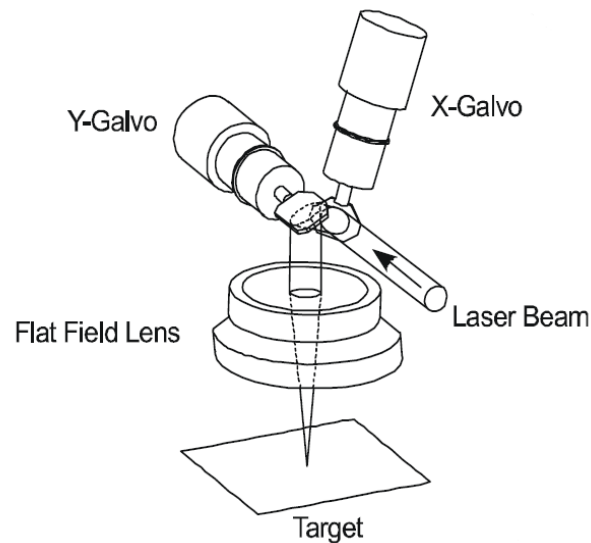


Figure 3.1 Schematic of a scanning head

The Waverunner software used in this project to control the scanning head follows paths which are input as vector drawings. These are then translated into scanning patterns. This type of beam delivery system is very good for the processing of large areas at high speed. However a trade-off is made. As the beam is directed towards the edge of the processing area its angle of incidence decreases which can sometimes have adverse effects.

The second system used to control beam delivery was a three-axis translation stage, manufactured by Aerotech and controlled using NView software.



Figure 3.2 Three Axis Aerotech stage with focusing optics and target holder

In contrast to the system equipped with a scanning head, a translational stage relies on target manipulation rather than beam manipulation. This gives more accurate control of the sample position. Unfortunately the processing speeds and target size are limited by the constraints of moving the stage and target. An Aerotech stage is controlled using the programming language GCODE. This is a language more commonly associated with CNC (Computerised Numerical Control) machines such as lathes or milling machines but the language has been adapted for use with laser systems. This simple language allows procedural control of a laser system, controlling the movements, including feedrate and position of each axis individually.

3.2 Analysis Tools

One of the unfortunate limitations of the human senses is that we have evolved to be just good enough at a lot of tasks. Fortunately the species has also been imbued with a talent for adaptation and gifted individuals to develop tools and devices to extend our senses. These technologies allow us to understand the chemical and physical properties of materials.

3.2.1 *Microscopy*

Microscopy is one of the most widely used analytical techniques used in this project. However the methods of microscopy do vary. Two types of microscopy were used in this project, optical and scanning electron. Some specialised techniques related to these technologies are also discussed separately.

If we begin with the most widely known method, we must begin with optical microscopy. Optical microscopy revolutionised the way we see the very small. It allowed features which are barely visible to the naked eye to be resolved with clarity. Early microscopes consisted of little more than a small glass bead which acted as lenses with high magnification due to their small radius of curvature. Soon however, more elaborate optical arrangements were developed until compound microscopes resembling those which we know today were built.

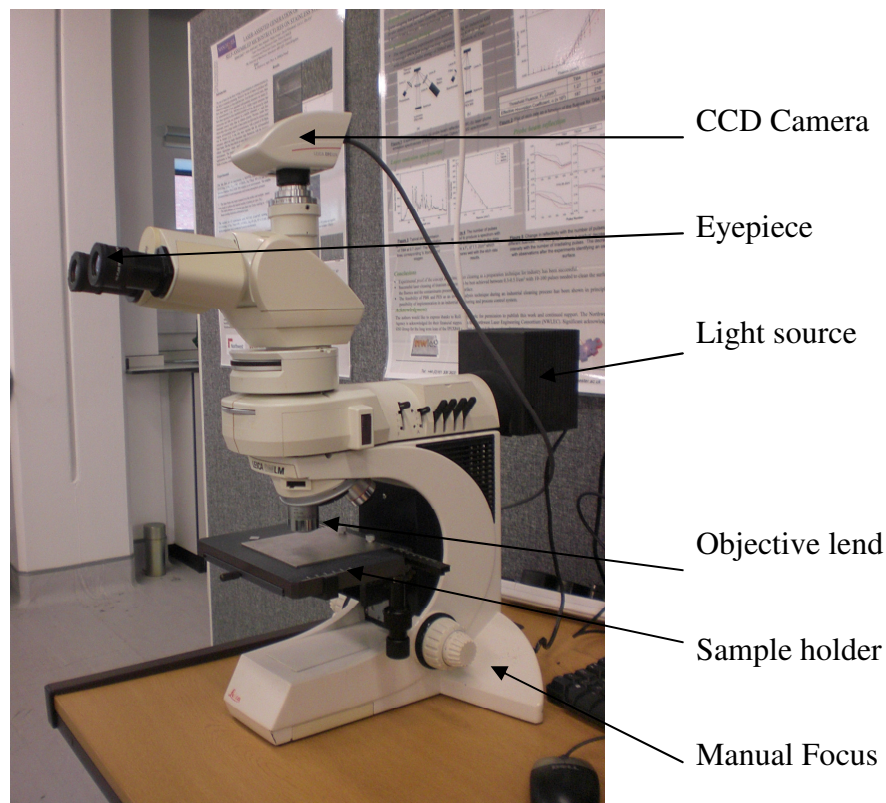


Figure 3.3 Arrangement of an optical microscope

Modern optical microscopes, such as those seen in Figure 3.3 are modernised versions of those early designs. Where early microscopes had a fixed magnification, it is now common for an optical microscope to have multiple objective lenses ranging in magnification from $\times 2$ to $\times 150$. Obviously, this means that the resolving power of modern microscopes is greatly improved and so is the way these optical images are recorded. Although there are still eyepieces for the use of the operator, many optical microscopes now employ a charged coupled device (CCD) cameras to record the images that are seen. With the aid of digital processing software, it is also possible to perform measurements on these images, recording distances and feature height with micron accuracy.

Unfortunately, the same physical restrictions which apply to laser processing mentioned in chapter two also apply to optical microscopy. This is because the same optical laws are used. One of the main problems is resolution, this is in both height and spatial parameters. Spatial resolution has a theoretical limit of 200nm. The problem of resolution in terms of height is due to the trade-off which is made as the magnification of a lens increases. As with the principles employed in Gaussian optics, to produce a smaller spot, and hence increase the resolving power of a lens, then the numerical aperture of a lens must be increased and the depth of field sacrificed. As magnification increases this means that rough surfaces, such as those produced in this project are difficult to inspect with any clarity. Fortunately, higher resolutions can be achieved using scanning electron microscopy.

3.2.2 Scanning Electron Microscopy

Scanning Electron Microscopy (SEM) is one of the most common solutions to viewing surfaces at high magnification with more clarity. The operating principles of an SEM are very similar to those of an optical microscope. The difference being that rather than manipulating the path of photons as they interact with a sample, a SEM manipulates electrons.

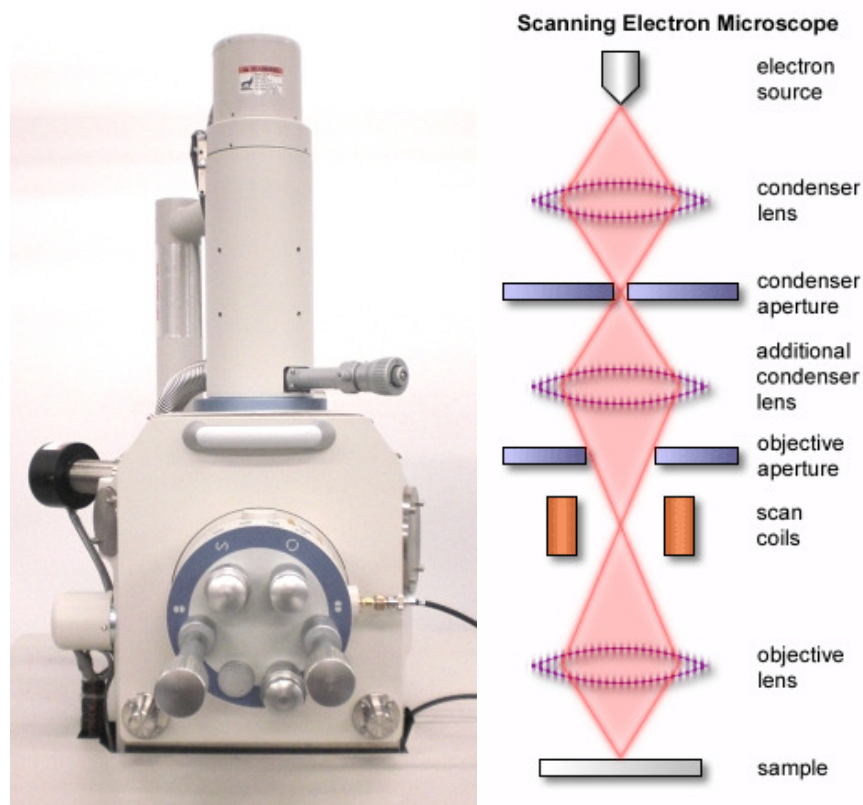


Figure 3.4 Arrangement of a Scanning Electron Microscope (SEM)

The arrangement of a SEM can be seen in Figure 3.4. If we carry on with the analogy of an optical microscope, we now come to the interaction of electrons with the sample to be inspected. In an optical microscope, photons are reflected back from a surface and returned to the eyepiece. Electron microscopy operates on a different principle. Firstly, rather than the sample being passive, in electron microscopy it must be electrically conductive and positively charged so that it attracts the negatively charged electrons. Secondly, as electrons are directed towards the target, they are so small that they will actually penetrate into the surface of the target. Once they interact with atoms directly, one of two events can happen. The electron can be absorbed into an atom and a short time later a secondary electron will be emitted, or the electron will interact with the nucleus of the atom directly and return to the collection device as a backscattered

electron. SEM devices are not exempt from limitations such as depth of focus or resolution; however, their resolving power is easily an order of magnitude better than their optical counterparts. The improved depth of field also means that the samples can be viewed from various positions. This in combination with the ability to measure distances on images formed by the image capture systems in SEMs makes them a very useful tool for measuring rough surfaces very accurately.

3.2.3 MEX

Indeed, the problem of measuring rough surfaces is one which needed to be addressed in this project. The usual way to measure the roughness of a surface is to use either an optical or mechanical method. Optical methods usually involve measuring the distance to the surface from a fixed point using a laser and building a map of the surface or the use of white light interferometry. Mechanical methods use a stylus to track and record the surface. Unfortunately, many of the surfaces produced in this project are too small for these methods but too large for atomic force microscopy (AFM) which has an upper limit, in terms of height, of 10 – 20µm. The solution to this is the use of SEM along with digital electronic models (DEM) produced using a software package called MEX[®] produced by Alicona[®]. This software builds a DEM of a surface using SEM images of a surface which are made at three slightly different viewing angles. This arrangement can be seen in Figure 3.5.

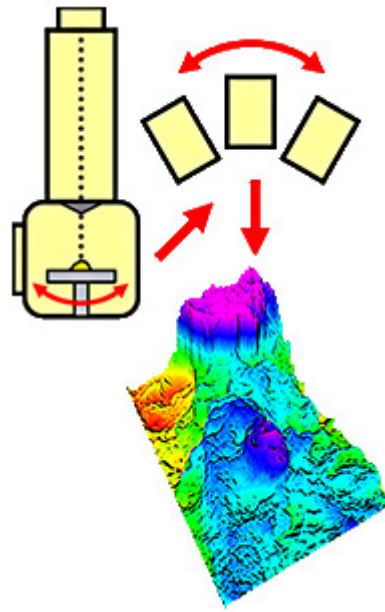


Figure 3.5 Orientation of samples needed for the production of MEX digital electronic models.

These images are then analysed to measure the change in position of surface features and, knowing the difference in viewing angle, the height of the surface at any particular point can be calculated by trigonometry. This allows the production of images such as Figure 3.6. From these datasets a number of surface measurements can be taken. These include statistical measurements, such as roughness values and direct measurements, including surface profiles and other direct measurements. The nature of a digital model means that software can analyse the topography of DEM surfaces and extract data such as surface roughness and arbitrary surface profiles easily. Particularly, this project uses this software for the analysis of surface roughness. This method is used rather than more traditional roughness measurement methods because of the scale of features produced.

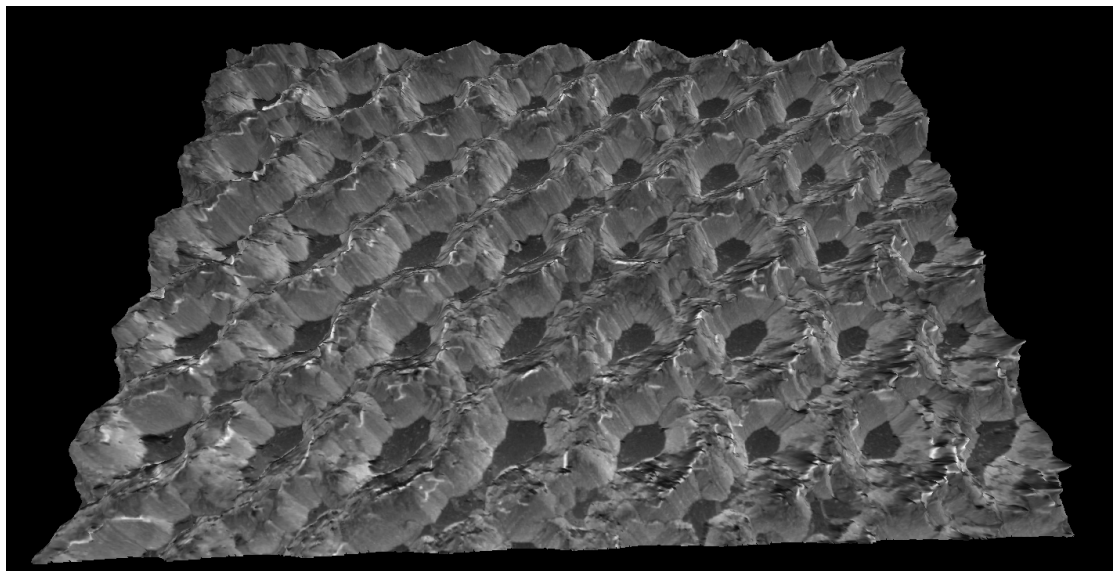
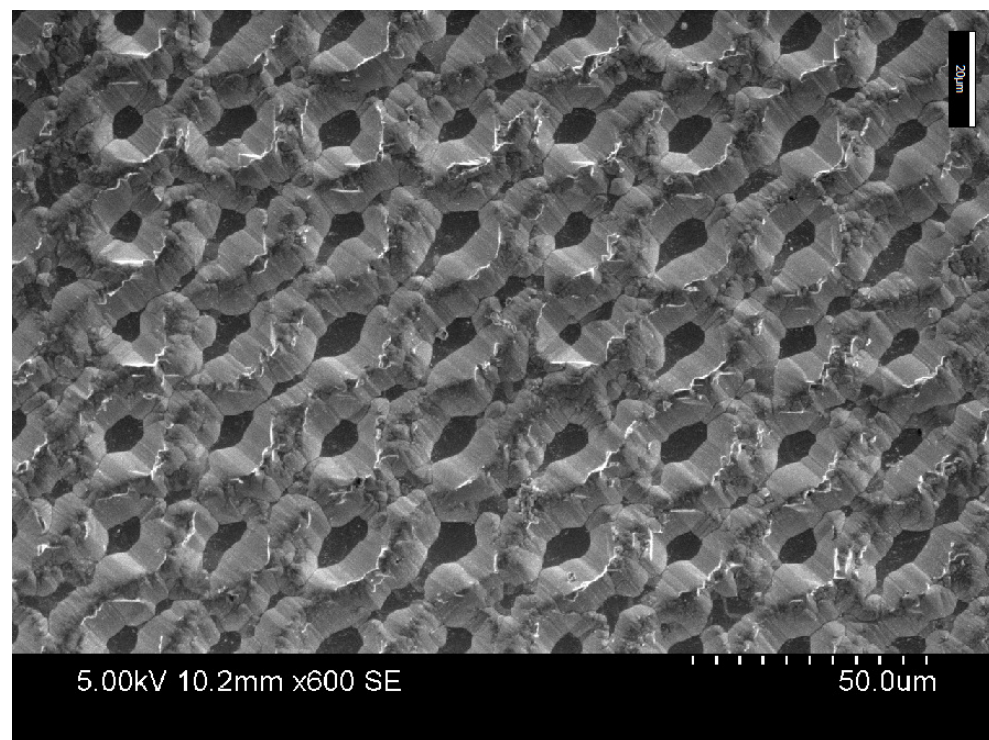


Figure 3.6 An example of a digital electronic model (DEM) created in MEX[®] (bottom) using three source images similar to the SEM image shown (top) .

3.2.4 White Light Interferometry

Another method of measuring roughness and depth on reflective surfaces is that of white light interferometry. Figure 3.7(a) shows the Wyko NT1100 surface profiler that is a non contact tool that can measure a wide variety of surfaces and samples.

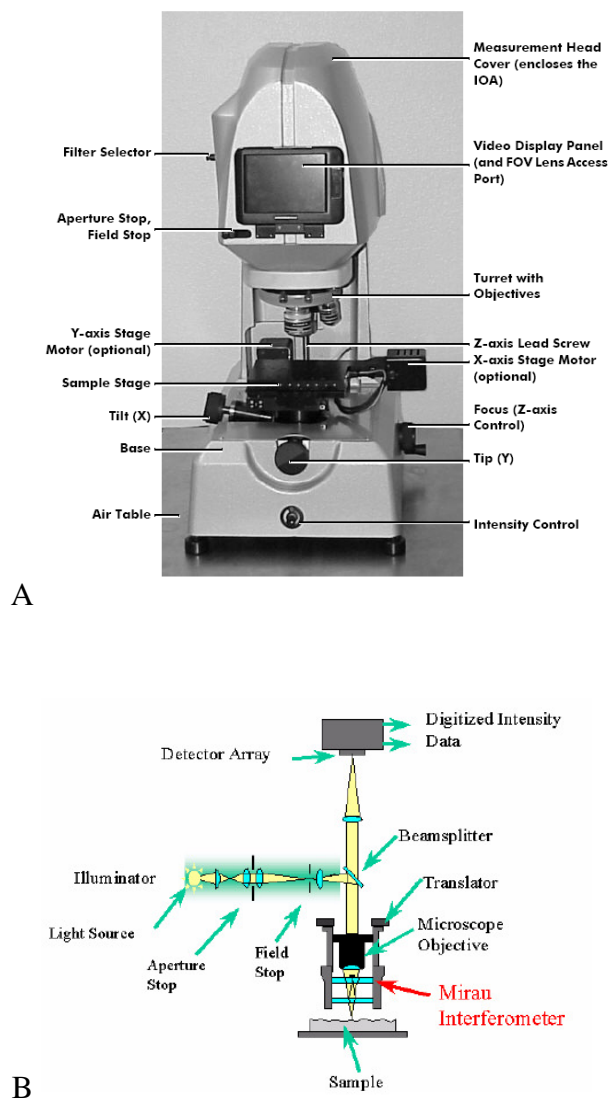


Figure 3.7 (a) Annotated photograph of the Wyko NT1100 (b) schematic diagram of the inside of (a), both taken from the Wyko techniques manual .[85]

Figure 3.7(b) shows a diagram of the inside of the Wyko NT1100, where the light from the illuminator travels through the Integrated Optics Assembly (IOA) and is reflected down to an objective by a beamsplitter. Once the light reaches the objective, another beamsplitter separates the light into two beams. One beam, the reference beam, reflects from a smooth reference mirror in the objective, while the other (the test beam) reflects from the surface of the sample, in this case the optical fibre, and back to the objective. If the surface of the sample is in focus, the two light beams will recombine and form an interference pattern of light and dark bands called fringes. The number of fringes and their spacing depends upon the relative tilt between the sample and the reference mirror. If the sample and the reference are parallel, only one large fringe will be seen. In this case, the fringes are said to be nulled. The interference pattern is received by the CCD camera and the signal is transferred to the computer where it is processed to produce a graphical output representing the surface topology of the sample.

There are two types of measurements available with the Wyko NT1100 system. In the first, phase-shifting interferometry (PSI), the bandwidth of the illumination is reduced and a mechanical translation system precisely alters the optical path length of the test beam. Each optical path change causes a lateral shift in the fringe pattern. The shifted fringes are periodically recorded by the camera, producing a series of interferograms. Computerised calculations combine the interferograms to determine the surface height profile. PSI is used for very smooth surfaces, such as mirrors, optics, or other highly polished samples. PSI measurements are not reliable for very rough samples or samples with an average surface roughness greater than 160nm as multiple fringe sets will exist simultaneously. The second type of measurement uses full bandwidth white light and is termed vertical scanning interferometry (VSI). This technique was developed to

measure samples with much greater surface roughness. An internal translator scans downward during the measurement as the camera periodically records frames. As each point on the surface comes into focus, the modulation on that point reaches a maximum, and then tapers off as the translator passes through focus. By recording the height of the translator at maximum modulation, the system can determine the height of each pixel. The maximum scan length for VSI using the NT1100 is 2 mm.

3.2.5 Goniometry

As has been seen previously, measurement of a contact angle must be accurate and reproducible. One of the most common techniques for measuring contact angle is the sessile drop technique. In this approach, a droplet of liquid (usually water) is placed onto the surface of a sample. The contact angle is then measured automatically by a computer linked to a digital optical microscope. The basic arrangement of this approach can be seen in Figure 3.8.

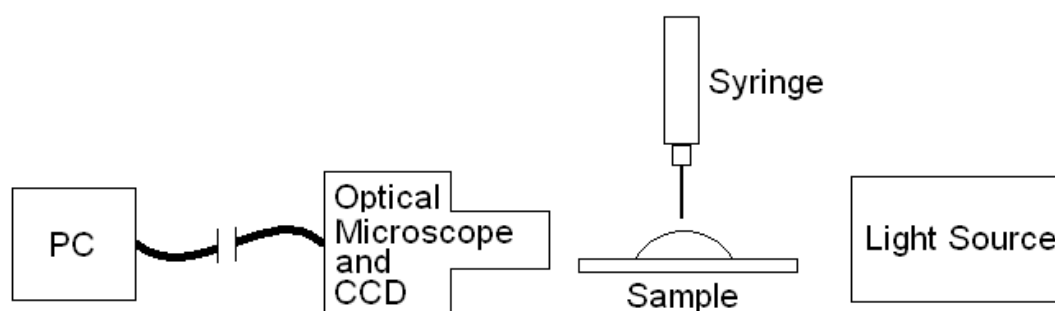


Figure 3.8. Arrangement of sessile drop contact angle measurements using a video tensiometer.

Although a sessile contact angle gives a good indication of the wettability of a sample, it does not indicate how a droplet will move over the surface of the sample in a real life

application. The most basic approach to measuring the dynamic properties of a droplet on a surface is to measure the roll-off angle of the droplet. To do this, a droplet is placed on the surface of a sample which is then tilted until the drop begins to move under its own weight. The angle of tilt of the surface at this moment is the roll-off angle. It is usually found that the roll-off angle decreases as the wettability and contact angle of a surface increase. This is simply because there is less contact area for the drop to adhere to the surface.

3.2.6 Spectrophotometry

Part of this project investigates the reflectivity of surfaces. Primarily, the reflectivity of a surface is quantified using a spectrophotometer. This device allows the reflectivity or transmission of a sample to be measured at a range of wavelengths ranging from the ultraviolet (UV) to the infrared (IR). This results in the production of a reflectivity or transmission spectrum. An example the reflectivity spectrum of a number of metal surfaces can be seen in Figure 3.9.

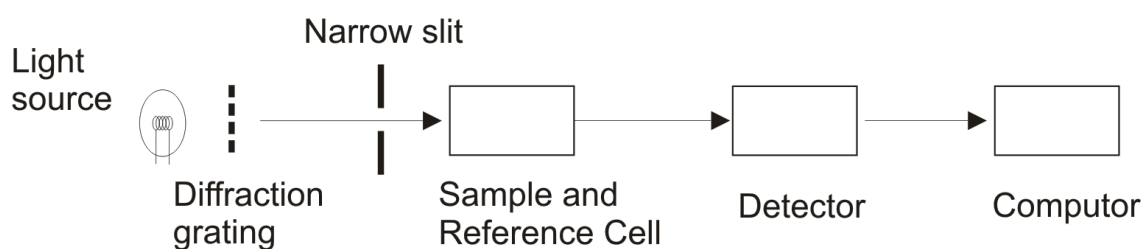


Figure 3.9. Schematic diagram of a single beam spectrophotometer

Figure 3.9 is a schematic diagram showing the principle components of a single beam UV-visible spectrophotometer [86]. A hydrogen or deuterium lamp is used for the UV

region and a tungsten or halogen lamp for the visible region. In this way light radiation from the whole range is scanned by the spectrophotometer. The light is then diffracted through a grating, which splits the light to a number of different wavelengths. Each wavelength is then allowed to pass through a narrow slit to the sample/reference cell as shown in Figure 3.9. The reference and sample cells are placed into the spectrophotometer individually. Light is then passed through each cell in turn and the transmitted radiation is detected and the spectrophotometer records the absorption spectrum of the desired wavelengths of light. Two beam instruments are also used and scan both the reference and sample cuvettes simultaneously.

In particular, this project used an integrating sphere to aid in the measurement of light reflected from laser processed samples. A schematic of this apparatus can be seen in Figure 3.10. Integrating spheres allow the light reflected from the measured surface to be diffused inside the sphere so that both specular and diffuse

reflections are taken into account. This gives a more accurate measurement of surface reflectivity.

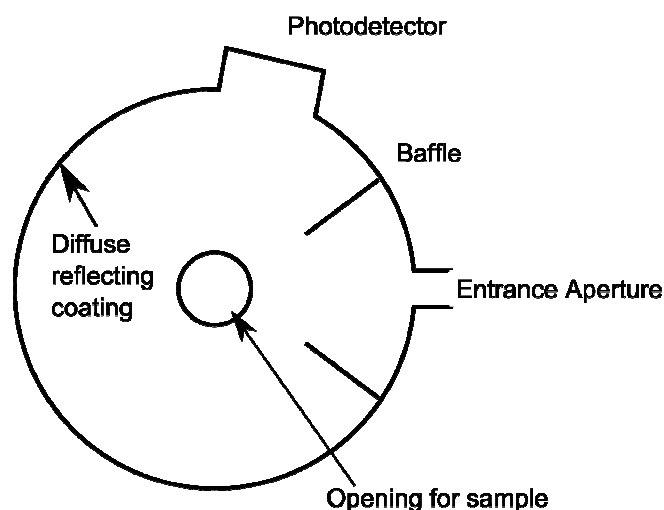


Figure 3.10 Schematic of an integrating sphere which can be used in conjunction with a spectrophotometer in place of a sample or reference cell.

3.2.7 X-Ray Diffraction.

X-Ray diffraction (XRD) is a non-destructive method which can reveal the crystallographic structure, chemical composition and other physical properties of materials and thin films. This is done by directing a beam of X-Rays towards a target sample and measuring how incident X-Rays are elastically scattered.

Unlike other technologies such as energy dispersive x-ray spectroscopy (EDX), which can be used in conjunction with a SEM and identifies the elements present in a sample, XRD can help identify the compounds present. This is important because many compounds can contain the same elements in different arrangements, changing their properties. A well known example of this type of problem is carbon. Depending on the arrangement of the crystal structure formed by carbon atoms, different compounds can be formed. Two of the most well know of these are Graphite and diamond. Although these materials are chemically identical, their properties are almost completely opposed. Diamond is the hardest material known and can be perfectly clear while Graphite crumbles easily and is usually black. These differences in properties are due to the arrangement, or crystal orientation of their atoms. There are hundreds of these naturally occurring arrangements of atoms. However, much work has been done to understand these structures and how they are arranged in crystals [87] and now it is possible to use software to identify the compounds present in materials after XRD measurements have been taken.

In this project, XRD is primarily used to identify the compounds present in thin layers at the surface of metals. These layers are typically in the order of nanometers in thickness. This means that to differentiate them from the bulk material of the sample is

very difficult. One method which has been developed to do this is small-angle X-ray scattering [88]. This technique uses X-rays to graze the surface of a sample by directing them at a very low ($\sim 3^\circ$) angle. This means that although the chemical composition of the substrate is still seen, the compounds present in thin layers on the surface can also be identified more easily.

4 LASER GENERATION OF SURFACE STRUCTURES

The most commonly noted applications of industrial lasers are those such as laser cutting and welding. While these techniques have enjoyed great success, the laser is a much more versatile tool. Due to the special qualities of laser light, it is possible to finely control the output of a laser. This allows laser users to damage a surface in a controlled fashion, producing surface microstructure that differs in both composition and morphology, resulting in the development of unique topographical patterns on the surface. The topographical patterns, or surface microstructures can be produced with scales in the micrometer to nanometer regimes. The majority of laser microprocessing is performed by removing specific volumes of a material surface by ablation. In this project a different approach has been taken. Rather than directly removing target material to produce structure, here the majority of experiments concentrate on the melting and movement of material. Building on the work of researchers such as Dolgaev *et al* [17, 56, 57], Kazakevich *et al* [58] and Vorobyev *et al* [89, 90], the possibilities of producing surface structures by more organic methods have been explored. This chapter gives an account of the development of these quasi self-assembled laser induced microstructures.

4.1 Experimental Methods

The general processing method which was used to produce the surface structures was held approximately constant however, slight alterations were necessary when switching from different laser systems. In general, the laser beam was raster scanned over the

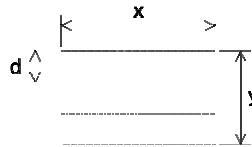
surface of the target material using a computer controlled galvo-scanning system, which was equipped with a flat-field lens.

When scanning the laser over the surface of the sample there were several parameters which could be controlled these were the average power of the laser, P_{AVG} , the scanning speed of the laser, V , and the distance between each line of the scan. This parameter is called the hatch distance, d . Other parameters such as the laser repetition rate, ν and the laser spot size, $2\omega_0$, were held constant. By varying the scanning speed, V , it was possible to change the number of pulses, N , which were fired at each individual point on the target surface. If very large numbers of pulses per spot were required, multiple passes were needed to give the total number of pulses per spot, N_T . To calculate the value of N for each pass, the equation used was:

$$N = \frac{2\omega_0 \nu}{V} \quad 4.1$$

This equation gives the total numbers of pulses along a single scan line. If it is required that the number of pulses fired at a given area, N_A , is calculated, Equation 4.1 can be modified to:

$$N_A = N \left(\frac{x}{2\omega_0} \right) \left(\frac{y}{d} \right) \quad 4.2$$



where the values of x and y are the dimensions of the total scan area as seen in the illustration accompanying Equation 4.2. In the following sections the types of microstructures produced using various laser systems are described. Each section will describe the laser being used and the results obtained.

4.2 Development of textured surface topography using 532 nm Violino Green Marker

The Violino Green Marking laser system is primarily a frequency doubled Nd:YVO₄ diode pumped solid state laser. This type of laser has become very common due to its small footprint and low maintenance requirements. The beam delivery system employed in the Violino systems is that of a scanning galvanometer head and was equipped with a flat field lens with a focal length of 150mm. This means that the laser beams can be scanned rapidly and accurately over the target surface.

The image in Figure 4.1 shows the Violino green marking system it has the output parameters;

Repetition rate: 30 kHz

Pulse width: ~ 7ns

Maximum Output power: 7 W

Wavelength: 532 nm

Focal Spot Size: 55 μ m



Figure 4.1 The enclosure which houses the Violino Marking System

The Violino Green system is very useful as a tool for scientific experiment. It is a relatively simple machine to operate, however, the inclusion of a scanning galvanometer in its design means that very accurate manipulation of the laser beam over a target surface can occur. Initially, the experiments conducted with the Violino Green laser investigate the findings of previous papers [17, 56, 58]. This includes the formation of microstructures on metals in various metals in both liquid and gaseous environments. Once this work had been reproduced, comparisons were made between previous works and those performed for this project.

4.2.1 Comparing Production of Microstructures in Gaseous and Liquid Environments.

In this experiment the 532nm Violino system was used to process AISI 304 stainless steel samples in liquid and air environments. This was done to make a comparison of both the distribution and size of features that are produced. The liquid environment was a mixture of deionised water and ethanol in the ratio 3:2 (deionised H₂O:Ethanol). This mixture was chosen because the addition of ethanol lowers the density of the liquid environment, increasing the ease with which any bubbles produced during processing are moved out of the path of the incoming laser beam.

When $V=1\text{mm/s}$ and $\nu=30\text{kHz}$, $N=1650$ pulses. For this reason, seven passes were made so that the total number of pulses fired at each spot was ~ 11550 . The hatch distance between scan lines was $25\mu\text{m}$. This was chosen so that there was a $\sim 33\%$ beam overlap between consecutive scans. Both samples were processed at a fluence of 19.64Jcm^{-2}

In the two different environments, after a total of ~11550 pulses had been fired at a stainless steel surface in a raster scan, the structures that can be seen in Figure 4.2 were produced. All scales being equal, the most obvious difference between the structures formed in air and those formed in liquid is the feature size. In liquids, the features have a size of 10–20 μm . In air, the feature size rises to 40–50 μm , approximately the spot size of the laser beam.

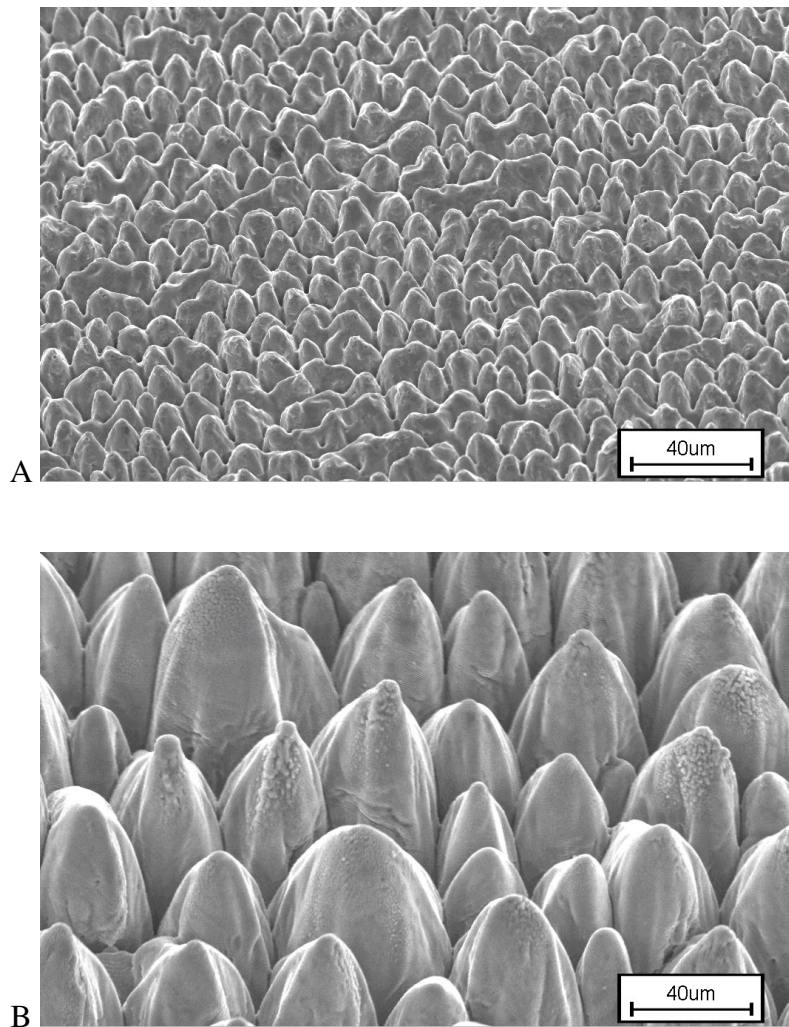


Figure 4.2. Stainless Steel machined in a) Ethanol and water b) Air

In addition to the increase in feature size, the shape and arrangement of the structures also changes. In a liquid environment, the structures are smaller, notably more rounded

and their distribution more random. In air, the structures are, although larger, more closely packed and their arrangement more linear, their period closely matching the laser spot size. This change in distribution can be seen in Figure 4.3.

It is thought that the reason for the change in feature size and distribution is the result of a number of different factors. The depth of liquid above the sample surface was approximately 5mm. The presence of this layer will have affected the formation of

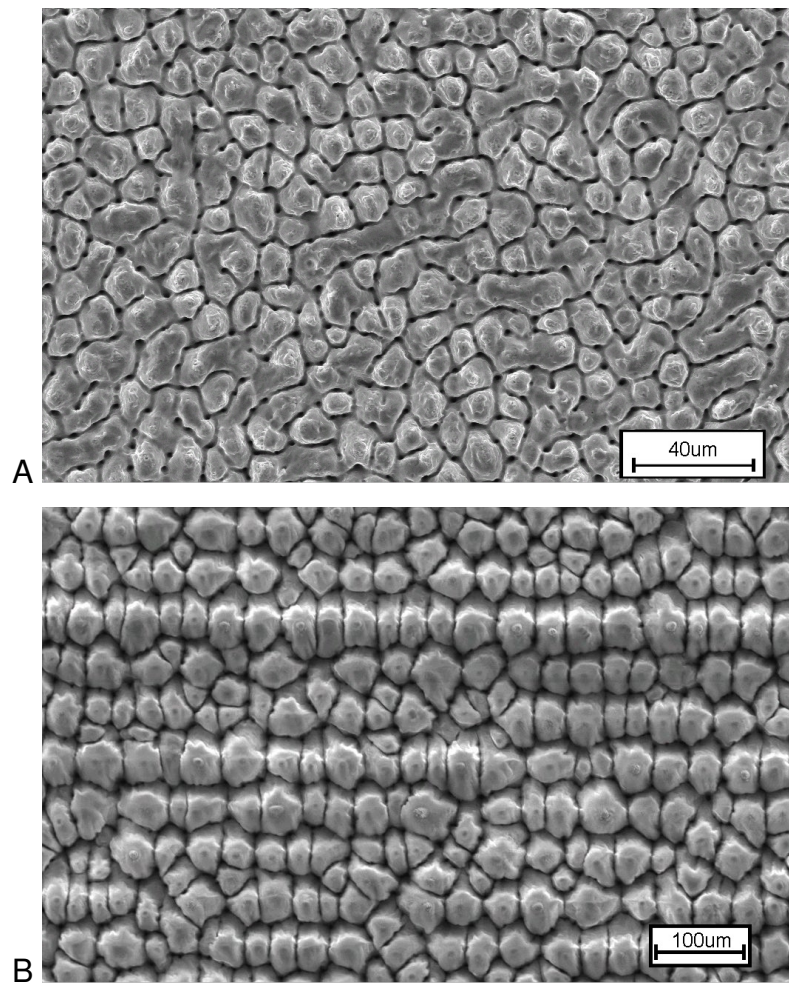


Figure 4.3. Structures produced in water (A) and Air (B). In these images, the scale bars are 20 and 50µm respectively. This change in feature size is related to the environment in which the surface is processed. Indeed this is believed to be the case when discussing the orientation of features also.

surface structures in several ways. It is known that laser power will be lost due to reflection at a liquid – air interface and through absorption by the liquid itself. It is known that at an abrupt change of refractive index, approximately 4% of incident light

is reflected. In this case this would reduce the effective laser fluence to approximately 18.8 Jcm^{-2} . Another loss will be due to absorption by the liquid. Fortunately this will be negligible for two reasons. Firstly, water is almost 100% transparent at 532nm, and secondly the distance light has to travel to reach the target surface is very short.

If the reason for this change in feature size is not because of reflection losses, there are a few more candidates. The liquid will have an effect on the temperature which the surface reaches, cooling the surface to a higher degree than air. This cooling would impede the flow of energy into the surface, reducing the efficiency of ablation. Although it was noted that a plasma was formed below the liquid surface during processing this would also have an effect on the not only the feature size of structures, but also the change in distribution. As a plasma forms, a shock wave is created [91]. In a gas, this shock wave will not affect the incident beam. In a liquid the shockwave will affect the beam indirectly. As the shock wave propagates the variations in pressure will disturb the surface of the liquid. Effectively this changes the angle of the surface, slightly scattering the laser beam. After the multiple passes which took place in this experiment, it is not surprising that the distribution of structures deviated from following the laser scan path. Having said this, there is much work that can still to be done to fully understand the subtle differences between these processes. Most importantly, to fully understand the change in feature size.

4.2.2 Change in microstructure with increasing numbers of pulses in air

The dependence of structure formation on the total number of pulses fired at the target was investigated. While using the same processing parameters as used in Section 4.2.1, the number of passes was increased from one ($N_T=1500$ pulses) to seven ($N_T=10500$

pulses). This was done to determine the number of pulses which are required to develop the structures seen in Figure 4.4.

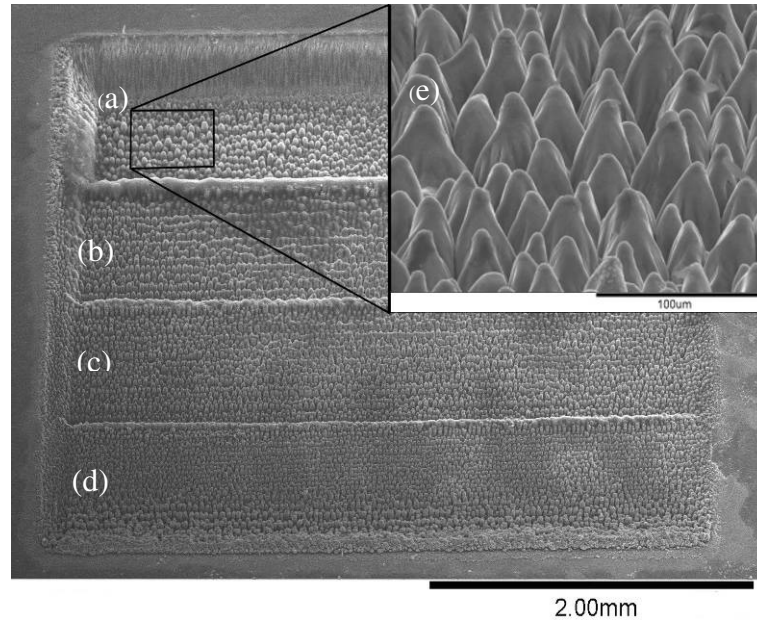


Figure 4.4. Scanning electron microscopy (SEM) images (view tilt 45°) of the target sites where the number of pulses per spot, N_T , have been changed (laser wavelength 532 nm, intensity 1.5 GW/cm², beam spot diameter $\sim 50\mu\text{m}$, distance between the subsequent lines $\sim 25\mu\text{m}$). From top to bottom, N_T is (a) 10500, (b) 7500, (c) 4500, and (d) 1500, with average tip-to-tip distance of 50, 41, 35, and $30\mu\text{m}$, respectively. Inset (e)—view tilt 75° is the enlarged part of the Fig. 5.04a. Exposed areas look like black regions on a bright steel surface

Figure 4.4 shows a SEM image of the results from this experiment. It is possible to produce these structures by applying as few as 1500 pulses per spot this can be seen in the bottom of the image in Figure 4.4d. The major change that occurs at the surface as more pulses are applied is its position in relation to the original surface, as can be seen from Figure 4.5. As the total number of pulses, N_T , is increased, the further below the original surface the structures are formed.

It is clear from the formation of structures below the datum of the surface that the laser fluence used to process these samples is unnecessarily high. This was also apparent from the amount of ablated material that fell as particulates around the ablation sites. To

better understand the evolution of these structures as the number of passes increases, this experiment was performed a second time.

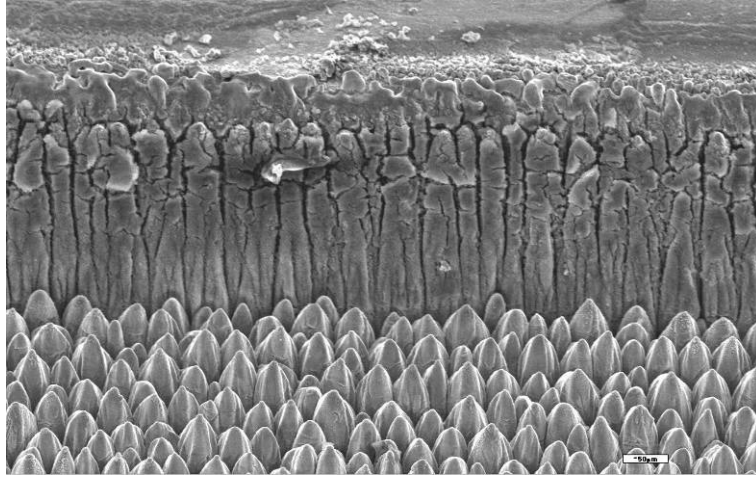


Figure 4.5 SEM Image of microstructures formed in Air when $N_T=10500$. This Image illustrates the position of structures below the datum of the surface. Scale bar 50 μ m.

In the second set of processed surfaces, a fluence of 3.93Jcm⁻² was chosen and the area to be processed was reduced to 300 x 300 μ m. This reduction in area greatly reduced the time taken for processing. All other parameters were kept constant. In total nine passes were made. At a scanning speed of 1mm/s this resulted in 1650 pulses fired per spot. After nine passes, this total is approximately 15,000 pulses. The evolution of the first eight passes can be seen in Figure 4.6. Figure 4.7 shows the surface of stainless steel after nine processing passes.

The images seen in Figure 4.6 and Figure 4.7 give new insight into the formation of this type of surface feature. In Figure 4.6 A and B it can clearly be seen that during the first two passes, melting occurs on the surface. This increased the surface mobility of molten metal and due to the high repetition rate of the laser this material is disturbed and pushed away from the centre of the laser scan path. As increasing numbers of passes are made, material that has solidified to form relatively high points on the surface forms the

tips of the larger surface structures which form during subsequent passes. This can be hypothesised because here the peaks of surface structures are level with, and in some

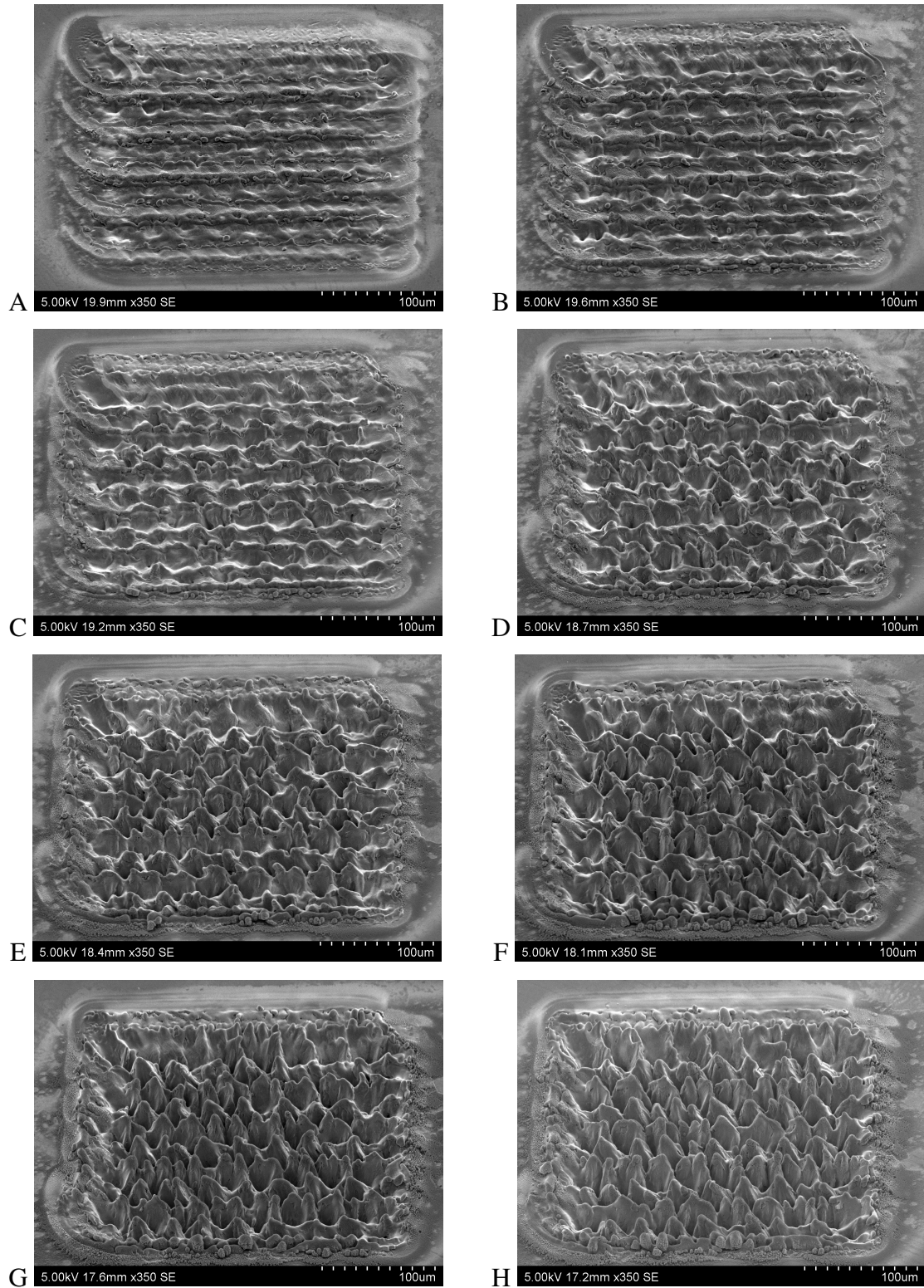


Figure 4.6 SEM images showing the evolution of surface microstructures over nine passes (A – H) with each pass being its own image. The surface is viewed at an angle of 45°

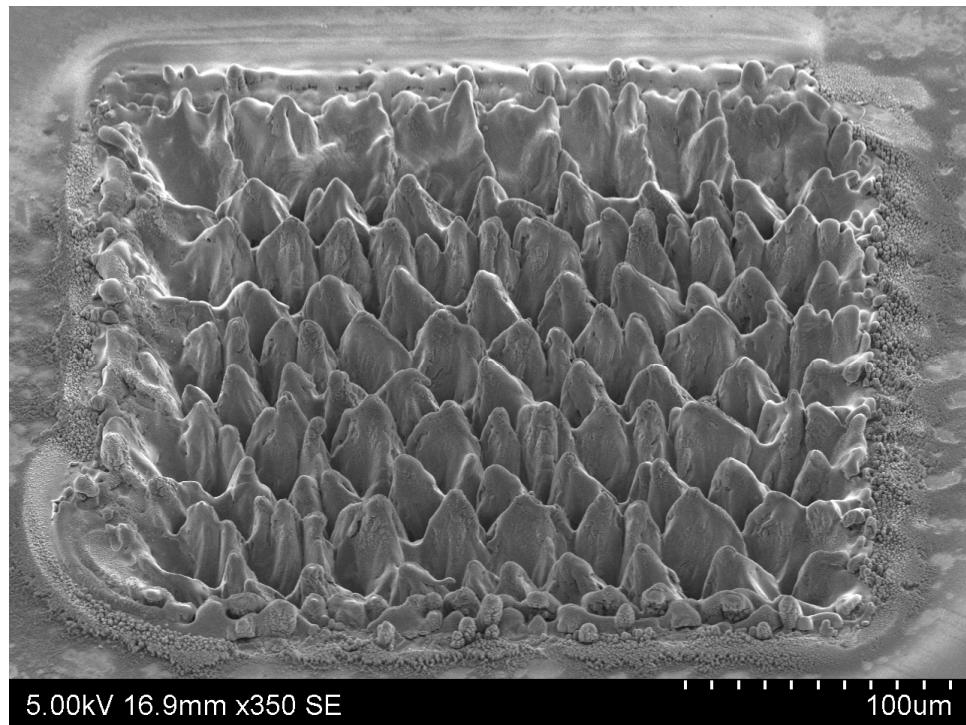


Figure 4.7 SEM image of the surface resulting from approximately 15000 pulses per spot being fired in a raster scanned pattern at a fluence of 3.93 Jcm^{-2}

cases protrude above, the level of the original surface. This raises the question of how the material between these peaks is removed. From these studies it is thought that this material is removed firstly by the flow of molten material towards cooler areas on the surface and then by ablation. The intensities required for this ablation are achieved when the molten surface reflects the incident laser beam from the sides of proto-peaks enabling ablation to occur directly in the path of the laser. Once the peaks are sufficiently well developed, this mechanism acts to only increase the depth of the voids.

One of the problems with this process is the time that is needed to cover large areas. From Figure 4.6 it is clear that after approximately 10,000 pulses (six passes, Figure 4.6 F) have been fired, the overall appearance of the surface structures varies little.

4.3 Laser Micro-topography Modification using 1064 nm EU Marker

The EU Marker system is very similar to the Violino Green Marker. Essentially, this is a lower powered system which is without a frequency doubling crystal. In this particular system, with the same beam delivery system the output parameters are:

Repetition rate: 30 kHz

Pulse width: ~ 8ns

Output power: 4 W (full power)

Wavelength: 1064 nm

Focal Spot Size: 50 μ m

The use of the Violino 1064nm system was necessitated during this project by the breakdown of the Violino Green system. Fortunately this allowed for the continuation of previous work at the fundamental Nd:YAG wavelength of 1064nm.

4.3.1 Change of microstructure as scanning speed is changed.

In the previous experiment, a low scan speed, $V=1\text{mm/s}$, was used. To try and increase the speed of the process, an experiment was performed to investigate the dependence of structure formation on both the scan speed and the number of pulses applied. To do this, an array of targets was machined on both stainless steel and titanium samples. The laser used was the Nd:YAG marker, operating at a wavelength of 1064nm, discussed previously. In these cases, the scan speed and the total number of pulses applied per spot, N_T , were increased incrementally. The scan speeds used were 1, 5, 10, 20, 40 and 60 mm/s. the values of N_T used were 2500, 5000, 7500 and 10000 pulses. This was done while setting the hatch distance, d , to 40 μ m and the fluence to 3.6 Jcm⁻².

It can be seen from Figure 4.8 that the microstructure of the stainless steel does respond to a change in laser scan speed. At a low speed of 1mm/s (Figure 4.8a) it can be seen that the structures, although individual, are not as regular as those already seen. The irregularity is the same as that seen at high laser powers and is the result of the scan

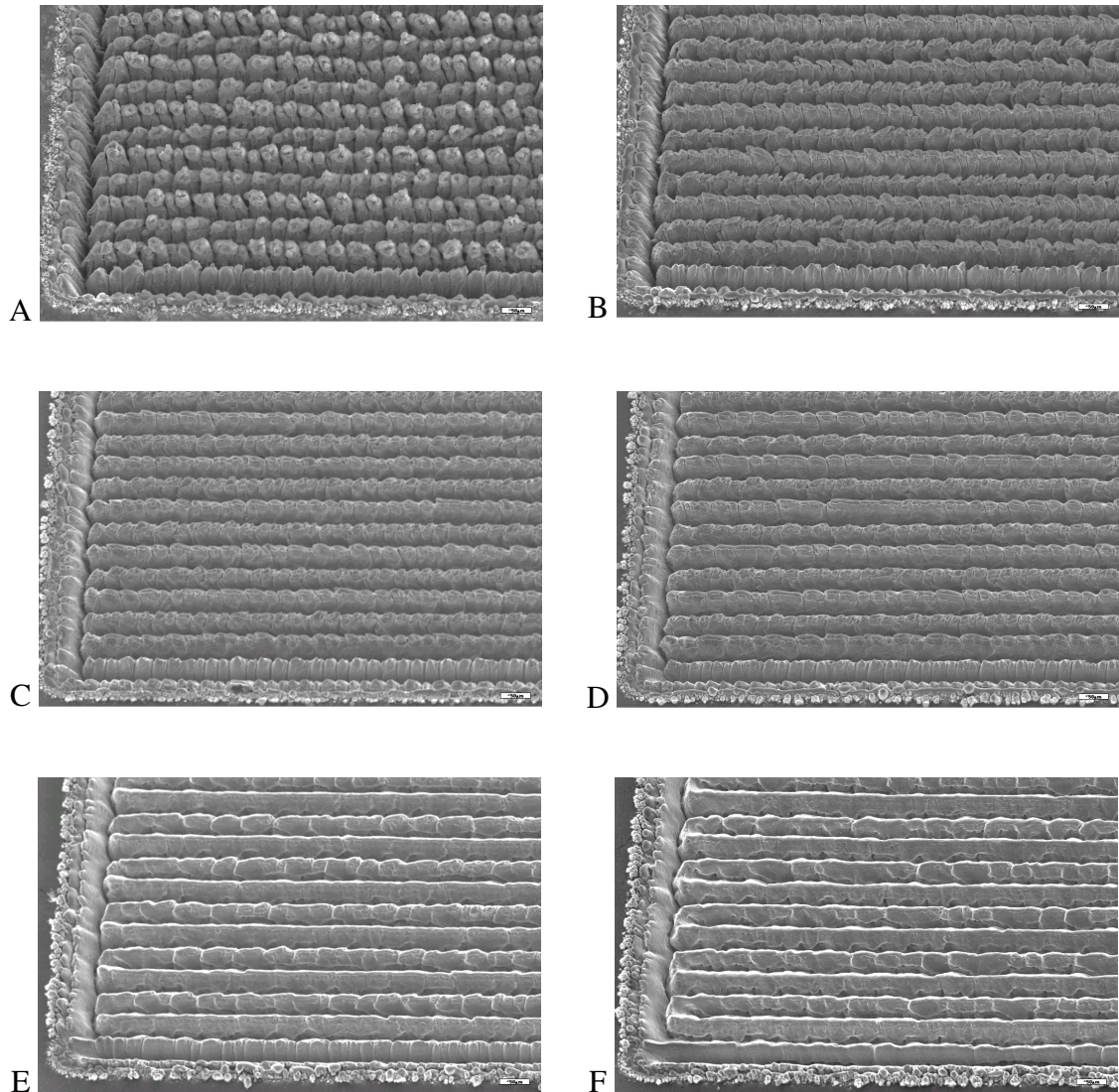


Figure 4.8 a-f. Development of Microstructures as 5000 pulses are deposited onto Stainless steel as the laser scan speed is increased. Left to right, top to bottom, 1, 5, 10, 20, 40, 60mm/s. Scale Bars 50μm

speed being too low. Due to this, too much energy is delivered to the surface and rapid oxidization occurs. As the speed increases to 5, 10 and 20 mm/s, more regular features,

such as those which are desired become apparent. At speeds of 20-60 mm/s, the structures become more linear in appearance. This is because the scan speed is now so high that there is not enough energy being delivered to the surface as the laser scans. From these images it was decided that the most separate and regular structures would be produced at a scan speed of approximately 10 mm/s.

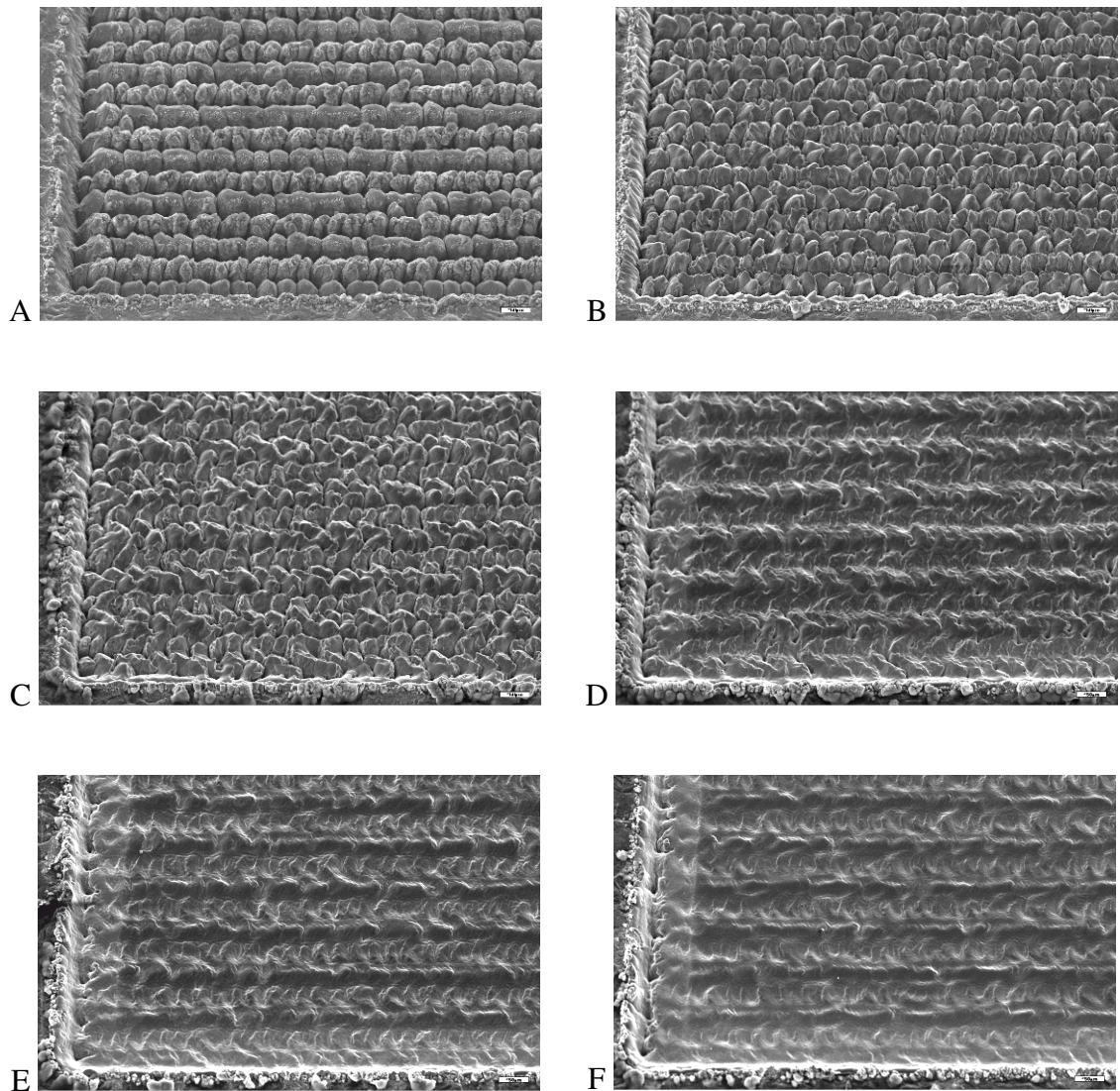


Figure 4.9 Development of Microstructures as 5000 pulses are deposited onto Titanium as the laser scan speed is increased. Scanning speeds A – F are 1, 5, 10, 20, 40, 60mm/s respectively. Scale Bars 50 μ m

If we now turn our attention to the same experiment performed using a Titanium target. Similar results can be seen, however structures are not as erratic at low scan speeds. Again, it would seem that the most regular structures are produced at scan speeds of 5 – 10mm/s. This would suggest that with the repetition rate used, there is an optimum number of pulses that should be fired at the target in a given time period. This allows the structures to form, but doesn't heat the target so much that vaporization takes place. It can also be seen from Figure 4.9 that at scan speeds above 10 mm/s, too few pulses are delivered to the surface. From the appearance of the structures, each pass of the laser simply melts the top layer of the target. Although it was seen that larger numbers of pulses do start to develop microstructure, they were in the form of holes in the surface and took far too many pulses to develop.

4.3.2 Effect of average laser power on structure formation.

Operating at 1064 nm, one of the first investigations that was carried out using this laser was to discover what effect the average power of the laser had on structure formation. This was done so that the best laser power for structure formation could be found. The laser parameters used were $V=1\text{mm/s}$, $d=40\mu\text{m}$ and $N_T=4500$. The maximum average

Laser Power / %	Average Output Power / W	Fluence / Jcm^{-2}
100	4.18	14.19
90	3.40	11.54
80	2.62	8.90
70	1.84	6.25
60	1.06	3.60
55	0.67	2.27

Table 4-1. Average laser output power and fluence as a percentage of the full laser pump power. The results from processing at the various average powers can be seen in Figure 4.10.

power of the laser was measured to be 4.18W when being computer controlled at 100%.

The increments in average power were those seen in Table 4-1.

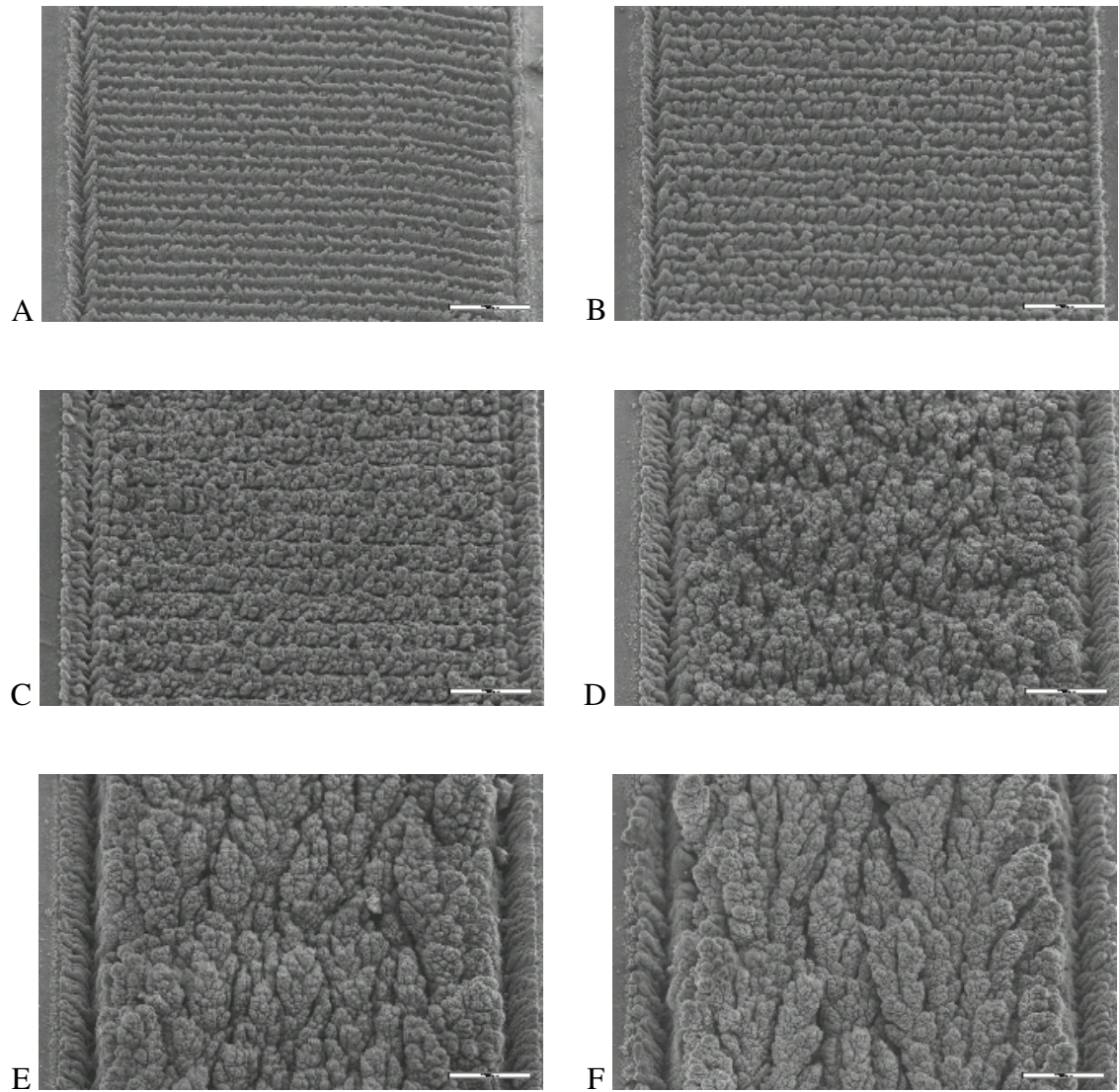


Figure 4.10 A-F, Samples of stainless steel raster scanned at average powers of 0.67, 1.06, 1.84, 2.62, 3.40 and 4.18W. Scale Bar 200µm

It can be seen from these images that as the average power of the laser increases, the structures become larger and less periodic. Until eventually, the structure that can be seen is more like a large oxide formation than the regular structures which were seen before. From this experiment, it was decided that an average laser power of 1.06W was to be used.

4.3.3 Influence of Hatch Distance on Structure Formation

It was noted from previous investigations that the structures being developed occur between the lines where the laser scans. To look at the effect of the distance between scan lines, the hatch distance, d , scans like those seen in Figure 4.11 were made and the value of d changed incrementally.



Figure 4.11. Diagram to show the meaning of the hatch distance, d .

Using processing parameters of $V=10\text{mm/s}$, $\nu=25\text{kHz}$, $N_T=2500$, and varying the hatch distance between 10 and $60\mu\text{m}$, the structures seen in Figure 4.12 are observed. There are several notable changes to the structures as the hatch distance is increased. The first of these is that when the hatch distance is small, $10\text{-}20\mu\text{m}$ ($2\omega_0 > d$), the structures that are produced are much more random in their arrangement and have a feature size which is smaller than the spot size. Increasing the hatch distance to $30\text{-}50\mu\text{m}$ ($2\omega_0 \sim d$) gives the best results in terms of separated features. Once the spot size of the laser is less than the hatch distance ($2\omega_0 < d$) we begin to see how the laser interacts with the target material. The majority of the processing occurs at the centre of the beam, this is where the intensity is highest. As we move away from the centre of the beam, the relative intensity decreases and a melt flow regime begins to become apparent. This can be seen most clearly in Figure 4.12f. Between the scan tracks, the surface of the target has remained undisturbed, while material from the centre of the scan track has been pushed up to form walls at its edges.

A

B

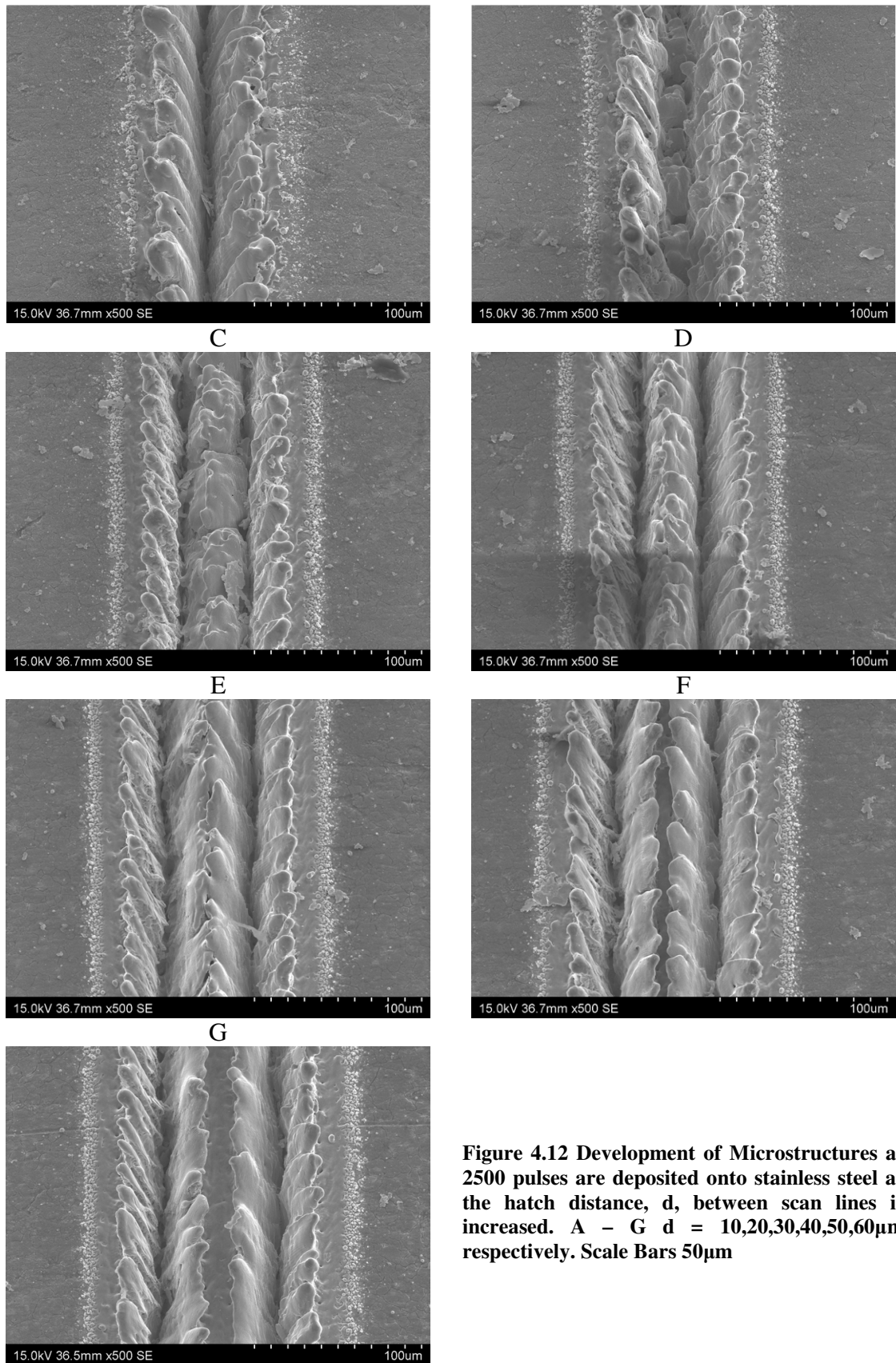


Figure 4.12 Development of Microstructures as 2500 pulses are deposited onto stainless steel as the hatch distance, d , between scan lines is increased. A – G $d = 10, 20, 30, 40, 50, 60\mu\text{m}$ respectively. Scale Bars $50\mu\text{m}$

4.3.4 The Effect of Different Laser Scanning Patterns

Up to now, the laser has been scanned across the surface in a simple raster scan as can be seen in Figure 4.13a. As it had been noted that structures form between the scan lines, it was a logical step to scan the laser in two directions to form individual structures between the scan lines. The scan pattern that was used for this cross hatching regime can be seen in Figure 4.13b.

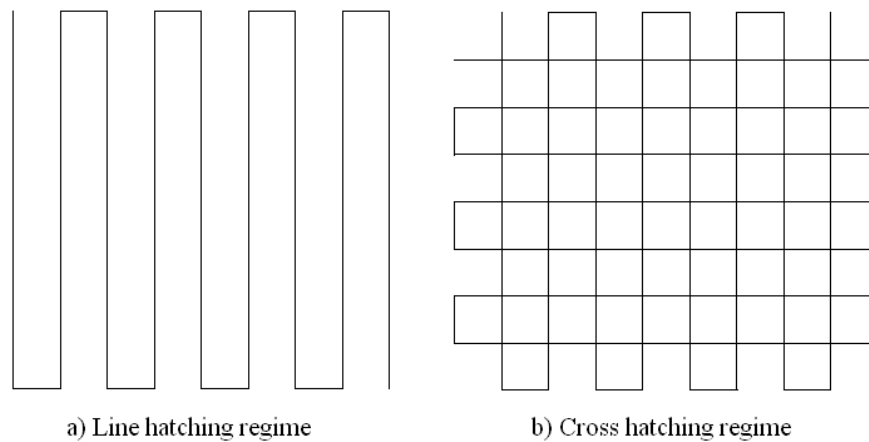


Figure 4.13. Different Scanning patterns used to produce microstructures.
a) Horizontal Line Scanning Regime (HSLR) b) Cross Hatching Regime (CHR)

For these experiments laser fluence of 2 J/cm^2 , intensity of $\sim 0.3 \times 10^9 \text{ W/cm}^2$, was used. The laser beam was raster scanned over the surface of the target at a velocity of 10 mm/s , using a computer controlled galvo-scanning system equipped with a flat field lens. The hatch distance, the distance between adjacent raster scans, was varied for each experiment. Essentially, the overlap between consecutive scans was decreased from 80% of the laser spot diameter on the surface, corresponding to the hatch distance of $10 \mu\text{m}$, to no overlap corresponding to the hatch distance of $70 \mu\text{m}$, each step-change being equal to $10 \mu\text{m}$. Consecutive scans were performed over each area (1 mm^2) so that the required number of pulses had accumulated. In fact, two laser scanning regimes

were employed for the experiments, namely horizontal line scanning regime (Figure 4.13a) and cross hatching regime (Figure 4.13b). In the horizontal line scanning regime (HLSR) the laser was scanned only in the X direction (Figure 4.14a) and the hatch distance was varied between the lines, from 10 μ m (Figure 4.14(a)) to 70 μ m (Figure 4.14 (g)) in steps of 10 μ m. However, in the crossed hatching regime (CHR) the laser was scanned over the surface in two directions (X and Y) to form a grid pattern (Figure 4.15 (a) to (g)). The hatch distance was varied in the same fashion as for the HLSR and was maintained in both X and Y directions. For the HLSR and CHR the total number of pulses fired onto each target surface was calculated to be 2500 and 5000, respectively. The surface morphology of the samples was examined by scanning electron microscopy (SEM). Irradiation of the material in CHR resulted in the formation of structures shown in Figure 4.15. Here the total number of pulses applied to each area was 5000. It is in contrast to the HLSR where only 2500 pulses were applied to each area. As it can be seen from Figure 4.15 (c) to (g), highly organized structures have been formed. Despite the large number of pulses applied, the heights of the structures from Figure 4.15(d) onward are always equal to the ablated layer thickness. Here the distance between the consequent scans were increased from 30 μ m (Figure 4.15 (c)) to 70 μ m (Figure 4.15 (g)), in steps of 10 μ m, in both X and Y directions. As it can be seen from the Figure 4.15 (a) and (b), increasing the overlap between the scanned lines, once again resulted in the severe oblation of the material. No well-defined structures have been formed in these cases.

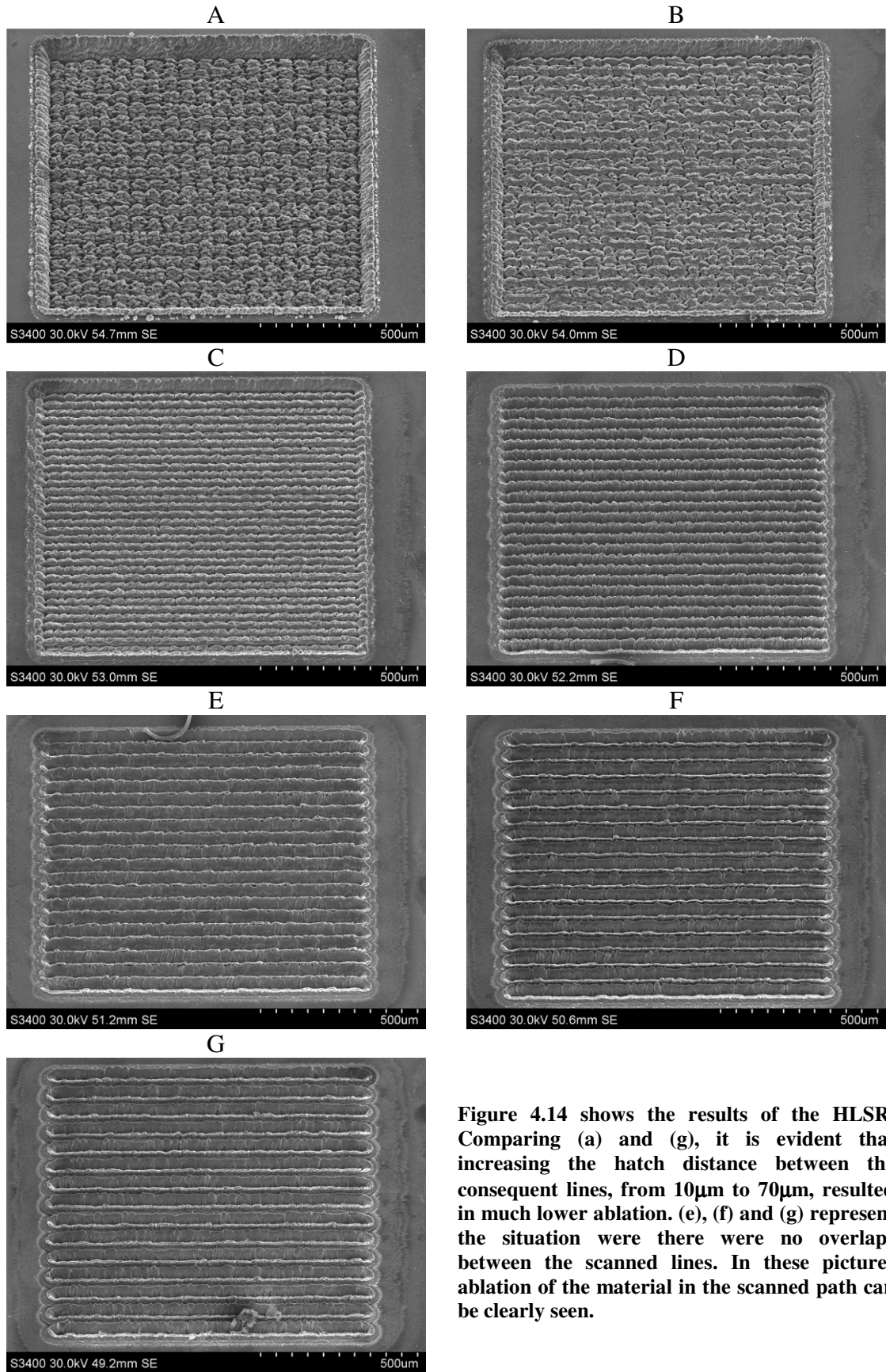


Figure 4.14 shows the results of the HLSR. Comparing (a) and (g), it is evident that increasing the hatch distance between the consequent lines, from 10µm to 70µm, resulted in much lower ablation. (e), (f) and (g) represent the situation where there were no overlaps between the scanned lines. In these pictures ablation of the material in the scanned path can be clearly seen.

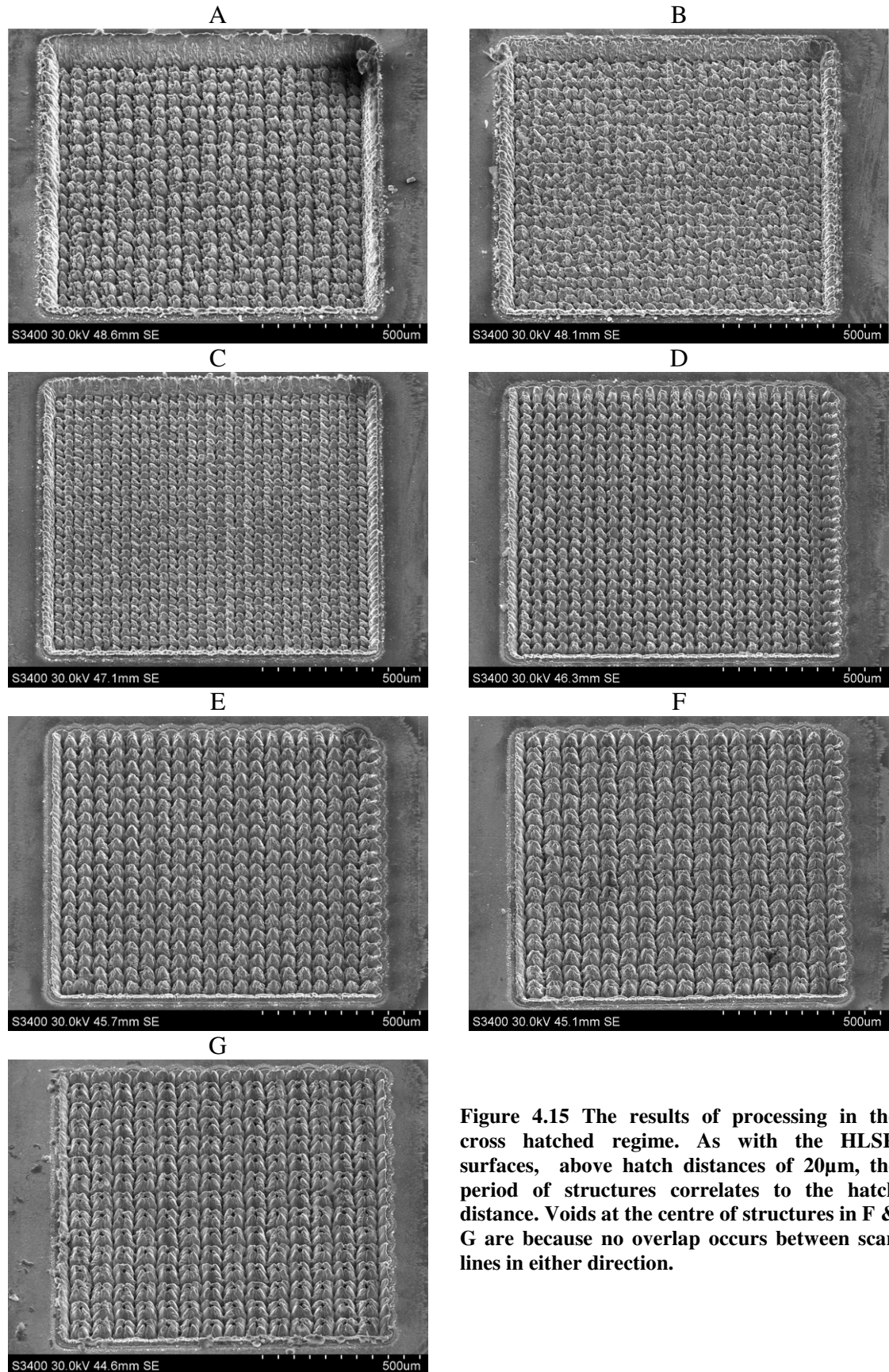


Figure 4.15 The results of processing in the cross hatched regime. As with the HLSR surfaces, above hatch distances of 20µm, the period of structures correlates to the hatch distance. Voids at the centre of structures in F & G are because no overlap occurs between scan lines in either direction.

It is believed that the driving force behind the material removal is the pressure of the expanding ablation products, which are produced at the centre of the laser beam. Owing to the high intensity and good beam quality of the source, ablation occurs at the centre of the laser beam, which is above the ablation threshold of the material. At the edges of the beam, melting occurs. Interaction of the melt with the pressure in the near-surface plasma layer results in hydrodynamic instabilities of the melt. As can be seen in Figure 4.14(e), (f) and (g) some structures have been formed at the edge of the beam. These structures can also be observed in Figure 4.14(c) and (d) where the distances between the consequent lines are 30 and 40 μm . For high level of overlap between the lines, Figure 4.14 (a) and (b), only severe ablation of the materials occurs with the consequence of no defined structure. It is considered that for the plasma produced during our high intensity nanosecond pulse laser irradiation (intensity in the order of $\sim 10^9 \text{W/cm}^2$ and $\tau=7\text{ns}$) deposition of laser energy is nonlocal and occurs below the critical electron density of $N_c \sim 9.7 \times 10^{20} \text{cm}^{-3}$ (The critical electron density is taken equal to $1.1 \times 10^{21} / \lambda_l^2 \text{cm}^{-3}$, where λ_l is the laser wavelength in microns [92]). The absorption of the laser radiation occurs via inverse bremsstrahlung. The duration of the ablation can be considered to be close to the duration of the laser pulse. The heat diffusion length, $l_T \sim 2(D\tau)^{1/2}$ [93], where D is the heat diffusivity ($D=0.04$) and τ is the laser beam dwell time ($\tau=7\text{ns}$), was calculated to be approximately equal to 33 μm . This value is smaller than the laser spot diameter on the target ($\phi \sim 50\mu\text{m}$), and hence the lateral heat flow can be substantially confined [48, 92]. It is worth mentioning that the nonlocalized absorption of the radiation results in the heat transport to the target and hence makes accurate energy deposition difficult. It is known that in the absence of definite polarisation of the laser beam and spatial modulation of the radiation intensity (in this case achieved owing to the good beam

quality of the source) melt instability in the field of ablation plume pressure results in the growth of large-scale surface structures with a characteristic period of $\sim 20\text{-}30\mu\text{m}$ [94]. In the range of irradiation parameters here (intensity in the range of $\sim 10^9\text{W}/\text{cm}^2$, or in general intensities in the range of $10^8\text{-}10^{10}\text{W}/\text{cm}^2$, and pulse durations in the range of $<10\text{ns}$), formation of these structures is due to a spatial modulation of the pressure in the near-surface plasma layer, followed by melt outflow from pits to humps and subsequent solidification. In our experiments, the large depth of field maintained a high irradiance owing to the good beam quality of the laser. Development of the instability requires that large number of pulses are fired onto the target.

4.3.5 Production of angled structures on stainless steel

Both of the lasers used for these experiments used a computer controlled system to direct the laser beam to a desired point on the target. Obviously, this means that the beam is not delivered at an angle normal to the target anywhere except directly below

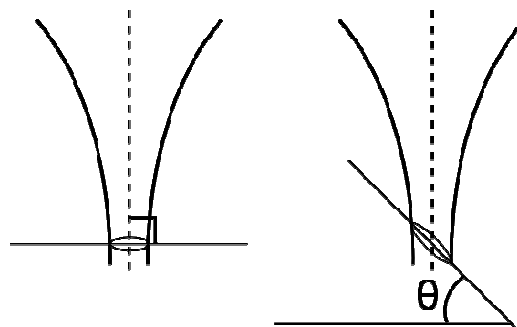


Figure 4.16 Schematic of experimental arrangement to show the change in shape and area of focal spot size as a target sample is tilted by angle θ .

the lens. It was noticed that when a sample was processed in a position which was at the extremity of the available scan area, the structures that were formed were inclined

towards the direction of the incoming beam. This phenomena has also been observed by others working on this process [17]. Unfortunately, although this effect has been reported, a systematic study has not been carried out.

It was calculated that the Rayleigh range and depth of focus of the laser system being used would be sufficient that the same type of processing that has been discussed previously could take place while the target was at an angle. Figure 4.17a-c show laser processing performed in exactly the same manner as seen previously, however the sample was inclined to angles of 15, 30 and 45 degrees, effectively changing the incident angle of the laser beam. This arrangement can be seen in Figure 4.16. It can still be seen that the alignment of the surface structures agrees well with the incident beam angle.

Applying the methodology of scanning the laser over the surface in a grid pattern allowed the structures that can be seen in Figure 4.18a-c to be developed. It was found that the most regular structures are produced when the hatch distance is larger than the laser spot size. One reason for this is that the melt flow can cause unwanted ridges and other anomalous structures when the hatch distance is smaller.

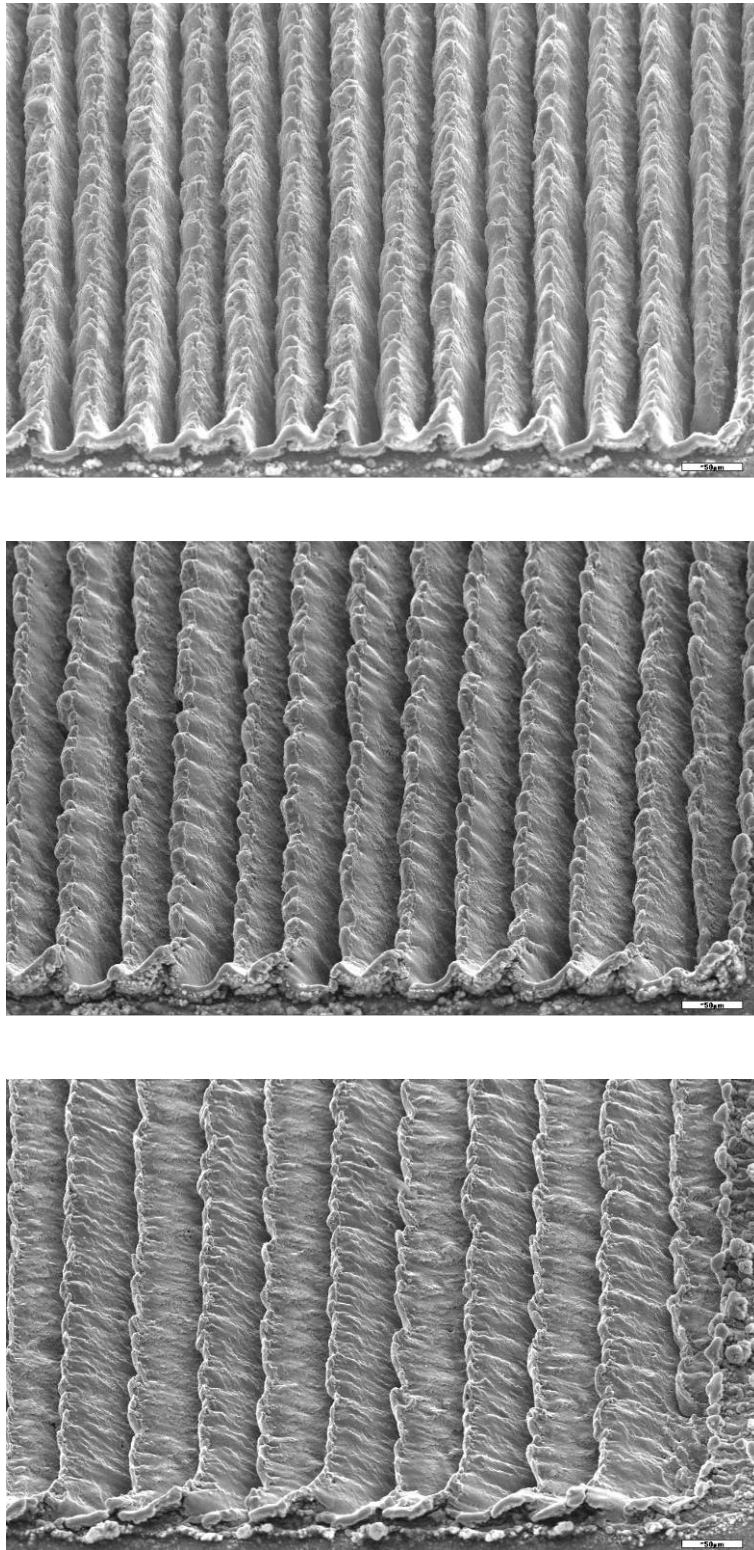


Figure 4.17 Angled Microstructures on stainless steel produced using the line scanning method. Left to right, samples tilted by 15, 30 and 45 degrees. Scale Bars 50µm

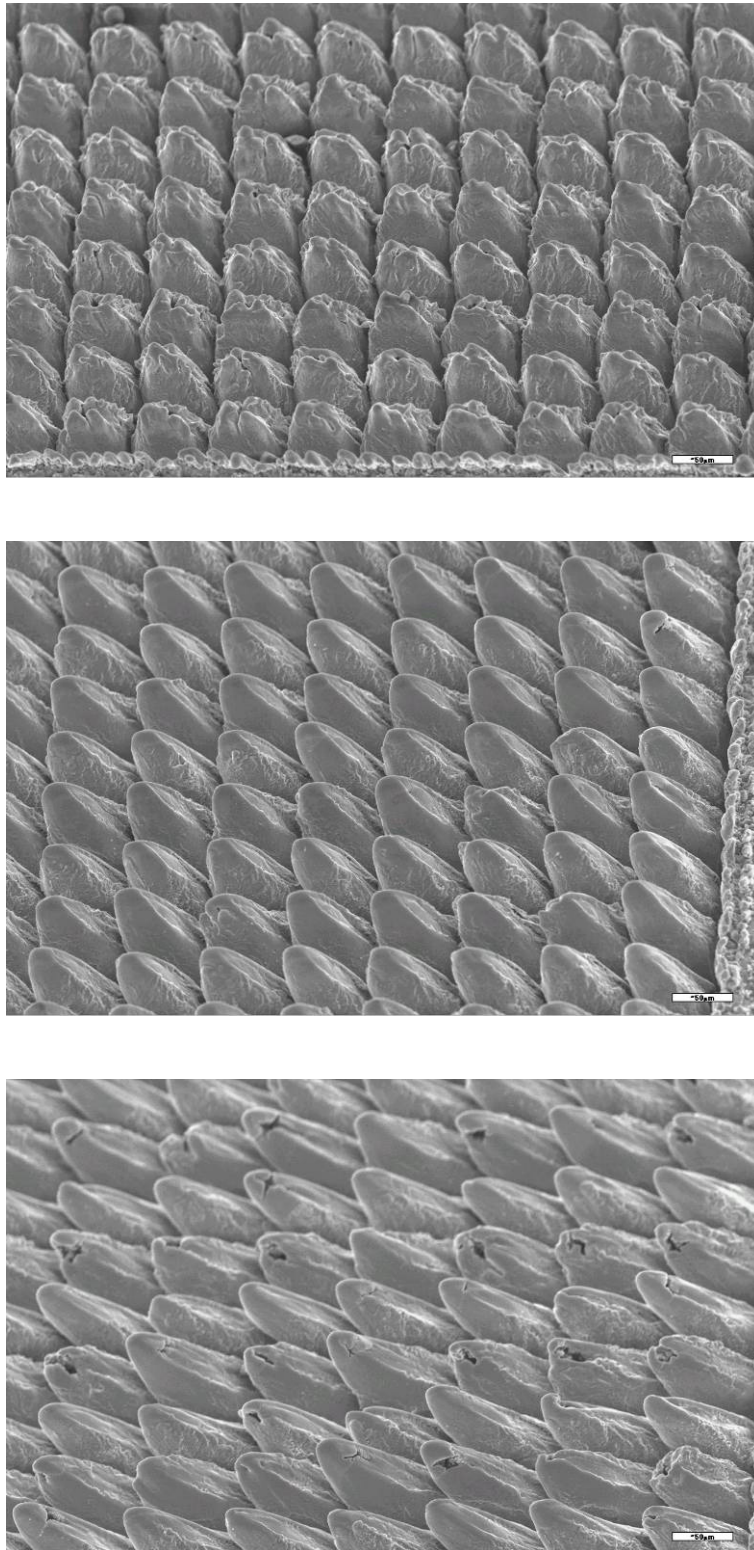


Figure 4.18 Angled Microstructures on stainless steel produced using the cross hatching method. Left to right, samples tilted by 15, 30 and 45 degrees. In all cases the hatch distance is 70µm. Scale Bars 50µm

As the target surface is tilted to produce these angles structures, the effective fluence at the surface changes with the tilt angle. As this processing is being carried out within the Rayleigh range of the optical system, It is convenient to treat the area around the focal point of the optical system as a cylinder. With this in mind, if the target plane is intersecting this cylinder then the focal spot will be either circular or elliptical. The change in the radius of the ellipse which is projected onto the plane of the target surface as the angle of tilt changes can be described as:

$$\omega_e = \omega_0 \cos \theta \quad 4.3$$

Where ω_0 has its normal meaning and ω_e designates the half length of the variable axis of the ellipse. The area of an ellipse can be calculated by $A_e = \pi ab$ where a and b are the half lengths of the major and minor axis of the ellipse respectively. If we describe this in more familiar terms,

$$A_e = \pi \omega_0 \omega_e \quad 4.4$$

From here the equation for the fluence of a Gaussian beam shown in chapter three can be modified to:

$$F_e = \frac{2E_p}{\pi \omega_0 \omega_e} \quad 4.5$$

At normal incidence, with a fluence of 2 Jcm^{-2} , the relationship in equation 5.5 results in the graph shown in Figure 4.19. In this case only three tilt angles were studied and the specific fluences at these angles can be seen in Table 4-2

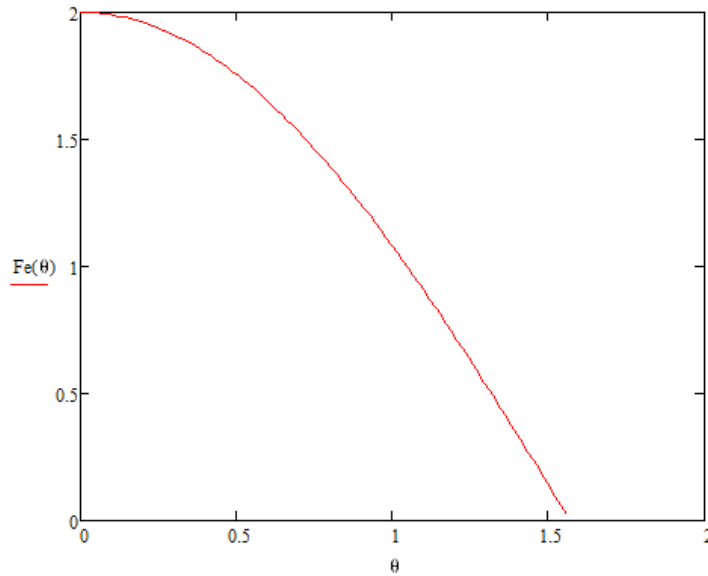


Figure 4.19 Angular dependence of focal spot fluence for target tilt angles between 0 and 90 degrees.

Tilt Angle / Degrees	F_e / Jcm^{-2}	$2\omega_e / \mu\text{m}$
0	2.00	55.00
15	1.93	56.95
30	1.73	63.56
45	1.42	77.90

Table 4-2. The calculated change of Fluence and elliptical spot size depending on target tilt angle.

The effect of this change in fluence can be seen in the topography of the features produced. Figure 4.18 shows structures produced by only changing the angle by which the target is tilted. If the structures are compared to those which were produced when changing the distance between scan lines (Figure 4.15) it can be seen that as the tilt angle increases, the structures begin to show features which would be associated with structures produced at larger hatch distances. This difference is especially apparent between samples tilted at 30 and 45 degrees in Figure 4.18. There are voids present in

the tops of structures of Figure 4.18. This is because the effective fluence is lower and the energy required to fully melt form these structures by melt flow is no longer available due to the increased spot size.

4.4 Laser Micro-topography Modification using Spectraphysics YHP40

4.4.1 The Effect of pulse duration on microstructure formation

Moving on from laser processing using the Nd:YVO₄ laser discussed previously, a Spectra-Physics YHP40-532Q Diode Pumped Solid State (DPSS) laser was used. This laser has a maximum output power of 15W at 1064nm, repetition rate of 30kHz and a pulse duration of 40ns. It is also worth noting that this laser has the option of output wavelengths of 532 and 355nm with the use of frequency doubling and tripling crystals. However, they were not used in this case.

The main difference between this laser and the marking laser used previously is the pulse duration. In comparison to the relatively short 7ns pulses produced by the Violino system, the 40ns pulse duration of the Spectra-Physics system changes the way in which the target surface is heated. In this case the pulse duration is over four times longer. However, the repetition rate of the two lasers are the same.

The similarities of these two lasers lend themselves well to experiments which make a direct comparison of the effect of pulse duration in the nanosecond regime. For this reason initial parameters for laser processing were set to be approximately equal to those which had produced the desired results with the Violino system.

The SEM images below (Figure 4.20) show the surfaces which were formed when the output of the laser was focused to a ~20μm spot. The hatch distance was set equal to the

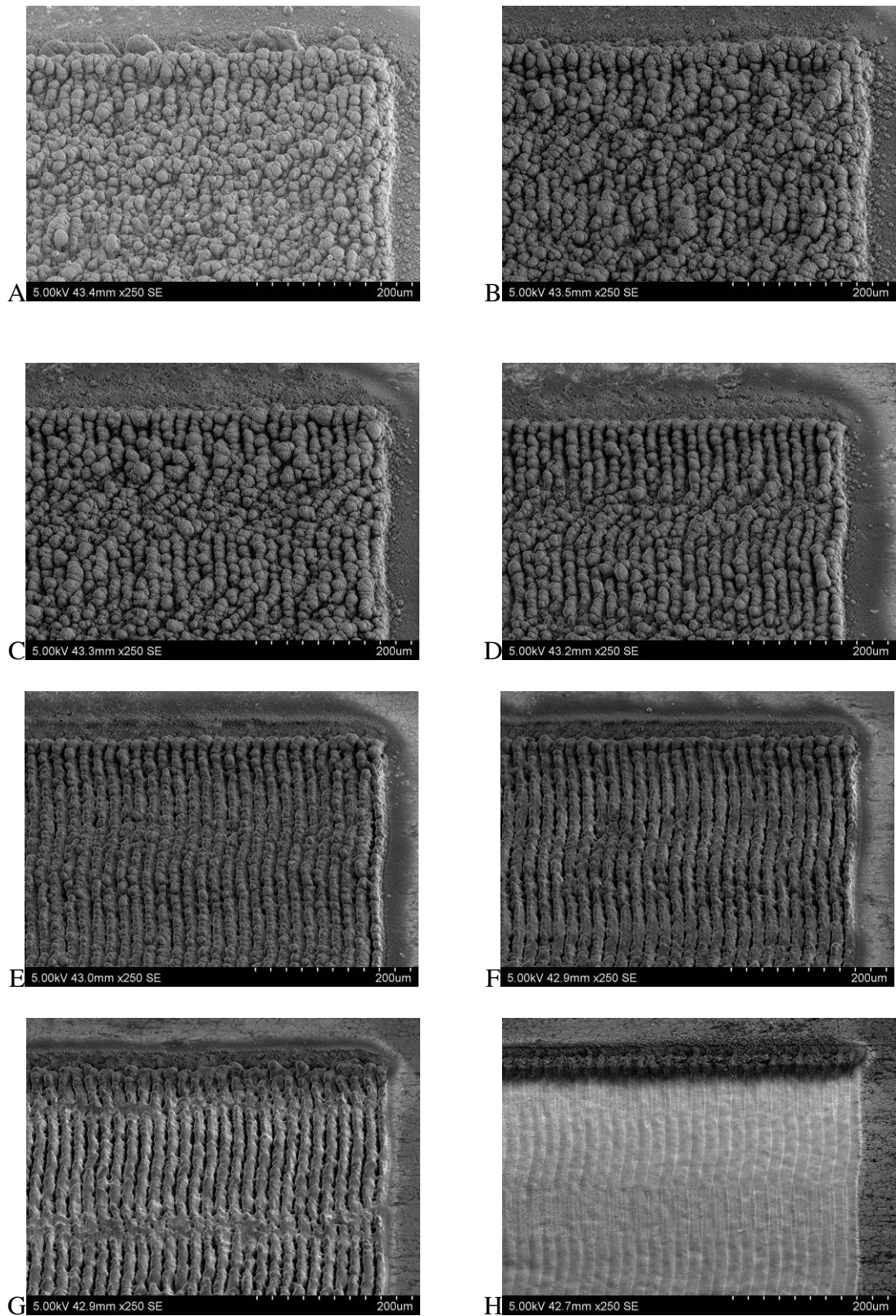


Figure 4.20. SEM images of Stainless steel targets processed using the Nd:YAG Laser. Fluence is varied from 53 Jcm^{-2} (a) to 15 Jcm^{-2} (h) in increments of 5 Jcm^{-2} .

spot size and the scan speed was set at 10 mm/s. The average laser power was increased incrementally from $\sim 15.9 \text{ Jcm}^{-2}$ to 53 Jcm^{-2} . The increment was 5.31 Jcm^{-2} .

Top to bottom the average laser power is being reduced. It is not until fluences of less than $\sim 5 \text{ Jcm}^{-2}$ that anything like recognisable, individual structures begin to form. At powers above this, there is a large amount of oxidisation caused by too much power interacting with the target. Effectively boiling and burning takes place.

The results which are discussed here represent the best results which were found using the Spectra-Physics laser. However, there were a number of problems with respect to producing structures that we have previously discussed using this laser system. The first is that although many efforts were made to produce structures, it was always the case that, with the set-up used, any trenches on the surface were only deepened by multiple passes and structures did not form. Another problem was the stage which was used to manipulate the target. At the speeds that were of interest, what can only be described as a 'wobble' of $\sim 10\text{-}15\mu\text{m}$ was encountered. This is of the same magnitude as the feature size of the structures and definitely did not help during the experiments. If time allows, this section of work will be returned to, and hopefully better results obtained as to the actual effect of increased pulse duration.

4.5 Laser Processing using Coherent Libra Femtosecond Amplifier

Up to now, the lasers which have been discussed have been nanosecond pulsed lasers. These systems have pulse durations which span in the region of 1 to 100×10^{-9} seconds. Femtosecond (fs) systems, as the name would imply, have considerably shorter pulse duration, usually in the region of 100 fs (100×10^{-15} seconds). Femtosecond lasers have been causing quite a stir in the laser processing community in recent years. The reason for this is the way in which light emitted by these devices interacts with a target material. Due to their short pulse durations, even at average powers as low as 1W, intensities in the GW regime can be produced at a focal point. This combination of pulse duration and intensity has very interesting results when materials processing is the desired use. During ns laser ablation, there is enough time during the pulse for energy to be transferred to the atoms surrounding those being directly affected by the incident laser beam. In the case of fs laser ablation, this is not the case. During fs laser ablation there is no time for the energy from the incident laser beam to be transferred to the lattice. The product of this is that ablation can occur at much lower average powers and there is little or no heat affected zone surrounding laser processed areas.

The Coherent Libra system is based upon a Ti:Sapphire laser. Ti:Sapphire lasers are tuneable lasers which emit red and near-infrared light in the range from 650 to 1100 nm. Ti:Sapphire refers to the lasing medium, a crystal of Sapphire (Al_2O_3) that is doped with Titanium Ions (Ti^{3+}). A Ti:Sapphire laser is usually pumped with another laser with a wavelength in the green part of the spectrum. In the case of the Libra system, this is a Coherent Evolution laser. Based on a frequency doubled Nd:YLF laser operating at 527 nm. Ti:Sapphire lasers operate most efficiently at wavelengths near 800 nm. The system arrangement of this laser can be seen in Figure 4.21

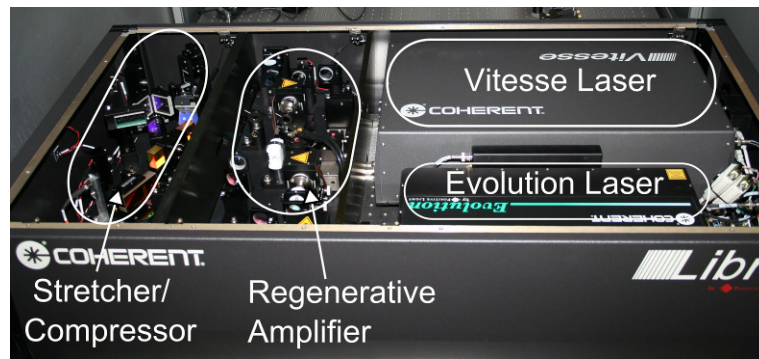


Figure 4.21 Overview of Coherent Libra Ti:Sapphire femtosecond laser system. Two lasers, the Vitesse and Evolution provide the source and pump beams respectively. The regenerative amplifier and stretcher compressor then manipulate these outputs into femtosecond output.

The Libra is designed to amplify very short single pulses typically a few nano-joules to over 1mJ of pulse energy and a pulse duration of ~ 100 femtoseconds. The very short pulses are initially stretched and amplification takes place as the optical pulses pass through a Ti:Sapphire rod which has been optically excited by a laser pulse from the Evolution laser. Normally, amplification in the rod is small but a regenerative amplifier allows multiple

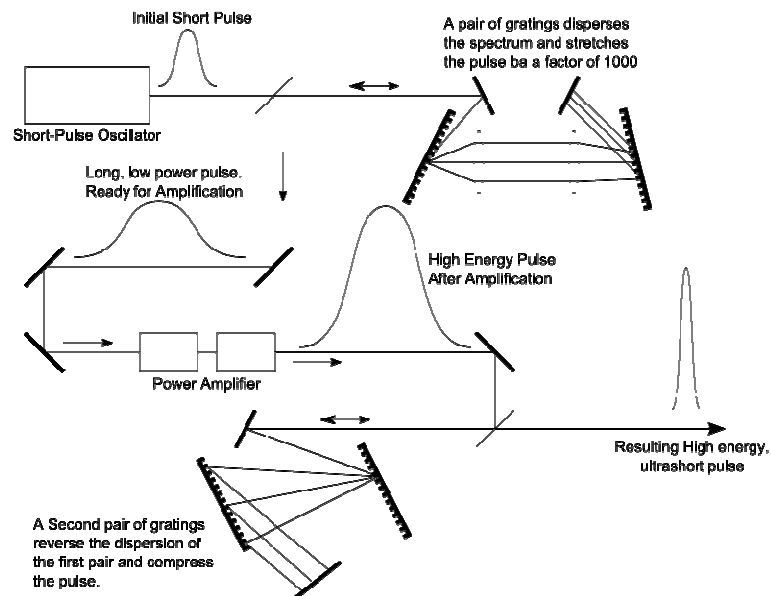


Figure 4.22. Schematic of the Stretcher/Compressor module shown in Figure 4.21. Ultrashort pulses are achieved using this chirped pulse amplification method in the Coherent Libra System.

passes through the rod resulting in a power gain of $\sim 10^6$. Following amplification the pulses are recompressed to a pulse duration on the femtosecond time scale. This process of pulse compression can be seen in Figure 4.22.

4.5.1 Damage Thresholds of AISI 304 Stainless Steel under Femtosecond Irradiation

Femtosecond laser ablation has a somewhat different mechanism to ablation performed using nanosecond pulsed lasers. When nanosecond lasers interact with a metal surface, energy is delivered at low enough rates that it is possible for energy to be transferred to surrounding material by lattice vibrations. Only when a volume of material is saturated with energy does ablation occur. When ultrashort (femtosecond) laser pulses interact with a material, the majority of the pulse energy is absorbed by the electrons with which they interact directly. Having such short pulse duration also means that the intensity of ultrashort pulses is several orders of magnitude higher than during nanosecond pulses. This short pulse duration, coupled with high intensities means that the material that laser light interacts with directly is ablated before energy can be transferred to the surrounding material. This mechanism gives ablation using fs lasers a much smaller heat affected zone and considerably less melting occurs in the area surrounding the interaction zone.

All samples used in this experiment were AISI 304 stainless steel which was ground and polished to a roughness of 25 nm using progressively finer polishing paper from 400 – 1200 grit. Samples were then polished using 1 μ m diamond paste. The final

roughness was evaluated using white light interferometry. The samples were mounted in the focal plane of a single, $f = 50$ mm, lens. This arrangement resulted in a damaged area ranging in diameter between $150\mu\text{m}$ and $20\mu\text{m}$, depending on laser power. The laser used was the Coherent Ti:Sapphire femtosecond laser system ($P_A = 1$ W, $\nu = 1\text{kHz}$, $t = 100$ fs). To calculate the damage threshold using the Beer-Lambert relationship [51], trains of 1, 5, 10 and 20 pulses were fired at the surface at a repetition rate of $\sim 1\text{Hz}$ and at fluences ranging from $13.2 - 0.05\text{ Jcm}^{-2}$ at 800nm and $1.65 - 0.01\text{ Jcm}^{-2}$ at 400nm . The output power of the laser was controlled using combinations of neutral density filters to attenuate the beam. The depths of the craters produced by these interactions were then measured using white light interferometry and the rate of ablation calculated for each laser fluence. The etch rate graph plotted in Figure 4.23 shows the ablation depth per pulse at the various laser fluences and wavelengths used. Incubation and ablation threshold fluence values for AISI304 stainless steel are given by the intersection of trend lines with the x - axis. Table 4-3 gives the numeric values of these threshold fluences.

Wavelength / nm	Incubation Threshold / Jcm^{-2}	Ablation Threshold / Jcm^{-2}
400	0.005	0.077
800	0.013	0.342

Table 4-3 Numerical values of ablation and incubation threshold fluences for femtosecond pulses of 800 and 400 nm wavelengths.

Apart from large scale ablation, resulting in drill holes, which would be expected at higher fluence values, smaller scale structures are also present in the surface areas which interact with the laser beam. Target sites which were subjected to fluences which fall between the incubation and ablation threshold show both micron scale and sub-wavelength structure.

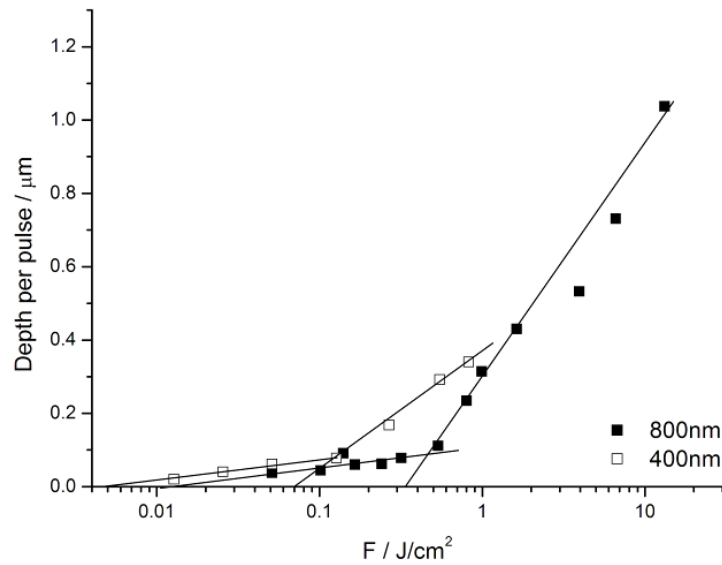


Figure 4.23 Ablation depth per pulse relationship for AISI 304 Stainless steel during femtosecond ablation at 40 and 800 nm.

4.5.2 Microstructure Production using Femtosecond Lasers

There are several simple experiments which were undertaken to find how structures produced with the fs system differed from those produced with ns systems. This first of these was to fire multiple laser pulses at a single spot on the target surface for various periods of time. Effectively, this allowed an investigation of the development of structures in a single spot over time. This was done by focusing the raw beam to a $\sim 90\mu\text{m}$ diameter spot, using a 50 mm focal length singlet lens, at a fluence of $\sim 9.5\text{Jcm}^{-2}$. The laser was then turned on and allowed to dwell for 0.047, 0.096 and 0.141 seconds. It being difficult to fully control or calculate the speed of the laser shutter, these values were chosen so that approximately, 50, 100 and 150 pulses would be delivered. Typical results of this experiment can be seen in Figure 4.24.

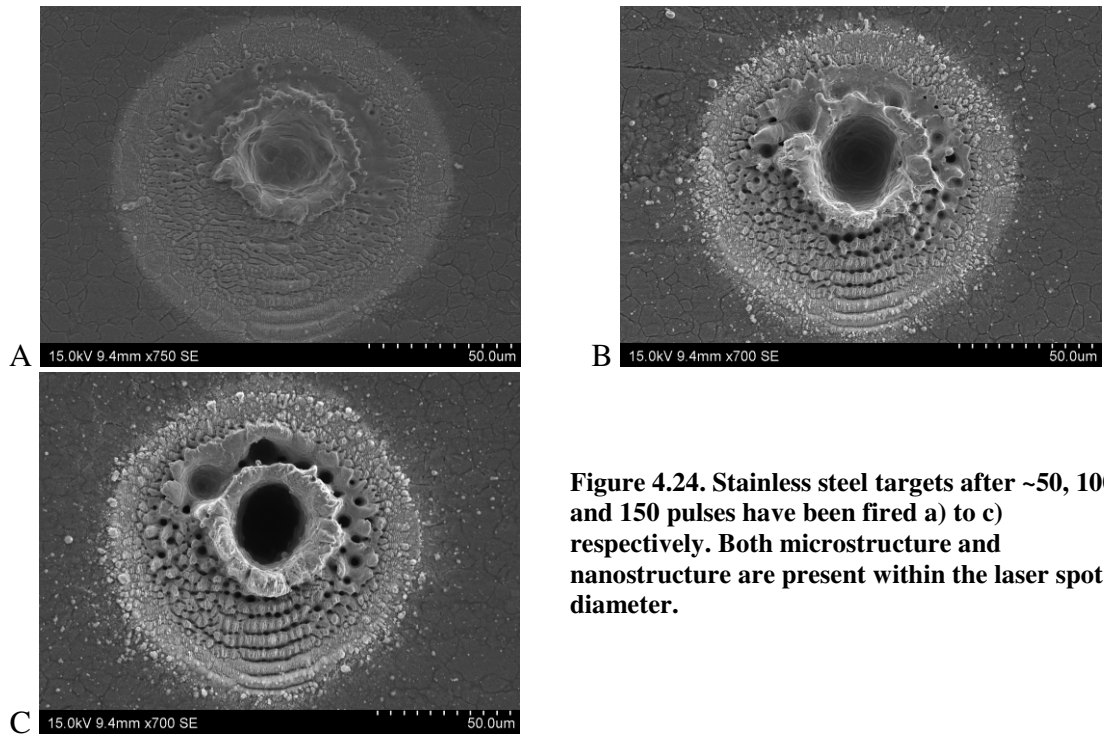


Figure 4.24. Stainless steel targets after ~50, 100 and 150 pulses have been fired a) to c) respectively. Both microstructure and nanostructure are present within the laser spot diameter.

In the next section it will be seen that structure can be formed after single pulse ablation of a surface. These images show the development of a surface as larger numbers of pulses are fired at a fluence that is well above the threshold needed. The most obvious difference between these results and those which would be found with ns laser systems is the amount of structure which is present within the machined laser spot. Where a hole approximately the size of the laser spot would be present in ns processing, we find that regular structure is formed. Even though some aberration is present in the optical arrangement the structures present have a ring geometry that can be explained by diffraction in an Airy pattern [32] which is diffraction by a circular aperture. In this case, the circular aperture occurs before the laser interacts with the target. The aperture associated with the focusing lens is the most likely. It can also be seen that although there is a small amount of melt flow present, the majority of the structures were formed by an ablative process. This would mean that any structures produced by this method should vary greatly in comparison to those produced by ns lasers.

The second experiment, working with the same laser parameters was used to investigate the effect of laser scan speed. The laser was scanned over the target surface at 1, 2, 3 and 4mm/s and in each case four passes were made. A hatch distance equal to that of the laser spot size, 90 μ m was used.

The structures which resulted from this experiment can be seen in Figure 4.25 to Figure 4.28. Each figure, shows how the scan speed affects that structure formed. The Figure 4.25 is after one pass of the laser over the surface. Figure 4.28 shows the target surface after four passes. If we first discuss the effect of scanning speed, it is understandable that a lower scanning speed will allow more processing to take place. This is because a larger number of pulses interact with the target surface in a given period of time. For each pass, the number of pulses fired per spot in relation to the scanning speed is given in Table 4-4.

Scanning Speed / mm/s	Pulses per spot
1	90
2	45
3	30
4	22.5

Table 4-4. Relationship between scanning speed and pulse number for a 90 μ m laser spot.

The surface structures which are produced after one laser processing pass at the four speeds mentioned can be seen in Figure 4.25. These images show that as the processing speed increases, thus lowering the number of applied pulses, less removal of surface material takes place. This is an understandable consequence. However these images also show that the formation of surface microstructures depends on multiple pulses being applied to the surface. The linear nature of the structures can be attributed to the movement of the target during processing. This is especially noticeable in Figure 4.25a

which has received the largest number of pulses. As indicated by Figure 4.24c, the deeper central ablated region has been extruded to form a channel.

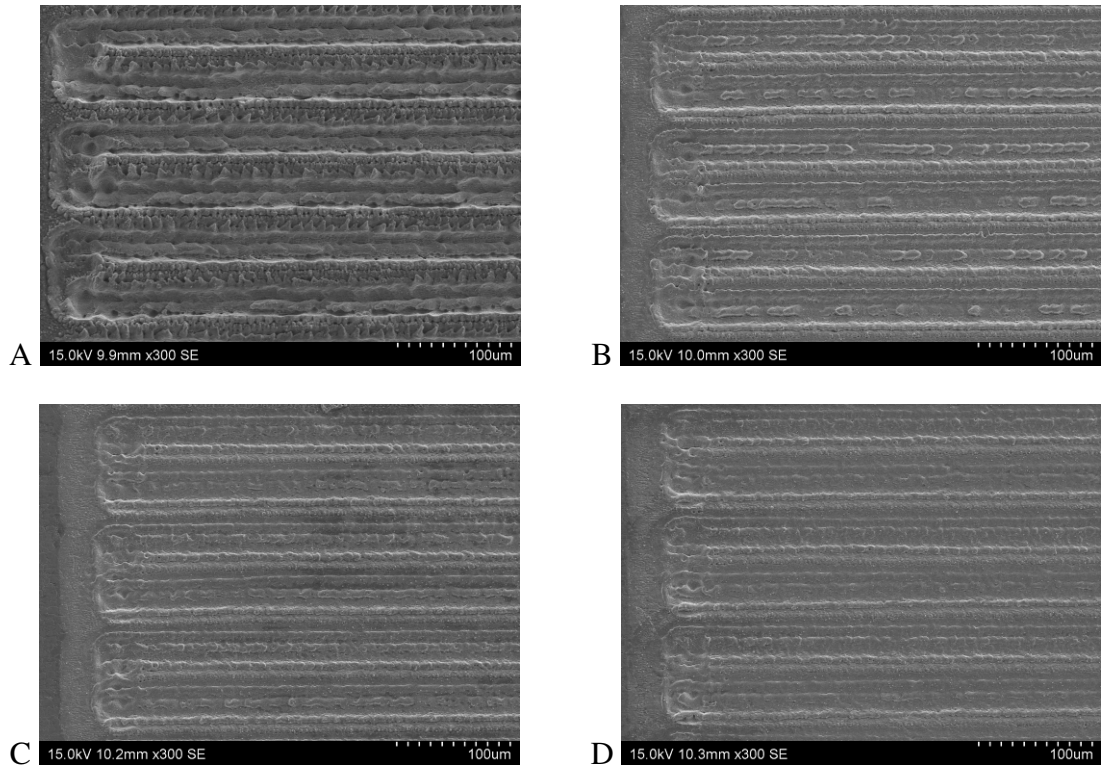


Figure 4.25. Structures produced after 1 pass at scan speeds of 1,2,3 and 4 mm/s. These can be seen in a) to d) respectively.

If a comparison is drawn between these structures and those due to laser processing in a similar manner using ns laser pulses there are two significant differences. The first of these is a lack of re-solidified molten material. As mentioned previously, the ultrashort pulses from femtosecond lasers do not allow time for energy to flow by thermal conduction to the surrounding material. This drastically reduces the volume of material which is molten and available to flow about the surface. Secondly, although microstructures are immediately obvious features, sub-wavelength structures also cover the majority of the surface. These features will be discussed separately in the next section.

Returning to the microstructure observed, the images in the next three figures (Figure 4.26, Figure 4.27 and Figure 4.28) show the evolution of surfaces as increasing numbers of passes are made over surfaces such as those seen in Figure 4.25.

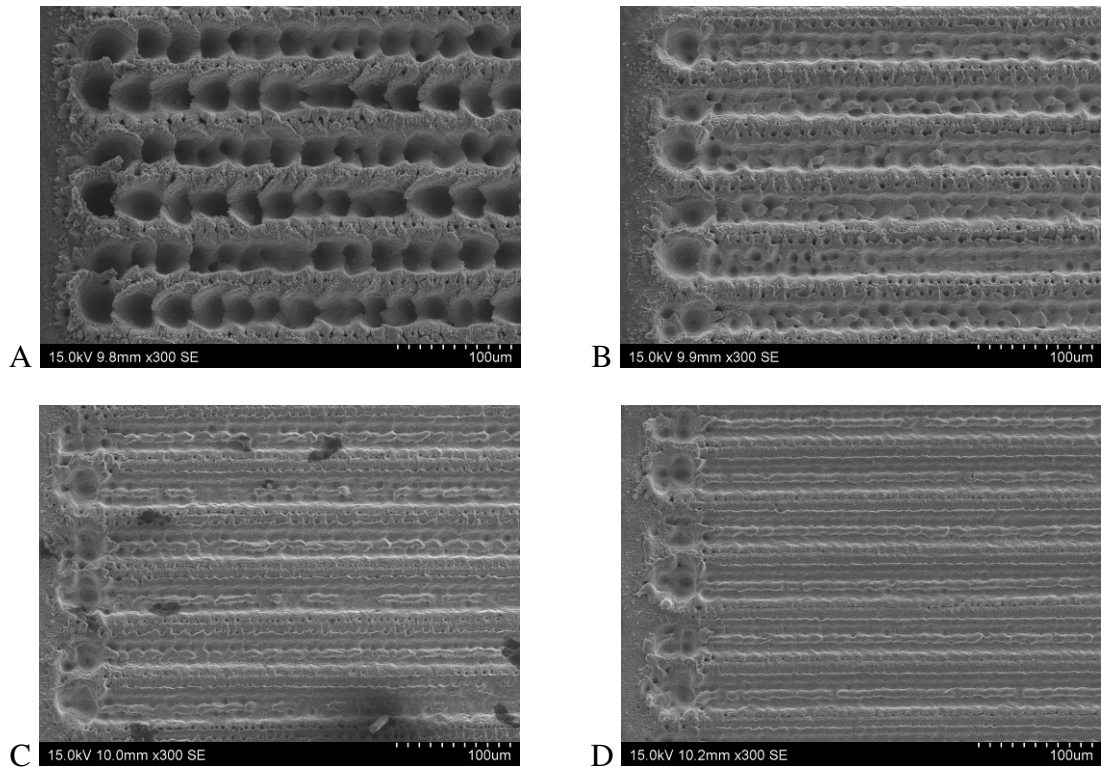


Figure 4.26. Structures produced after 2 passes at scan speeds of 1,2,3 and 4 mm/s. These can be seen in a) to d) respectively.

Although there are two variables to consider with these four sets of images (Figure 4.25 to Figure 4.28) it is possible to see trends appearing in the structures formed. It is thought that features present in Figure 4.25a and Figure 4.28d are extremely similar. This is explained by the condition that the same number of pulses have been applied to each surface. The difference in features at the beginning of the laser path can be explained by the dwelling of the laser beam as the mechanical stage decelerates and moves to the next scan line, causing larger numbers of pulses to begin drilling holes in the surface. As is the case in ns processing, multiple passes tend to accentuate the features which are formed during the first pass. This progression can be seen in the

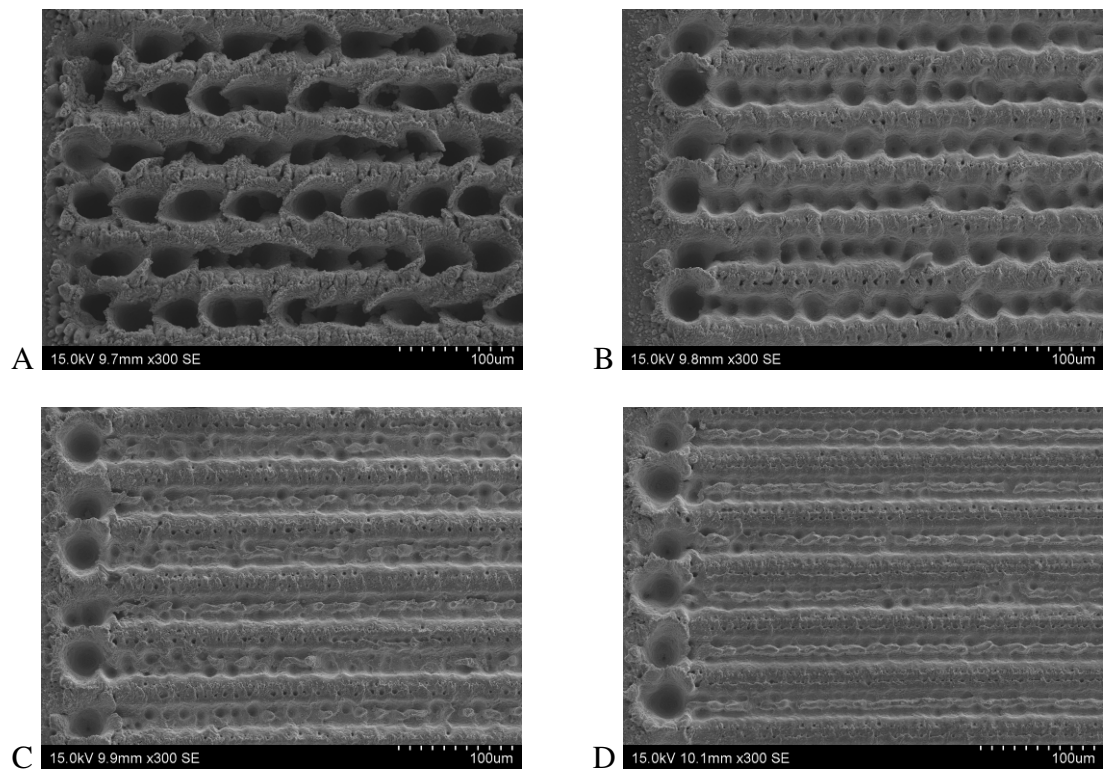


Figure 4.27. Structures produced after 3 passes at scan speeds of 1,2,3 and 4 mm/s. These can be seen in a) to d) respectively.

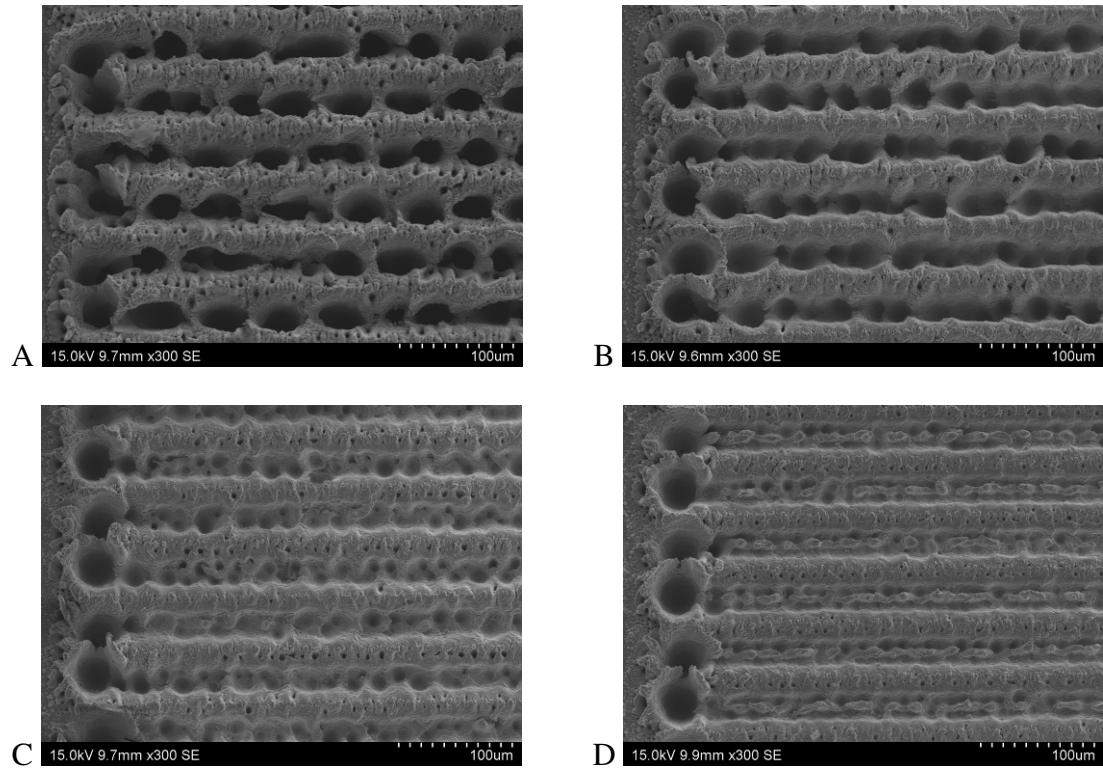


Figure 4.28. Structures produced after 4 passes at scan speeds of 1,2,3 and 4 mm/s. These can be seen in a) to d) respectively.

above figures. It can be seen from inspection that structures produced at higher scanning speeds have a finer microstructure.

4.5.3 Production of Sub-Wavelength Structures using Femtosecond Lasers

Further investigations into the formation of sub-wavelength structures revealed that it is possible to use the well known bell shape intensity distribution of a Gaussian beam to our advantage. A known threshold of both damage and ablation means that as overall power is reduced, the effective area of the laser spot decreases. This means that at fluences between the incubation and ablation threshold it is possible to treat the laser beam as a flat top because only the central region of the beam is of a high enough intensity to modify the surface. This effect can be seen in Figure 4.29.

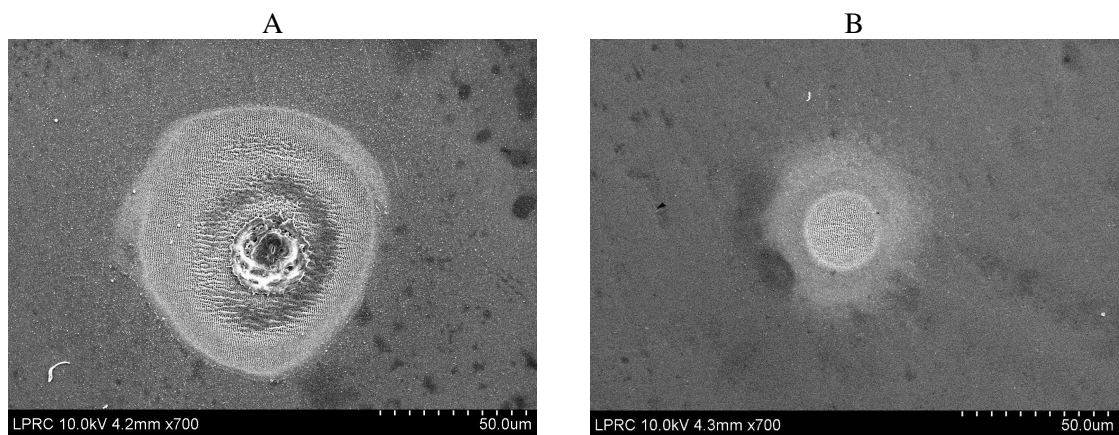


Figure 4.29 The effect of femtosecond laser processing after ten pulses at fluences of 4.06Jcm^{-2} (a) and 0.09Jcm^{-2} (b)

Here the processing of the two sites differed only in the fluence being used. Figure 4.29a, processed with a fluence of $\sim 4\text{Jcm}^{-2}$, shows the three different types of damage which occur. Beginning at the centre of the damaged area it can be seen that ablation takes place, moving outwards, the microstructures which have been discussed previously are beginning to form. As the periphery of the damaged area is reached, the intensity of laser light will be much lower. At these low powers, the dominant features are sub-wavelength laser induced periodic surface structures (LIPSS). Figure 4.29b

shows an area treated with ten laser pulses were at a fluence of 0.09 Jcm^{-2} , just over the incubation threshold. This area is shown at higher magnification in Figure 4.30.

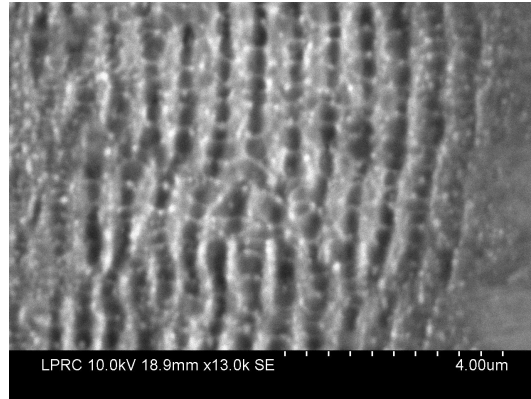


Figure 4.30 Example of laser induced periodic surface structures (LIPSS) produced using an 800nm femtosecond laser at an average power of 8mW and twenty applied pulses.

White light interferometry measurements of the surface shown in Figure 4.29b can be seen in Figure 4.31. A crater with a maximum depth of 200nm is produced after 10 pulses, with wavelength 800nm. A closer look at this area using scanning electron microscopy revealed that the damaged area is covered in LIPSS with a mean period of $589 \pm 42 \text{ nm}$. As can be seen by Figure 4.32, the mean period of LIPSS occurring at 800nm can be considered independent of the laser fluence used, suggesting that it is indeed caused by interference effects as suggested.

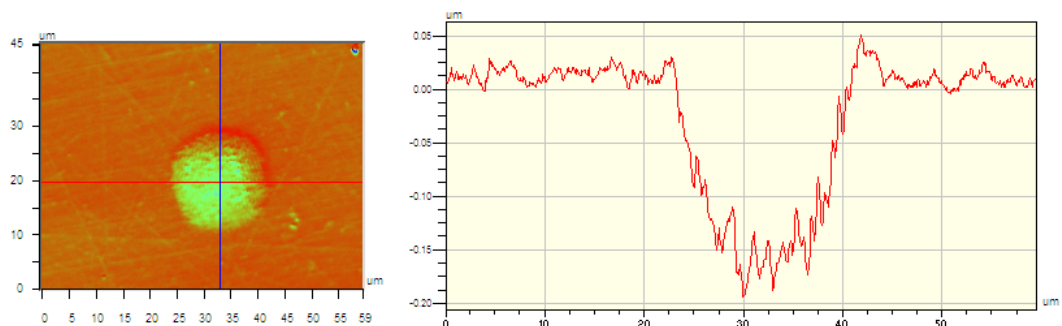


Figure 4.31 Profile of ablation crater obtained using white light interferometry

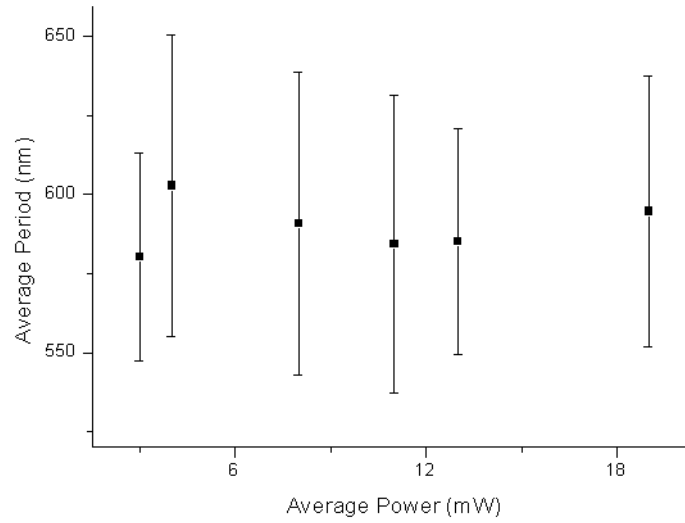


Figure 4.32. Mean period of LIPSS generated using 800nm femtosecond light.

With the aid of a BBO crystal, allowing 800nm radiation to be frequency doubled the same experiment was performed at 400nm. At this wavelength, due to increased photon energy, a lower fluence is required. In this case it was found that a fluence of only 0.13Jcm^{-2} was required. It was found that the average period of the LIPSS formed by 400nm light was 282 ± 21 nm.

4.5.4 Sub-wavelength features over large areas.

At this point, all LIPSS areas had been produced while the target was stationary. Translating the target perpendicular to the polarisation direction of the laser beam allows LIPSS structures, formed in a single spot, to be extruded into more linear features.

Figure 4.33 shows an example of the types of structures which were formed using 100fs pulses at a wavelength of 800nm and a processing speed of 1mm/s. A fluence of

0.022Jcm^{-2} was used. The area that can be seen in the micrograph shows approximately the area of a single laser spot. As can be seen, the features which are present have a regular structure and a period of $\sim 610\text{nm}$. This period is in keeping with the period found during stationary processing.

Working at the shorter, 400nm , wavelength in the same manner allowed the structures seen in Figure 4.34 to be produced. Although these structures are formed by the same mechanism of those seen in Figure 4.33 the period is much shorter, $\sim 295\text{nm}$. This is due to the change of laser wavelength.

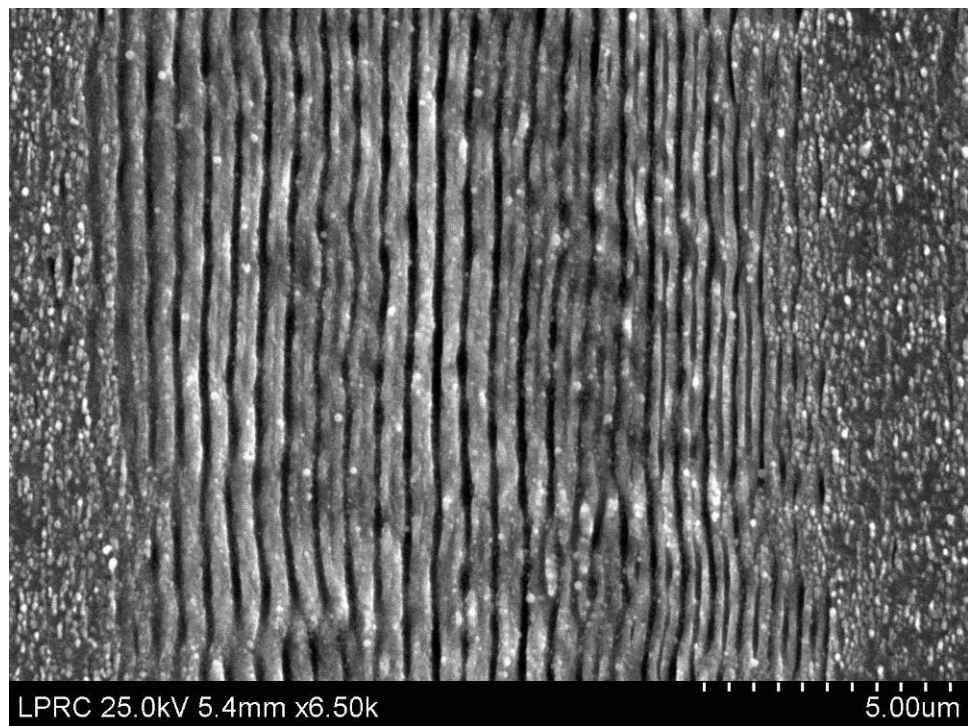


Figure 4.33 Laser induced periodic surface structures formed by translating a stainless steel sample with a speed of 1mm/s at a fluence of 0.022Jcm^{-2}

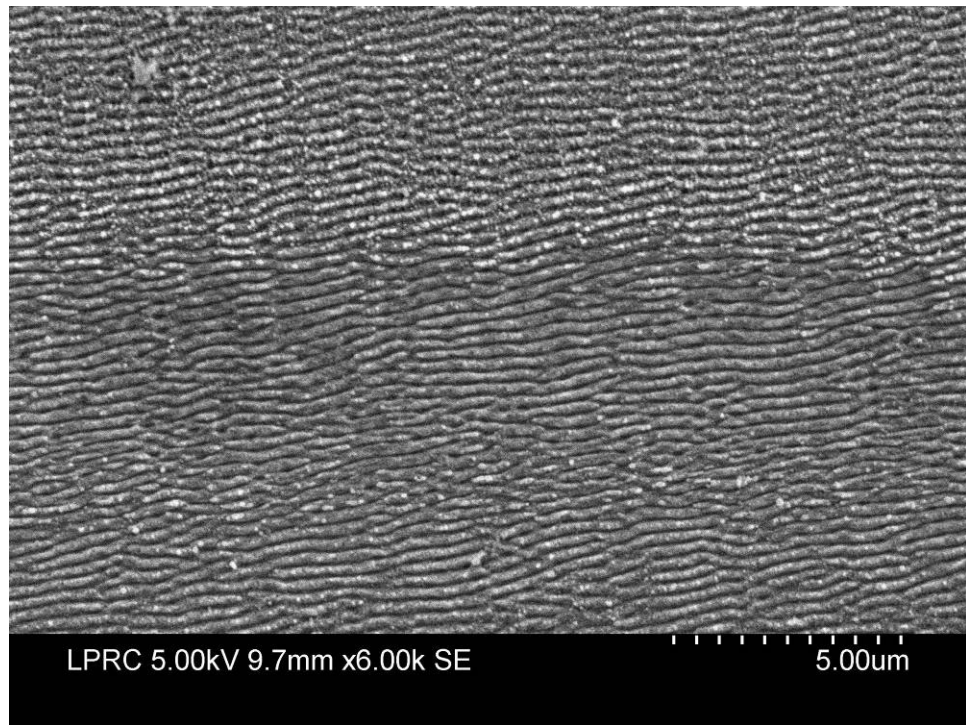


Figure 4.34 Laser induced periodic surface structures formed at 1mm/s and a fluence of 0.001Jcm^{-2} . Structure period is found to be $\sim 295\text{nm}$

It was found that varying the scanning speed and number of passes had very little effect on the arrangement of structure formation.

To develop the types of structure that can be formed using this method, it was decided to investigate the formation of LIPSS by rotating the sample by 90° between processes. This has the effect of rotating the polarisation of the incident laser beam relative to the sample. This experiment was performed at a wavelength of 800 nm using the same parameters as those used to form the structure in Figure 4.33. These results can be seen in Figure 4.35.

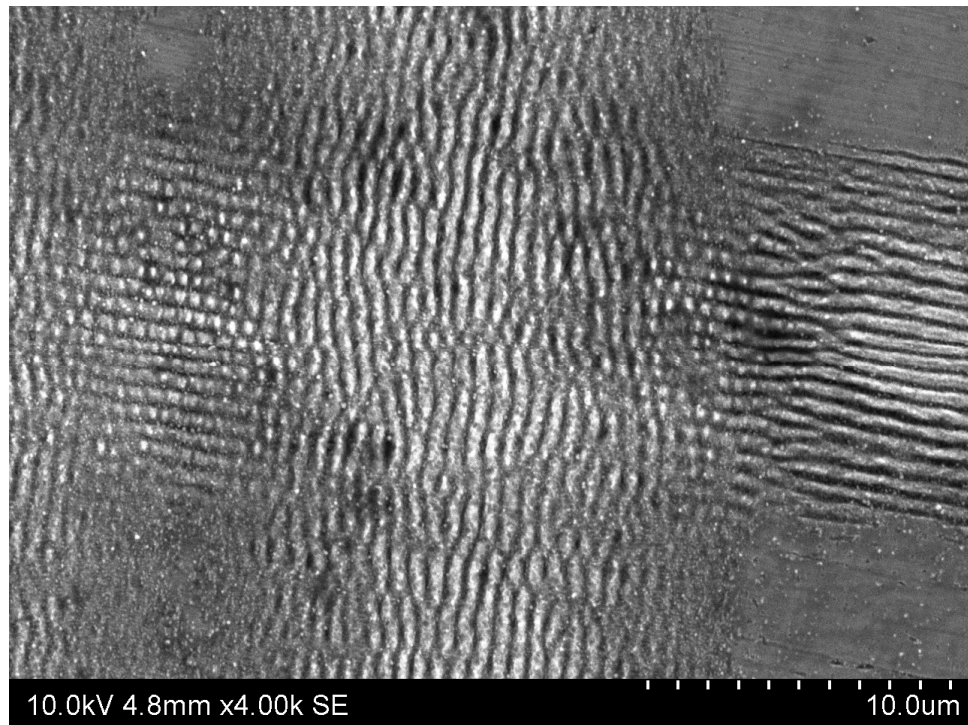


Figure 4.35. Laser induced periodic surface structures formed by the superposition of two processing passes. Importantly, during the second pass, initial structures are not destroyed at the edges of the beam path.

It is noted from this image that the LIPSS formed in a horizontal direction on the image were formed during the first processing pass. During the second pass the structures running in the vertical direction were formed. As is plainly obvious, the second processing pass destroyed the LIPSS which were formed initially, only at the edge of the beam path is there a superposition of structures. Here two sets of periodic ripples combine to produce sub-wavelength bumps with a spacing of approximately 600nm. This would suggest that, given the Gaussian intensity distribution of the processing beam that a lower intensity is required to form these bumps, that LIPSS formed during the first processing pass enhance the absorption of incident pulses during the second pass.

4.6 Surface Structure Formation Mechanisms

In this chapter it has been shown that the types of surface structure which can be formed on metals, specifically stainless steel, using lasers are diverse. To better understand the mechanics of microstructure formation, it is important to know the temperature changes involved during laser processing. This is done with the assistance of a one dimensional heat flow model. This model allows a theoretical peak temperature to be obtained and gives some indication of the timescales involved in heating and cooling.

4.6.1 One dimensional heat flow model

Assuming that the heat flows in only one direction and there is no convection or heat generation the basic heat equation becomes:

$$\frac{\partial^2 T}{\partial z^2} = \frac{1}{D} \frac{\partial T}{\partial t} \quad 4.6$$

Where T is the temperature, z is the depth, t is the time and D is the thermal diffusivity.

If it is assumed that there is a constant extended surface heat input and constant thermal properties, with no radiant heat loss. Then the solution taken from Steen [11] is:

$$T(z,t) = \frac{2I}{k} \left(\sqrt{Dt} \cdot \text{ierfc} \left(\frac{z}{2\sqrt{Dt}} \right) \right) \quad 4.7$$

Where I is the intensity and k is the thermal conductivity. The ierfc function is called the “integral of complimentary error function” and is derived from a mathematical

polynomial [95]. However taking into account any losses due to reflectivity, R of the metal surface equation 4.8 becomes:

$$T(z,t) = \frac{2I(1-R)}{k} \left(\sqrt{Dt} \cdot \text{ierfc} \left(\frac{z}{2\sqrt{Dt}} \right) \right) \quad 4.8$$

To include cooling of the material after the laser pulse, the integration in Equation 4.8 is extended beyond the pulse duration. Consider the uniform surface like previously then the material will cool according to the relationship [11].

$$T(z,t) = \frac{2I(1-R)}{k} \left(\sqrt{Dt} \cdot \text{ierfc} \left(\frac{z}{2\sqrt{Dt}} \right) - \sqrt{D(t-\tau)} \cdot \text{ierfc} \left(\frac{z}{2\sqrt{D(t-\tau)}} \right) \right) \quad 4.9$$

Using these equations a basic understanding of the laser interaction with stainless steel can be formed. Using the values shown in Table 4-5 as input variables, the plots of temperature vs. time after the firing of a laser pulse can be seen in Figure 2.1. The values of fluence and pulse duration are those used in previously discussed experiments.

	532nm	1064nm
Thermal Conductivity (W/mK)	13.8	13.8
Thermal Diffusivity (m²/s)	0.4x10 ⁻⁵	0.4x10 ⁻⁵
Fluence (J/cm²)	2.63	4.32
Pulse Duration (ns)	7	7
% Reflectivity	38	46

Table 4-5. Input variables used in the calculation of surface temperature change using a one dimensional heat flow model [96]

Values at 532nm relate to topographical structures shown in Section 4.2.2 and values at 1064nm relate to structures discussed in Sections 4.3.3 to 4.3.5.

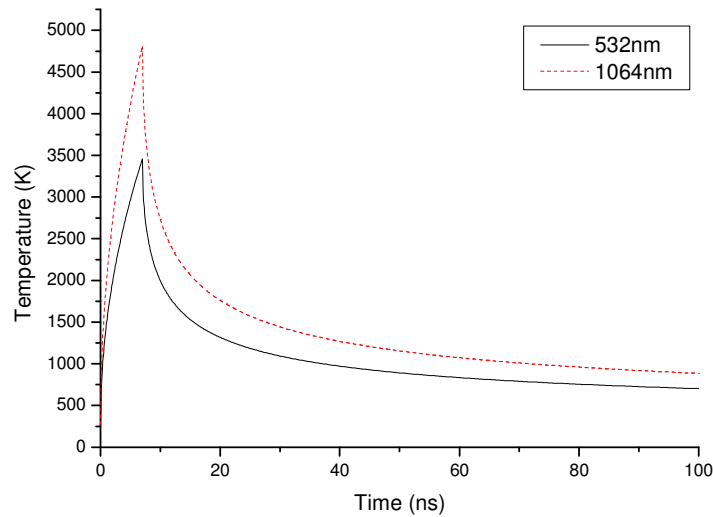


Figure 4.36. Change of surface temperature with time of stainless steel surfaces subjected to 7ns pulses of laser radiation at 532 and 1064nm

Figure 4.36 is quite revealing of the temperature changes which take place during processing and their timescales. Considering processing at 532nm, the peak temperature reached is calculated to be 3,460 K, this is over the boiling point of stainless steel. In addition to this, the surface only stays at that temperature for a short period of time, returning to a temperature below the melting point of 1783 K within 4ns of the end of the laser pulse. With a repetition rate of 30kHz, the time between laser pulses is three orders of magnitude longer than this period of heating and cooling. Now considering a wavelength of 1064nm the peak temperature reached is calculated to be 4,833 K and a further 12ns are taken for the surface temperature to return below the melting point. This is a reasonable value as a higher fluence is used.

Both of these theoretical results fit well with observed structures and formation theories. At both wavelengths, it is found that the temperature peaks above the boiling point of the metal for a short time. During this time, due to the irradiance profile of the beam used, small amounts of molten materials will flow towards the cooler edges of the beam path. At a repetition rate of 30kHz, the cumulative effects of these pulses will begin to form regular structures.

Experimental observations of processing at 1064nm confirm this. It has been shown that higher fluences increase the peak temperature reached and that the time taken for a surface to re-solidify is almost three times longer. Higher temperatures mean more material on the surface will be molten and the extended period of time the material is molten accounts for the more abundant melt flow that occurs while processing at 1064nm.

4.7 Conclusions

It has been shown that the topographical structures which can be produced by self assembled methods of laser processing are diverse. The formation of microstructures using nanosecond lasers has been shown to be dependant on various factors. Laser fluence is possibly the most important of these. In this case, rather than using a laser for the complete removal of material a novel process has been shown that relies on the partial removal of the metal surface and more importantly the movement of molten. A one dimensional heat flow model has shown that fluences slightly above the threshold fluence of the metal allow the temperature of stainless steel surfaces are taken to

roughly 500 - 1000 K above the boiling point of the material. For brief periods of time (5 – 20ns) after the laser pulse has stopped, the surface of the material is still molten. During this time instabilities in the molten material allow the movement of material to the cooler edges of the beam path. This movement is fuelled by the expansion of ablation products at the high intensity central region of the laser beam. Owing to the high repetition rate of the laser, the formation of self assembled micro scale structures occurs over a period of time where large numbers of pulses are applied, each pulse contributing to the formation of structures which have approximately the same height as their period.

It has also been shown that the distance between scanning paths has a great affect on structure formation. When there is a large overlap between consecutive scans, the structures shown in section 4.2 are typical. There is very little control over the exact positioning of these structures. In section 4.3 the advantages of processing with a larger hatch distance become apparent. Obviously, increasing the distance between scan lines means that the processing time for a set area will decrease. Additionally, using a hatch distance above 50% of the laser spot size allows topography with a period equal to the spot size to be formed. Further developments of this technique have shown that scanning with two interlaced patterns orientated perpendicular to each other allows even higher control of the feature size and position.

Previous to this work the orientation of self assembled microstructures towards the incident angle of a laser beam other than normal to the surface had only been mentioned briefly in literature [17]. It has been shown in section 4.3.5 that there is a very good

correlation between the angle of surface structure formation and the incident beam angle.

Experiments using femtosecond lasers have shown this technology as particularly useful for the production of sub-wavelength structures. Owing to the high intensity and ultrashort pulse duration of femtosecond laser systems it has been shown that it is relatively simple to produce surface structures of approximately 600 and 280 nm with 800 and 400nm laser light. Development of this technique has been shown to allow the coverage of large areas with these laser induced periodic surface structures. This is achieved by translating the target surface in a direction perpendicular to the polarisation of the laser.

5 MODIFICATION OF WETTABILITY

In Chapter 4, topographies produced by laser modification of stainless steel surfaces were discussed. This chapter is intended to illustrate one of the applications of such surfaces, namely their effect on the contact angle of water droplets deposited onto the surfaces.

In recent times, there has been an increased interest in the fabrication of surfaces with very high contact angles. These so called super-hydrophobic surfaces have a contact angle higher than 150° . A natural example of a super-hydrophobic surface is the leaf of the lotus plant [4] commonly found in many parts of the world. The ultimate goal of this work is to produce super-hydrophobic surfaces on metals. Initially, stainless steel is the target substrate, however in some cases, other metals including copper and titanium have been studied. The effects of several laser variables were of interest during the course of the experiments which are described in Chapter 4. The same variables are of interest now, however it is the effect on the contact angle rather than the resultant topography of the surface which is now the focus of our attention.

5.1 Contact Angles and Wettability

The wettability of a surface is a measure of how easily a liquid can spread out on a solid substrate. The wettability of a surface is usually discussed in conjunction with the contact angle of a liquid-vapour interface when it is in contact with a solid surface. When a liquid droplet (usually water) is formed on a surface, it is natural for the liquid to adopt a form that will minimise the interfacial energy at the points where it contacts both the surface and the surrounding atmosphere. This effect is especially important in

an environment of air. In this case, the droplet will form a bead on the surface, with the edges of the bead making a contact angle, θ , with the surface.

Essentially, there are three regimes into which a droplet resting on a solid surface can fall. These regimes (Figure 5.1) are dictated by the contact angle which the droplet forms with the surface and are a measure of the surfaces wettability.

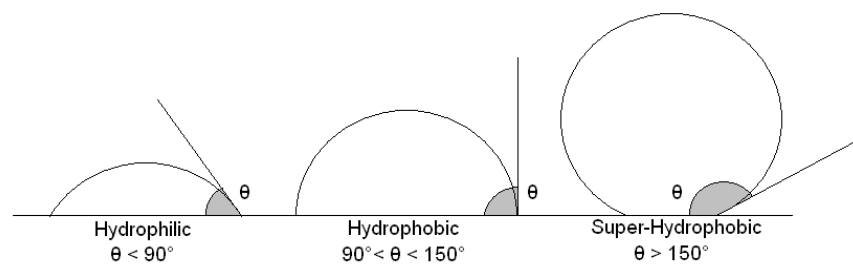


Figure 5.1. Three regimes of contact angles when a droplet is formed on a surface.

Beginning with low contact angles (high wettability), the first type of surface is a hydrophilic one. In these cases the contact angle is below 90° . Increasing the contact angle (decreasing the wettability), leads to a hydrophobic state. Here the contact angle is above 90° . Decreasing the wettability further brings us to the most interesting state, the case of a super-hydrophobic surface. Here the contact angle is greater than 150° . The reason for a heightened interest in super-hydrophobic surfaces is the bead shape which the droplet adopts. This is done to minimize energy, but it has other implications such as increasing the mobility of the droplet over the surface and allowing surface cleaning to occur as the droplet moves around.

The first major investigations into the concept of wettability were conducted by Thomas Young, as early as 1805 [97]. The resultant equation from his work can be seen in (5.1).

$$\cos \theta_y^s = \frac{\gamma_{SV} - \gamma_{SL}}{\gamma_{LV}} \quad 5.1$$

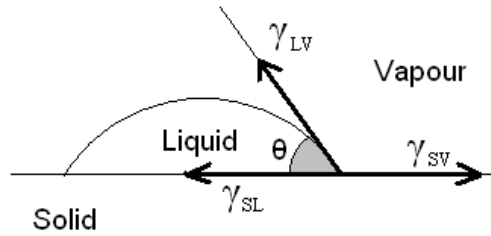


Figure 5.2. Interfacial forces acting on a liquid droplet at rest on a surface.

Where θ_y^s is the Young's angle and γ is the interfacial tension at the solid-vapour, solid-liquid and liquid-vapour interfaces (Figure 5.2). The contact angle that a liquid droplet makes with a flat surface is dictated by the free energy of the surface. As a general rule when water is involved, the lower the surface energy, the higher the contact angle. This is all due to the fact a liquid droplet will assume the form which requires the lowest amount of energy. Although this work is the foundation of modern theory, the resultant contact angles are calculated for a chemically homogeneous and perfectly smooth surface. While further work has been done on the contact angle of smooth, homogeneous surfaces [98-100], for most applications it is important to take the roughness and varying chemical composition of the surface into account.

5.1.1 Wetting on rough surfaces

In actuality, the complications of roughness and surface composition were tackled independently of one another. It was Wenzel, who studied the effect of the surface roughness on the apparent contact angle [101]. The result of these investigations gave the relationship:

$$\cos\theta_w = r\cos\theta_Y^S \quad 5.2$$

Where θ_w is the Wenzel contact angle and r is the surface roughness, defined as the ratio of the true surface area to the horizontal projection of the surface area. The implications of (5.2) are that when the value of $r = 1$ (smooth surface), a return is made to the Young's angle. However when $r > 1$ two different types of behavior become apparent. In the first case, if $\theta_Y^S < 90^\circ$ (hydrophilic surface) then $\theta_w < \theta_Y^S$ since $r > 1$. Secondly, if $\theta_Y^S > 90^\circ$ it will be the case that $\theta_w > \theta_Y^S$. The resultant property of surface roughness, in terms of its effect on contact angle, is that the underlying wetting properties of the surface are magnified by the roughening of the surface.

During a closer inspection of Wenzels relationship for the case of a rough hydrophobic surface, it soon becomes clear that a droplet deposited onto a rough surface may not be able to follow all of the contours of that surface. In this case some air pockets will be trapped underneath the droplet, as can be seen schematically in Figure 5.3. This is not in keeping with the assumptions made in the derivation of Wenzels theory. However, the effect of a heterogeneous surface on water contact angle was studied elsewhere.

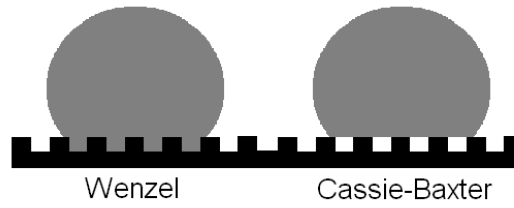


Figure 5.3. Water droplet at rest under the assumptions of Wenzel, left and Cassie and Baxter, right.

The problem of a heterogeneous surface was tackled by Cassie and Baxter in the hope of improving the water repellency of textiles [102]. The basis for their model was when a surface is chemically heterogeneous. In this model, it was assumed that a surface was made of two species, each having differing contact angles, θ_1 and θ_2 , and having fractional surface areas f_1 and f_2 . Where $f_1 + f_2 = 1$. When the interfacial energy is minimized and the Young's relation is applied, this leads to the Cassie-Baxter equation:

$$\cos\theta_{CB} = f_1\cos\theta_1 + f_2\cos\theta_2 \quad 5.3$$

Where θ_{CB} is the Cassie-Baxter contact angle.

Although (5.3) can be used in any situation, there is a special case for this equation when a droplet is placed onto a rough surface in an air environment. In this case, the contact angle between the air and the water is 180 deg. This means that (5.3) reduced to:

$$\cos\theta_{CB} = f\cos\theta_Y + f - 1 \quad 5.4$$

As we have already seen, there are two main factors which contribute to the contact angle assumed by a droplet deposited onto a solid surface. The first of these is chemical homogeneity of the surface. In the case of a planar and chemically homogeneous surface, the Young's relationship applies. If the surface becomes chemically heterogeneous but remains planar, or air bubbles are trapped below the droplet, the Cassie-Baxter relationship can be used. The second contributing factor is the roughness of the surface. In this case, the Wenzel relationship applies.

Not surprisingly, since the work of Wenzel and Cassie and Baxter, there has been a large amount of work carried out to further understand the wetting of rough surfaces. Although the Wenzel and Cassie-Baxter models can both explain an increase in the contact angle of a surface, there are conditions under which the two theories do not agree. A discussion of this problem by Patankar *et al* [103] gives a clear appraisal of the different predictions of Wenzel and Cassie Baxter theories. These predictions can be seen in Figure 5.4.

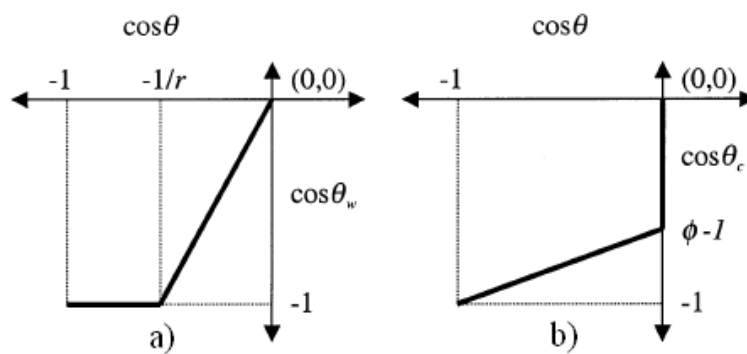


Figure 5.4. Comparison of contact angle values from the theoretical work of Wenzel (a) and Cassie-Baxter Theories (b)

From Figure 5.4 it can be seen that there are only three points on these competing plots where the theories agree. Wenzel's theory, as depicted in Figure 5.4a tells us that the equilibrium contact angle on a rough surface will be an amplification of the contact angle of the same liquid on a flat surface, caused by the roughness ratio, r . Whereas Cassie and Baxter's theory tells us that during composite wetting, if more of the area underneath a droplet exposed to air than surface material then the contact angle will increase significantly. These discrepancies have been investigated independently and there is experimental evidence that both theories are correct under the correct conditions. Bico *et al* reported good agreement between the theory of Cassie-Baxter type wetting and their experiments [9]. In this case a number of different surfaces – spikes, holes and stripes – were fabricated from a silicon wafer substrate with a monolayer of fluorosilane. This was done in order to induce Cassie-Baxter type wetting and contact angles of 170° were observed. It is interesting to note that if a droplet with a contact angle of 170° was pressed, it made a transition from Cassie-Baxter wetting to Wenzel wetting and its contact angle decreased to 130° , as predicted by theory. The transition of droplets sitting on a rough surface from Cassie-Baxter to Wenzel wetting has also been studied by Liu *et al* [104]. The comparison of Wenzel theory and experimental data was performed by Onda *et al* [105]. Their experiments found that Wenzel type wetting on fractal surfaces made from alkylketene dimer resulted in contact angles of up to 174° . In addition to this, it was found that the experimental results fitted with Wenzel's theory. From this collection of work, it has been proposed that Wenzel's formula be used when the equilibrium contact angle is in the hydrophilic ($\theta < 90^\circ$) region and Cassie and Baxter's formula be used in the hydrophobic ($\theta > 90^\circ$).

5.1.2 Contact Angle Hysteresis

Further development of this idea brings us to the concept of contact angle hysteresis. Although the sessile drop method is a good estimate of the overall wettability of a surface, it is not a true representation of how a moving droplet would behave. In this case the concept of hysteresis must be used.

When a droplet is moving, it is usually because the surface is not flat. In Figure 5.5 it can be seen that although the liquid droplet is in contact with the same surface at the upper and lower sides of the droplet, the contact angle is different. On the lower side of the droplet, the advancing contact angle, θ_A , is higher than that of the receding contact angle, θ_R , on the upper side of the droplet. Due to the nature of the droplet, there will be an infinite number of contact angles at the different points along the liquid-solid interface. For this reason, the contact angle hysteresis, $\Delta\theta$, is given as:

$$\Delta\theta = \theta_A - \theta_R \quad 5.5$$

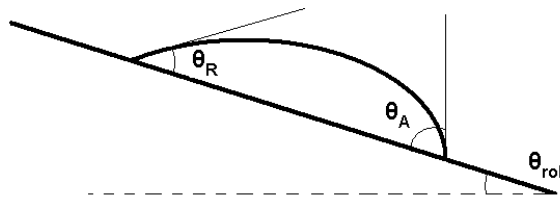


Figure 5.5. Advancing and receding contact angles of a liquid droplet on an inclined surface.

The hysteresis and change of contact angle as a function of the surface roughness was investigated by Johnson and Dettre [106]. The results of their work on the contact angle hysteresis on a roughened wax substrate can be seen in Figure 5.6

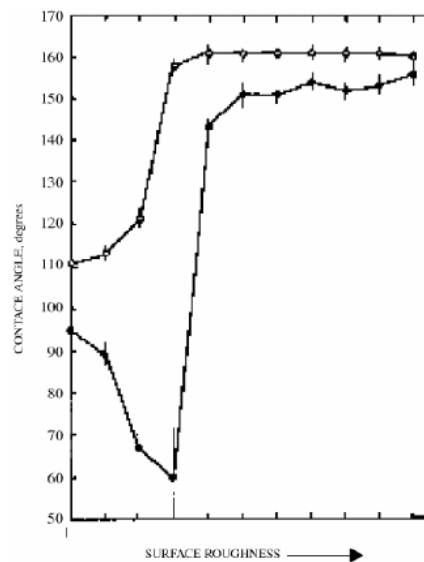


Figure 5.6. Advancing and receding contact angles on rough surfaces [106].

As can be seen in Figure 5.6, as the roughness increases, initially there is a dramatic rise in the contact angle hysteresis. As the roughness increases further, the contact angle hysteresis begins to decrease until an approximate equilibrium is reached. This means that the effect of increasing roughness on a hydrophobic surface is that not only is the contact angle increased, as predicted by Wenzel and Cassie-Baxter theory, but the hysteresis also decreases. This makes the surface more robust if it is desired to be super-hydrophobic.

5.2 The Lotus Effect

The self cleaning properties of most plant leaves are obvious and have probably developed as an evolutionary response to any number of factors such as disease or simply collection of sunlight for photosynthesis. The majority of leaves have a certain degree of hydrophobicity. This is usually due to the waxy or smooth surfaced of their leaves or petals. There are however, a number of plants whose leaves have super-hydrophobic surfaces [107]. The lotus plant, *Nelumbo Nucifera*, is one of these such specimens. The term ‘lotus effect’ was first coined by Barthlott and Neinhuis [4] during their work on the self cleaning properties of various plant leaves. They found that the reason for the high water contact angle ($\sim 160^\circ$) on the lotus leaf was not due to a smooth surface, but actually a rough one.

5.2.1 Physical Basis of the Lotus Effect

As can be seen from Wenzel (eqn 5.2), the roughness of a surface amplifies the underlying wetting properties of the surface. It can be seen from Figure 5.7a that the surface of a lotus leaf is very rough. There are protrusions from the average surface, on which a water droplet rests.

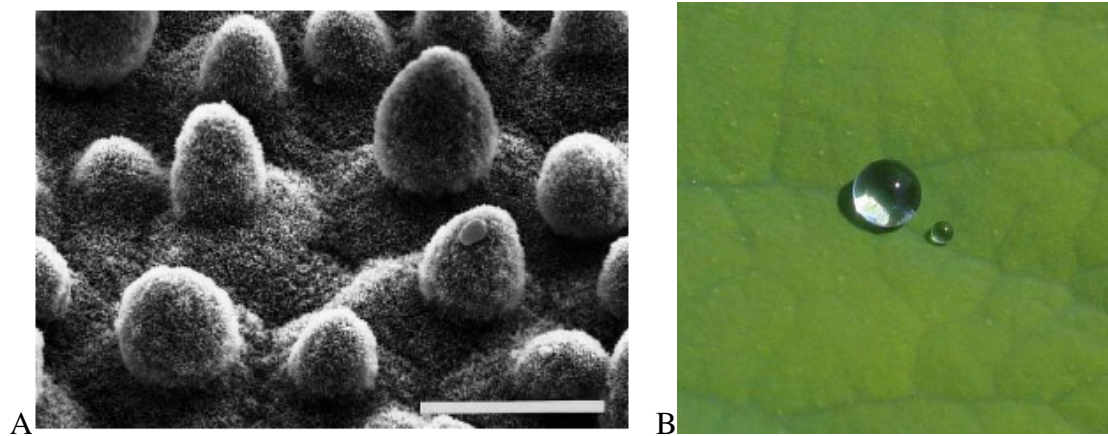


Figure 5.7 a) SEM image of the surface structure of a lotus leaf (right). b) Photograph of liquid droplets at rest on a lotus leaf (left)[108].

It was found during the studies of Barthlott and Neinhuis [4, 107] that lotus leaves have one of the highest contact angles 160.4° [4]. It is believed that this is because of the double scale structure that can be observed on the surface of a lotus leaf. In Figure 5.7a it can be seen that in addition to the relatively large micron scale features, there is a frosting of some white material. In actual fact the frost is made from wax crystals. These epicuticular wax crystalloids are the main cause of water repellency and are reported to have a length between 1 and $5\text{ }\mu\text{m}$ and a diameter in the nanometer range.

5.2.2 How and Why the Lotus Leaf is Self Cleaning

Most contaminants that are deposited on the surface of a lotus leaf are larger than the scale of the surface structure. For this reason, contaminants will rest on the peaks of the surface structures. The reason particles are removed is due to the way the droplet moves over the surface.

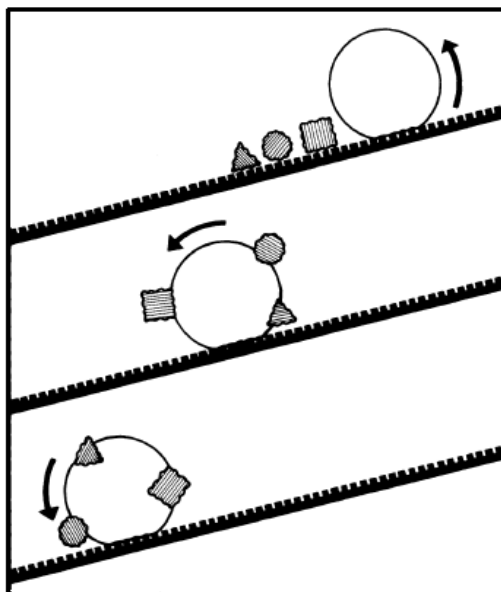


Figure 5.8. Schematic of the way in which particles are removed from super-hydrophobic surfaces by liquid droplets [4]

A high contact angle means that the droplet rolls over the surface rather than slides. As the droplet rolls, contaminants, which are usually hydrophilic, but even hydrophobic particles such as pollen, are embedded into the surface of the water droplet.

It can be seen from Figure 5.8 how contaminants are removed from a super-hydrophobic surface such as a lotus leaf. This is the beauty of a super-hydrophobic surface. Rather than the droplet sliding, as a raindrop would down a window pane, the droplet actually rolls, acting like a sticky marble and removing any debris in its path.

5.2.3 The breakdown of the lotus effect.

It has been shown [109] that the hydrophobic effects of the lotus leaf can be cancelled, if water is deposited onto the surface in the correct way. When water vapor is allowed to condense onto super-hydrophobic surfaces, such as a lotus leaf [110] or some other super-hydrophobic surface, the vapor will fill any voids between protrusions on the

surface. As the vapor begins to condense, it does so over all of the features of the surface at the same rate. Effectively, this means that a Wenzel type of wetting is induced, whereas under normal circumstances of drop formation a Cassie-Baxter type would prevail.

5.2.4 Artificial Low Wettability Surfaces.

Although initial work, such as that by Cassie and Baxter, Wenzel and Johnson and Dettre was completed around the middle of the 20th century, there was then a gap as interest in fabricating this type of surface waned. This was until the early 1990's when a large number of papers were published on the subject. Nakajima *et al* [99] produced a review of these fabrication methods and found a wide variety of methods being employed, including molding of plastics [9], plasma etching [111], chemical vapor deposition [112], and direct machining [113]. The daily use of low wettability surfaces is still in its infancy, however there are already some commercial applications and a whole range of possibilities. One of the first uses of the lotus effect was by the company LotusanTM. One of their products is a render that can be applied to most surfaces and, when dried, leaves a super-hydrophobic surface. One of the most obvious applications for this product is its use in inaccessible areas, such as the outside of high rise buildings. Here the paint could be utilised so that expensive maintenance costs would be reduced. It is also conceivable that, if a suitable process were developed, structural engineering materials such as metals could be processed to have the same surface structures and properties. This is one of the aims of this PhD.

5.3 General Experimental Methods

The variables which were considered in relation to the effect they have on the water contact angle were; the laser scanning speed and the total number of pulses applied per spot, N_T . In addition to these laser processing parameters, the change of contact angles over longer timescales has been studied.

In the case of contact angle measurements which were made to investigate the effect of scan speed, V , and the number of pulses applied, N_T , contact angle measurements of all sites of interest were taken within minutes of each other. The same is true of samples being studied over longer time periods. However, between sets of measurements the samples were kept in grip-sealed polyethylene bags at room temperature and normal atmospheric conditions. All measurements of contact angles were made with a FTA 188 Video Tensiometer using the FTA32 software supplied with the device.

5.4 The effect of Laser Scan Speed the Total Number of Pulses Applied

As can be seen from Section 4.3.1, the laser scan speed can have a great effect on the shape of the topography which is formed. It is known that the contact angle varies depending on the shape of the surface, because of the varying surface area which may be in contact with the droplet. This is not only true when Wenzel type wetting occurs, but also when Cassie-Baxter wetting occurs. Changing the shape of a surface will change how a liquid droplet rests on it and of particular importance, how much air can be trapped below it. To find the optimum speed to process a stainless steel and titanium sample to achieve the highest contact angles, the experiments in Section 4.3.1 were

repeated and contact angle measurements taken. The results of these can be seen in Figure 5.9 and Figure 5.10.

If we first consider the change of contact angle with speed on stainless steel (Figure 5.9), it can be seen that there is a general peak in the contact angle when the scan speed is 10mm/s. This is the same no matter what the total number of pulses applied is. At lower scan speeds, the contact angle decreases rapidly, however when the scan speed is above 10mm/s it is reasonable to say that increasing the number of pulses applied increases the contact angle. This is because although it is much harder to modify surface topography at high speeds, applying a larger number of pulses will increase the size of any features such as peaks or holes which have been initiated by previous sets of pulses. If we now move on to Figure 5.10, we find that the generalities which were true of stainless steel no longer apply. At lower pulse numbers (2500 and 5000 pulses) there is a peak in contact angle at approximately 5mm/s and the other features of the plot lines are similar to that of stainless steel, However, at higher pulse numbers (7500 and 10000 pulses), there is a reduction in the contact angle generally. It can also be seen that there is not a distinct peak in the contact angle at a single processing speed when larger numbers of pulses are applied.

The contact angles which are presented in figures Figure 5.9 Figure 5.10 show an increase in comparison to the values of both flat and roughened surfaces that have been reported previously [114]. Unfortunately, specific roughness measurements were not made of these surfaces however the peak contact angle for stainless steel was $\sim 140^\circ$ and for titanium $\sim 68^\circ$.

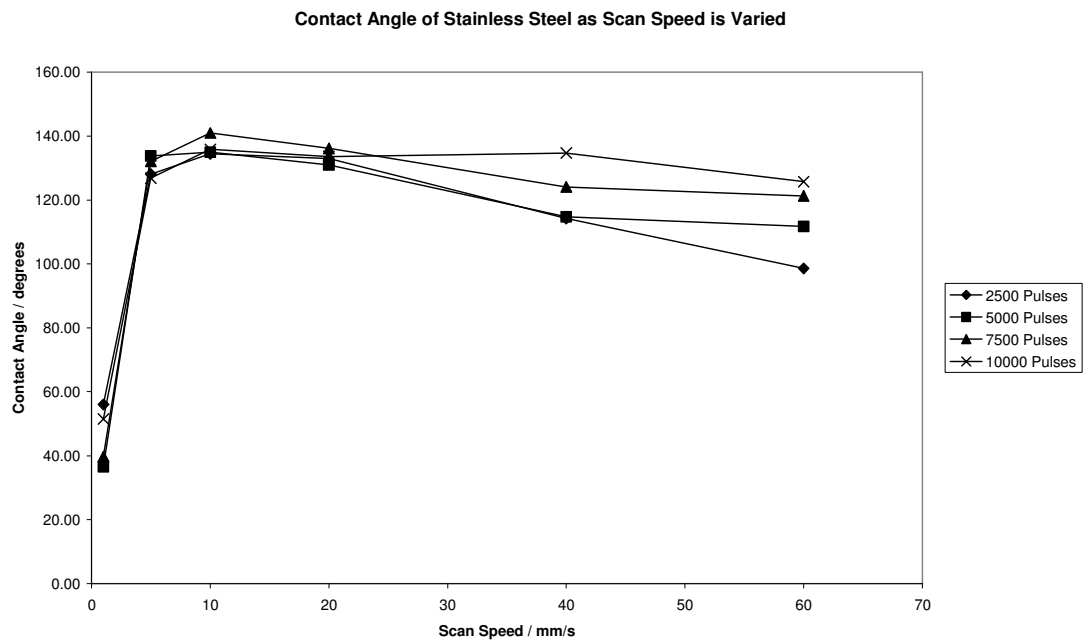


Figure 5.9. Graph to show contact angle measurements as a function of laser scan speed at various numbers of pulses on microstructured stainless steel. Time between laser processing and contact angle measurement, 15 days

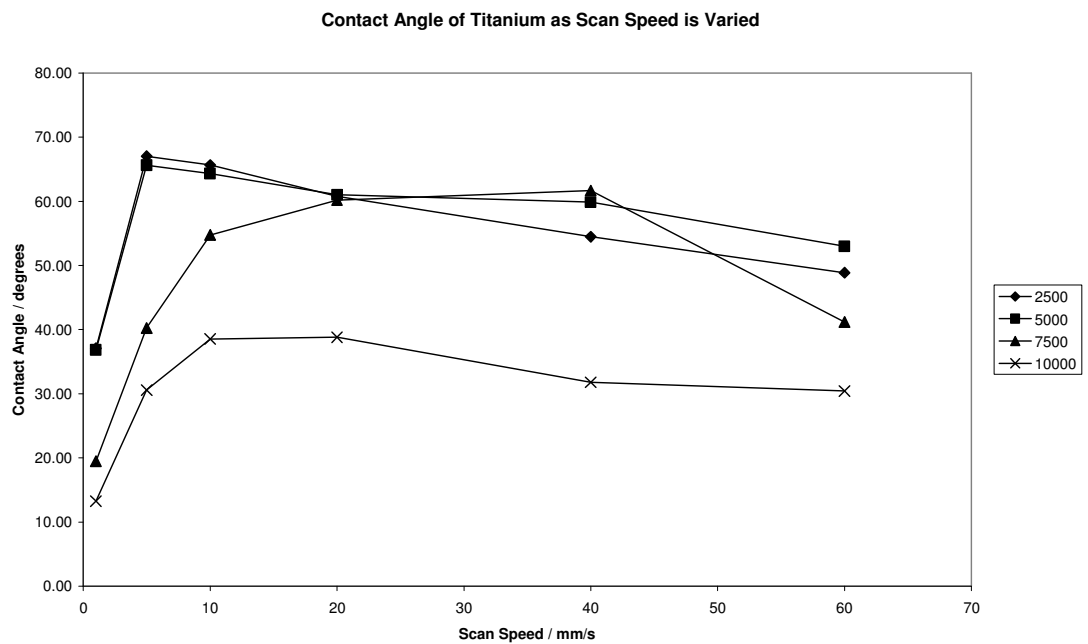


Figure 5.10. Graph to show contact angle measurements as a function of laser scan speed at various numbers of pulses on microstructured titanium. Time between laser processing and contact angle measurement, 14 days

5.5 Development of Contact Angles Over Long Time Periods

The investigation of how the contact angle changes over longer periods, in this case approximately one month, was undertaken after it was noticed that the contact angle is very low when measured shortly after laser processing. It has been reported previously that the wettability of Aluminium [115] and Magnesium [116] is also susceptible to an increase in contact angle over time. In previous cases, this has been attributed to the growth of an oxide layer after processing.

Figure 5.11 shows how the contact angle of a laser structured surface changes in comparison to the same material when it is untreated.

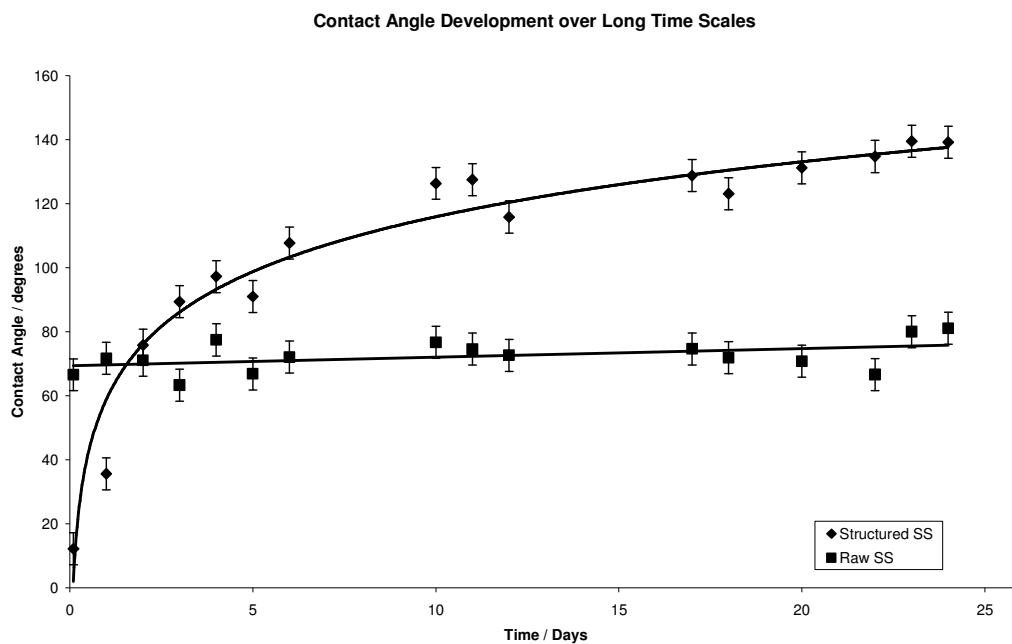


Figure 5.11. Graph to show the increase and development of contact angle measurement on laser textured stainless steel over long time periods in comparison to an untreated sample. The structured sample was processed at a fluence of 3.6Jcm^{-2} . Approximately 10^3 pulses were applied per spot during four processing passes at a speed of 10mm/s .

It can be seen that there is a sharp increase in the contact angle over the first 5-7 days and then the contact angle begins to plateau, eventually settling at a value of around 140°.

The change of contact angle over relatively long time periods raises another point about the mechanism of the contact angle change. After laser processing the surface topography present on a sample surface will change very little. Therefore any change to the surface which allows an increase in contact angle must be chemical in nature. Recent studies by Kietzig *et al* [117] have investigated the development of contact angles over time on laser processed alloys including AISI 304 stainless steel. Their work has shown that when active Magnetite $\text{Fe}_3\text{O}_4 - \delta$ ($0 < \delta < 1$), a nonstoichiometric, oxygen deficient iron oxide scale, is exposed to suitable atmospheres, dissociative absorption of carbon dioxide occurs [118]. When this happens, it is thought that carbon dioxide becomes carbon monoxide and zero valence carbon. Oxygen anions are then transferred into the lattice vacancies of the steel alloy to form stoichiometric Fe_3O_4 . It is known that this reaction has a very slow rate and would account for the observed change in contact angle.

To investigate further, a sample was prepared and subjected to analysis by X-ray Diffractometry (XRD). This sample was processed using the Violino marking system discussed in previous chapters. A laser beam, with spot size 55 μm was scanned over the stainless steel (AISI 304) surface in a raster scanned pattern. The processing speed was 20mm/s was used and 12 passes were made resulting in approximately 1000 pulses being fired at any given point in the processing area. The fluence used was 4.6 Jcm^{-2} . This sample was stored for a period of three months. This was done so that any changes

in surface chemistry would have time to develop. The sample was stored in polyurethane sample bag before analysis using low angle XRD. The results of this analysis can be seen in Figure 5.12 and Table 5-1.

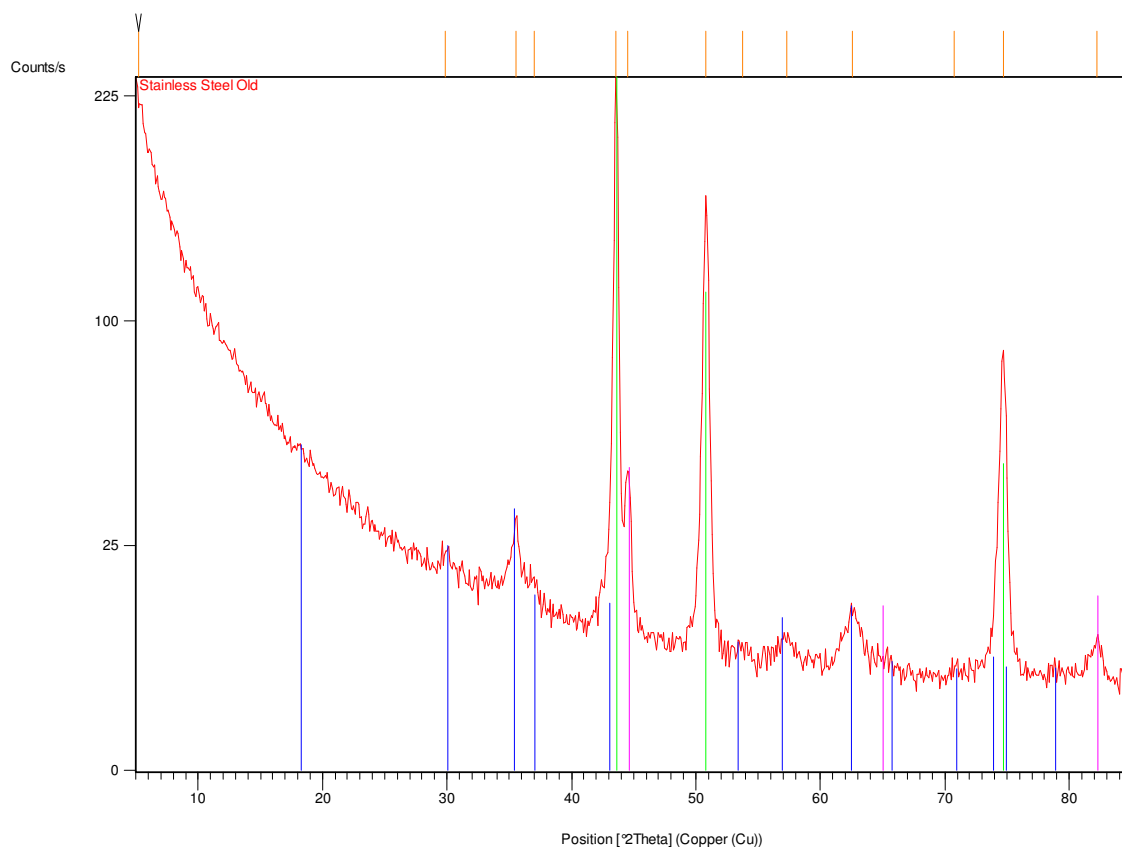


Figure 5.12. XRD data of a laser processed Stainless steel sample after a three month period




Compound Name	Scale Factor	Chemical Formula	
Chromium Nickel	1.117	CrNi	
Magnetite	0.074	Fe ₃ O ₄	
Ferrite	0.143	Fe	

Table 5-1. Compounds present on the surface of a laser processed stainless steel sample after a three month period.

It is expected that Ferrite and Chromium Nickel compounds are found on the surface of laser processed AISI 304 stainless steel as these are constituents of the substrate. However, in addition to these, the oxide magnetite is also present. This is in agreement with the work of Kietzig *et al.* This confirms, by an alternate method, that the hypothesis that contact angle increase is due to carbon contamination as a result of the dissociative absorption of CO_2 is correct. One of the sources of this carbon contamination is thought to be the polyurethane bags in which the samples were stored. Although it was thought that this method of storage would provide sufficient sample protection, this effect was discovered at such a point during the investigation that to repeat all of the work up to that point would have been impractical. It was therefore decided to carry on with the same method under the assumption that any contamination caused would be common to all samples.

5.6 Contact Angles of Angled Structures

In Section 4.3.5, it was shown that it is possible to create microstructures which are formed at an angle to the original surface by changing the incident angle of the laser beam. One reason for doing this was to find out if the structure angle has any effect on the overall contact angle.

If we take a moment to contemplate this, it can be hypothesized that an angled structure on a hydrophilic substrate, such as stainless steel, would have a lower contact angle than that of a surface with structures which are normal to the surface. The reason for this is that the area of the surface which is in contact with the droplet will be higher in the case of an angled structure. The smaller the angle between the structure and the substrate, the

more of the microstructure surface area will be available to be in contact with the droplet.

The surfaces produced were the same as those discussed in Chapter 4. Therefore the contact angle of structures with angles of 45, 60 and 15 degrees were measured. The period of these structures is approximately 50 μm . The results from these contact angle measurements can be seen in Figure 5.13.

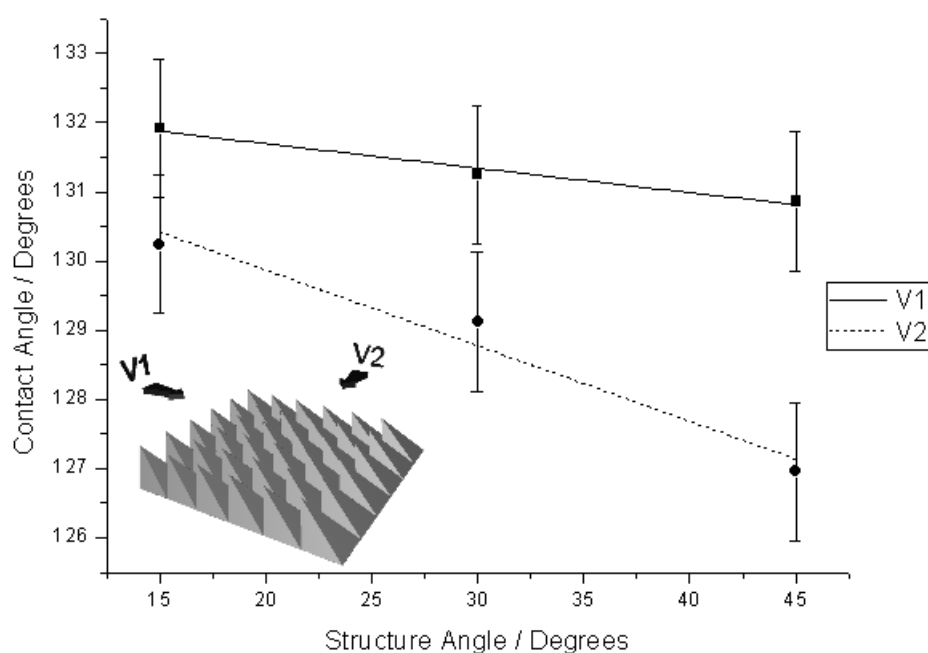


Figure 5.13. Contact Angles of Angled structures on stainless steel. Insert; Visualisation of Surface structure and viewpoints.

Figure 5.13 shows that as the angle of the structure increases, there is a drop in the contact angle from the point of view of V1 and V2. The decrease of contact angle is sharper when viewed from V2 because this is the plane where the water droplet is increasingly in contact with the structures surface. The contact angle from the point of view of V1 stays relatively unchanged because the profile of the surface structure effectively does not change.

5.7 Conclusions

From the contact angle measurements that have been reported, there are several conclusions which can be drawn. It has been shown that as predicted, increasing the roughness of stainless steel and titanium surfaces by generating periodic microstructures using lasers, can increase the contact angle of droplets placed on the surface. It was found that contact angles of up to 140° could be measured on both stainless steel and titanium. This was done by changing surface topography using the techniques shown in Chapter 4.

It was found that the highest contact angles were produced on stainless steel at an optimum scanning speed of 10mm/s. On titanium, this speed was slightly lower at 5-10mm/s. On stainless steel, the application of larger numbers of laser pulses generally increased the contact angle when compared to structures produced at the same speed with lower numbers of pulses. However, the highest contact angles were always produced at a scan speed of ~ 10 mm/s. The effect of larger numbers of pulses at any speed on titanium had the opposite effect. As the number of pulses was increased at any speed, there was a decrease in the contact angle.

It was found that laser processed stainless steel surfaces were extremely hydrophilic only a few hours after laser processing. It was then found that the contact angle of these surfaces increased in a logarithmic manner in the weeks after laser processing. It was found that over a 24 day period, the contact angle increased for almost zero to $\sim 140^\circ$. This is thought to be because of the growth of an oxide layer or contamination from the atmosphere. However this is still under investigation and will be the subject of future

work. It should, however, be noted that after the 24 day period, the surfaces were washed in an ultrasonic bath with ethanol and the wettability was unchanged. This may suggest that an oxide layer has been formed.

When a short investigation was made into the effect the structure angle has on the wettability, it was found that as the angle of the surface structure increased, the contact angle decreased. This is because as the structure angle increases, the surface area of the structure which is in contact with the liquid is increased and less of the liquid is in contact with air and the surface fractions of air-liquid and material-liquid contact are changed slightly and a lower contact angle is favored.

6 MODIFICATION OF SURFACE REFLECTIVITY

6.1 Introduction

During studies of laser generated microstructures on metal surfaces it has been noted that after processing and regardless of material used, the surface obtained exhibits decreased reflectivity or has become completely black in appearance [119, 120]. This has also been reported for semiconductor materials such as silicon [121] as well as a number of other materials [122-124]. Having been reported on multiple materials, it can be assumed that this effect occurs due to a structural change on the surface as this is the commonality in all cases.

The way a surface reflects light depends greatly on its surface finish. As with any surface, light will reflect at an angle equal to the incident angle. If a surface is flat, as is the case with a mirror, then the reflected light will form an image of the surroundings. The opposite of this case is to intentionally diffuse the light incident on a surface. These variations in the type of reflection, which occur, can be seen in Figure 6.1.

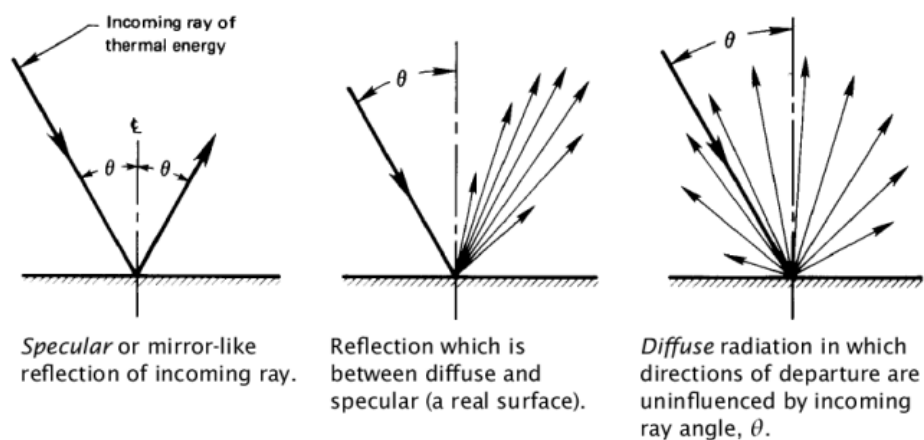


Figure 6.1. Visualization of specular and diffuse reflectivity [96]

Perhaps the simplest enhancement of reflectivity is the modification of surface roughness and topography. If this concept is taken further, it is possible to engineer the surface to direct reflected light towards another part of the surface after its first interaction with a surface. This means that the residual energy from the first interaction has the opportunity to be absorbed by another part of the surface.

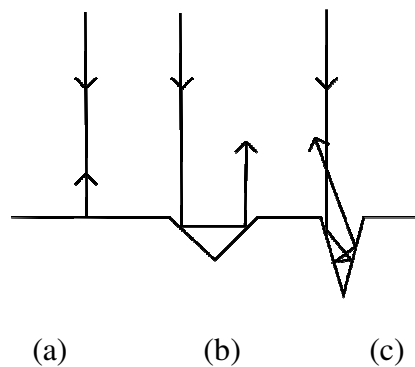


Figure 6.2 Beam paths of light rays incident onto three cavity shapes at normal incidence.

Figure 6.2 shows an example of three surface shapes that will have varying effects on the intensity of light reflected away from the surface. A photon interacting with a flat surface will only encounter one reflection, regardless of the incident angle. More reflections can be induced by forming steep sided features on the surface. Figure 6.2(b) is an example of a special case. Known as a retro-reflector, a V-shape with a wall angle of 45° will reflect light on a vector parallel to the initial incident ray. Once the wall angle increases beyond this, it is possible for higher numbers of interactions to occur, as seen in Figure 6.2(c). Although this example only considers two dimensions, these same properties apply to three dimensional structures. Additionally, if the surface is roughened in some way, more diffuse reflection occurs, decreasing the probability of reflection away from the surface.

Factors that have been overlooked until this point are the reflectivity of a surface due to its chemistry or colour. The chemical properties of a surface determine the absorption depending on the wavelength, hence energy, of incident photons.

6.2 Reflectivity of Laser Processed Stainless Steel and Copper.

In initial experiments, reflectivity measurements were taken from surfaces of stainless steel (AISI 304) and pure Copper (99.999) which had been structured by nanosecond laser processing. Samples were processed using a frequency doubled Nd:YVO₄ marking laser with a wavelength of 532nm, $\tau=7\text{ns}$, $\nu=30\text{kHz}$, $F = 2.81 \text{ Jcm}^{-2}$. The spot size of the laser was 55 μm , which was equal to the hatch distance used. In the experiments, a low number of pulses per spot were fired at the target, ranging from 66 (1 pass) to 198 (3 passes). The laser scanning speed used was 25mm/s.

Reflectivity of the samples was measured using a UV-Vis Spectrophotometer (Analytik Jena Specord 250) with the ability to measure between 360 and 1100nm. An integrating sphere allows the overall reflectivity of the surface to be obtained.

SEM images of the surfaces can be seen in Figure 6.3 and Figure 6.4. Here it can be seen that the surface morphology is a highly periodic groove and ridge structure. The reason that this type of structure can be seen rather than the periodic microstructures as seen in chapter four is the low number of laser pulses and relatively high processing speed used.

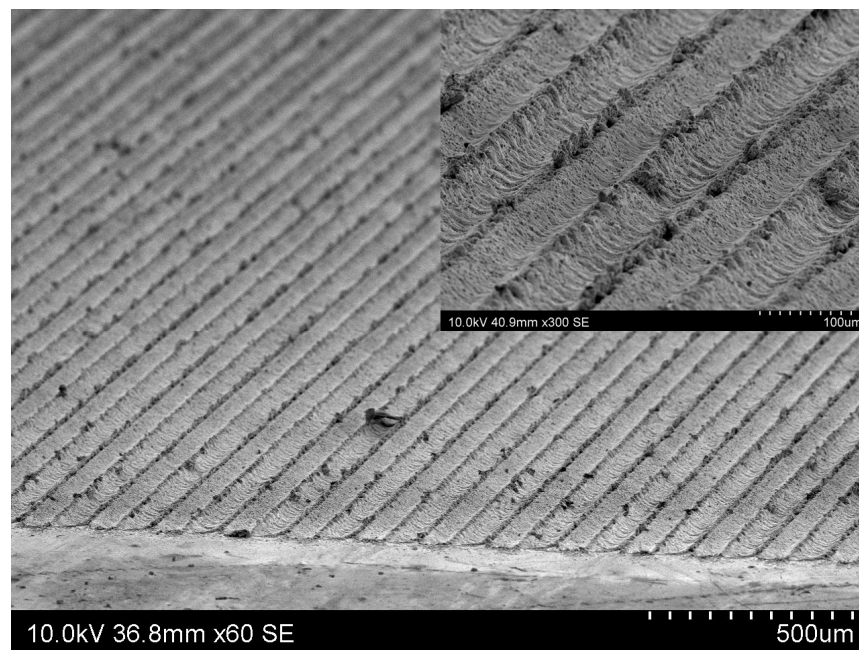


Figure 6.3 Stainless steel surface after one pass has been made in an effort to modify reflectivity. Inset: The same surface at higher magnification. Due to the low number of pulses used, only a periodic trough and peak structure can be seen.

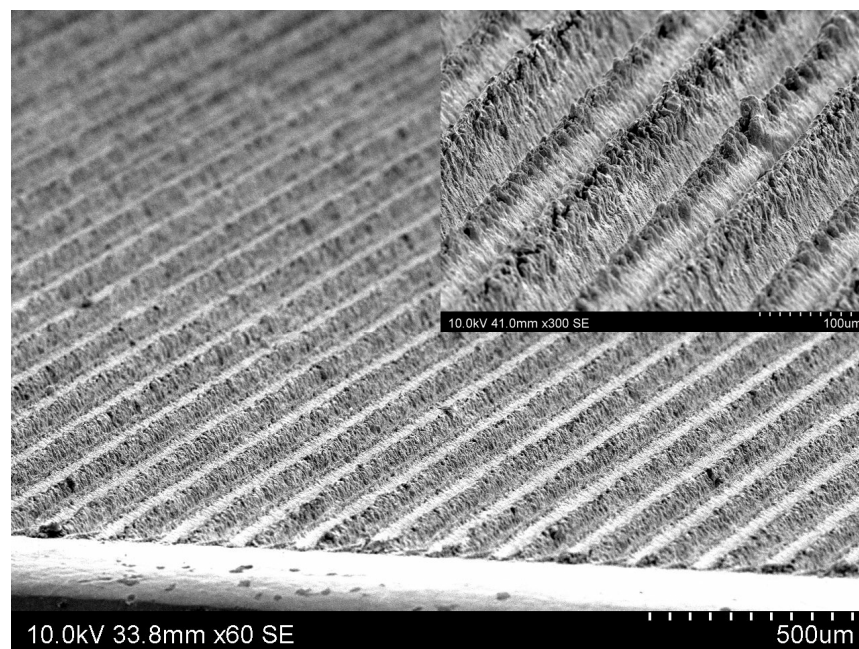


Figure 6.4 Copper surface after three passes have been made in an effort to modify reflectivity. Inset: The same surface at higher magnification. As the number of passes increases, more individual structures begin to develop

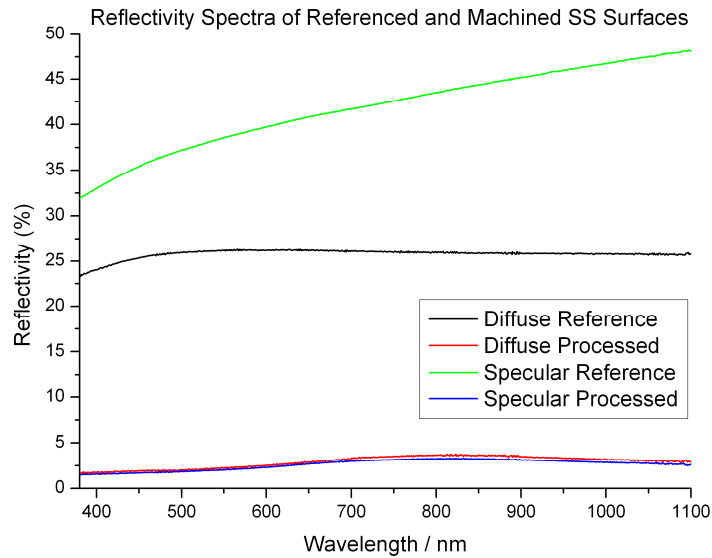


Figure 6.5. Diffuse and specular reflectivity spectra of reference and a laser processed (fig.3.21) stainless steel surface. Reflectivity is reduced by upto 45%. Diffuse and specular reflectivity are almost identical post processing due to high roughness of microstructure.

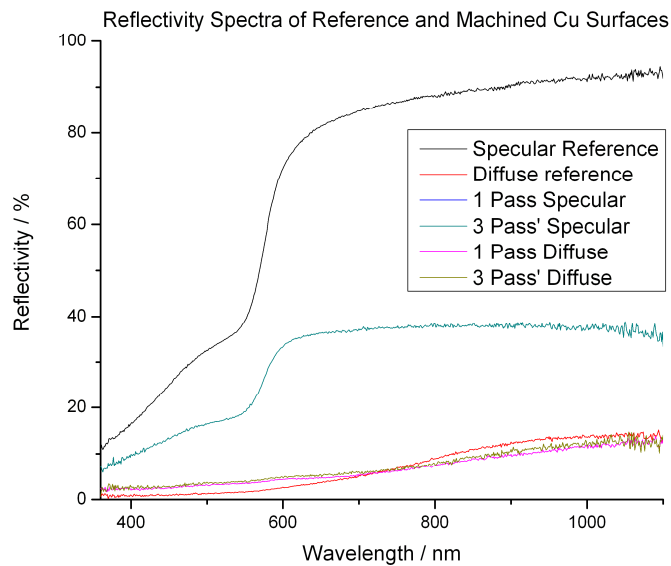


Figure 6.6. Diffuse and specular reflectivity spectra of reference and a laser processed (fig.3.22) copper surface. Most interesting in this case is the reduction in reflectivity at wavelengths about 600nm. In this region most of the energy which would otherwise be reflected is absorbed by the sample.

After laser processing, these surfaces had a black tone as expected. To further understand the extent of this increase in absorption; the reflectivity of the surfaces was measured. Figure 6.5 and Figure 6.6 are plots of the diffuse and specular reflectivity spectra of reference and laser processed stainless steel and copper surfaces. The first thing, which is obvious from these figures, is the reduction in the percentage of reflected light due to laser processing and the resultant topography. In the case of stainless steel, this reduction is 30-45% and on copper between 10 and 80% depending on the wavelength and type of reflectivity measured. In Figure 6.5, it is noted that the difference between the specular and diffuse reflectivity of the sample is negated by the laser processing, after which the values of both types of measured reflectivity are almost identical. In this case this would mean that no light is reflected specularly. Hence measurement with an integrating sphere gives the same result in both modes.

Given a high enough intensity of light the absorption of photons will impart enough energy to the surface and through conduction the bulk temperature of the metal will rise. With possible applications in solar thermal technology in mind, it was decided to measure how Copper surfaces react to focussed white light.

6.3 Preparation and Characterisation of Surface Microstructures for Solar Energy Harvesting

6.3.1 Introduction

In this approach, a discussion of how various laser processed, coated and plain (uncoated) surfaces behave under exposure to focused white light is investigated. Although it is expected that the surfaces under study would experience a rise in temperature, the main focus here is to elucidate how the absorption increase compares to conventional surfaces, and to characterise the optical absorption efficiencies during exposure to simulated sunlight. Through an appreciation of surface texture, micromachining conditions and optical absorption uses for applications in energy harvesting are envisaged.

6.3.2 Experimental

Using knowledge from previously reported work [119, 120] a range of laser processed surfaces were produced on 0.8mm thick pure Copper sheets approximately 25mm square. This was undertaken out in order to yield an appropriate array of samples with varied textures or roughness. The surfaces were processed using a Nd:YVO₄ (Laservall) laser system ($\lambda=532\text{nm}$, $\tau=7\text{ns}$, $P_{\text{AVG}}=1.08\text{W}$, $\nu=30\text{kHz}$, $2\omega_0=55\mu\text{m}$, $M^2\sim 1.5$, $F=6.49\text{Jcm}^{-2}$) at processing speeds of 5, 10, 20 and 50mm/s. The beam is scanned in an interlaced pattern and the distance between scan lines is equal to the laser spot size. So

that the effect of oxide layer formation can be quantified, laser processing is carried out in both air and argon atmospheres. To do this, a processing chamber, filled with argon is utilised. This chamber was purged for one minute at a regulator pressure of 3psi before processing commenced. The gas flow continued until processing was completed.

The newly produced surfaces were then be analysed using a number of techniques. Measurements of the optical properties of the surfaces are made using a UV-Vis Spectrophotometer (Analytik Jena Specord 250) in conjunction with an integrating sphere. To inspect the physical attributes of the surfaces, Scanning Electron Microscopy (Hitachi s-3400N) in conjunction with Alicona MEX software is used to produce three dimensional digital models of the surfaces. In addition to this, analysis by X-Ray Diffraction (XRD) is used to identify the species of copper oxide which grow on the surface during laser processing in air. This technique is also used to confirm the lack of oxide on samples processed in Argon atmospheres.

To measure the response of the surfaces to an optical impulse, the experimental arrangement shown in Figure 6.7 was used. To heat the samples, a halogen lamp with an output of 1.3W was used. Focusing of the white light to a spot size of ~15mm resulted in an optical intensity of $\sim 7.3\text{kWm}^{-2}$ at the target surface. For comparison, the irradiance of the Sun, unfocused, is approximately 642 Wm^{-2} [96]. Using the same optical arrangement and replacing the light source with the sun could produce an intensity of over 25MWm^{-2} in a 15mm focal spot.

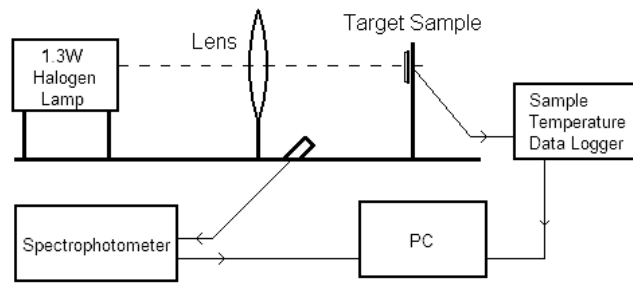


Figure 6.7. Arrangement of equipment used to measure thermal response. Temperature was measured using a K-type thermocouple attached to the back of the 0.8mm thick sample. Back-reflected light was measured from an arbitrary point. The temperature data was captured using a Keithley Instruments 2701 digital multimeter equipped with a M7706 data acquisition module.

The output spectrum of the light source used can be seen in Figure 6.8. Here, a normalised comparison to the output spectrum of the sun is shown. As can be seen, the solar analogue has an output roughly similar to the output of the sun.

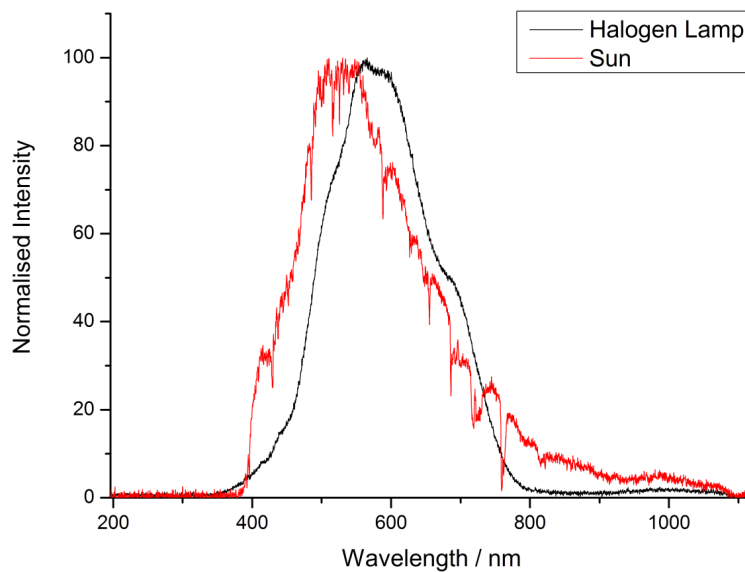


Figure 6.8. A comparison of the output of the artificial light source used and optical solar radiation. The output spectra of these sources have been normalised. The loss of spectral data in the UV wavelengths (<400nm) for solar radiation is due to the attenuation of these wavelengths by an optical filter which was a necessary part of the experimental arrangement.

6.3.3 *Reflectivity of Surfaces*

The reflectivity spectra of the laser processed metallic surfaces show a substantial improvement in absorption with respect to surfaces that were left unprocessed, as can be seen from Figure 6.9. It can also be seen the overall shape of the reflectivity spectra varies depending on the atmosphere used during processing. In the case of copper (Cu 99.999% grade), a distinctive rise in reflectivity around 550 to 600 nm can be seen. This accounts for its reddish lustre. For Cu samples processed in an Argon atmosphere, this observation can still be made. However, the reflectivity is diminished. Much of the absorption enhancement can be attributed to roughening of the surface. On the other hand, Cu samples processed in air do not exhibit the same reflectivity spectrum profile. This can be explained by the formation of localised copper oxides immediately after processing in air yielding a much darker and therefore more absorbing spectral profile. Darkening surfaces of Cu with carbon paint, shows similar levels of absorption as samples processed in air. This helps separate those effects which are due to the topographical features of the studied surfaces rather than their apparent colour.

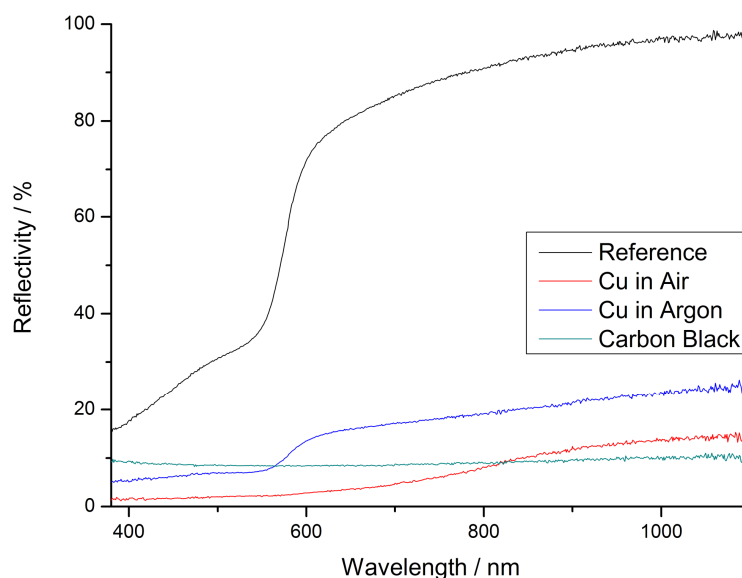


Figure 6.9. Reflectivity spectra of four samples shows overall a decrease in reflectivity before and after processing. This was observed at a translation speed of 5mm/s, in Air and Argon atmospheres. The samples processed in air exhibit a fairly similar absorption to those coated with a carbon based black coating (Carbon Black)

A microscopic examination of surfaces processed under the same conditions, except for the atmosphere, reveals some interesting clues. Figure 6.10a and b show two copper surfaces, processed using the same laser parameters, processed at 5mm/s and a fluence of 7.4 Jcm^{-2} . However, it is obvious that these two surfaces have very different microstructure formations present.

Considering that surfaces shown in Figure 6.10 were produced in air and argon atmospheres respectively it is possible to hypothesise how this difference came about.

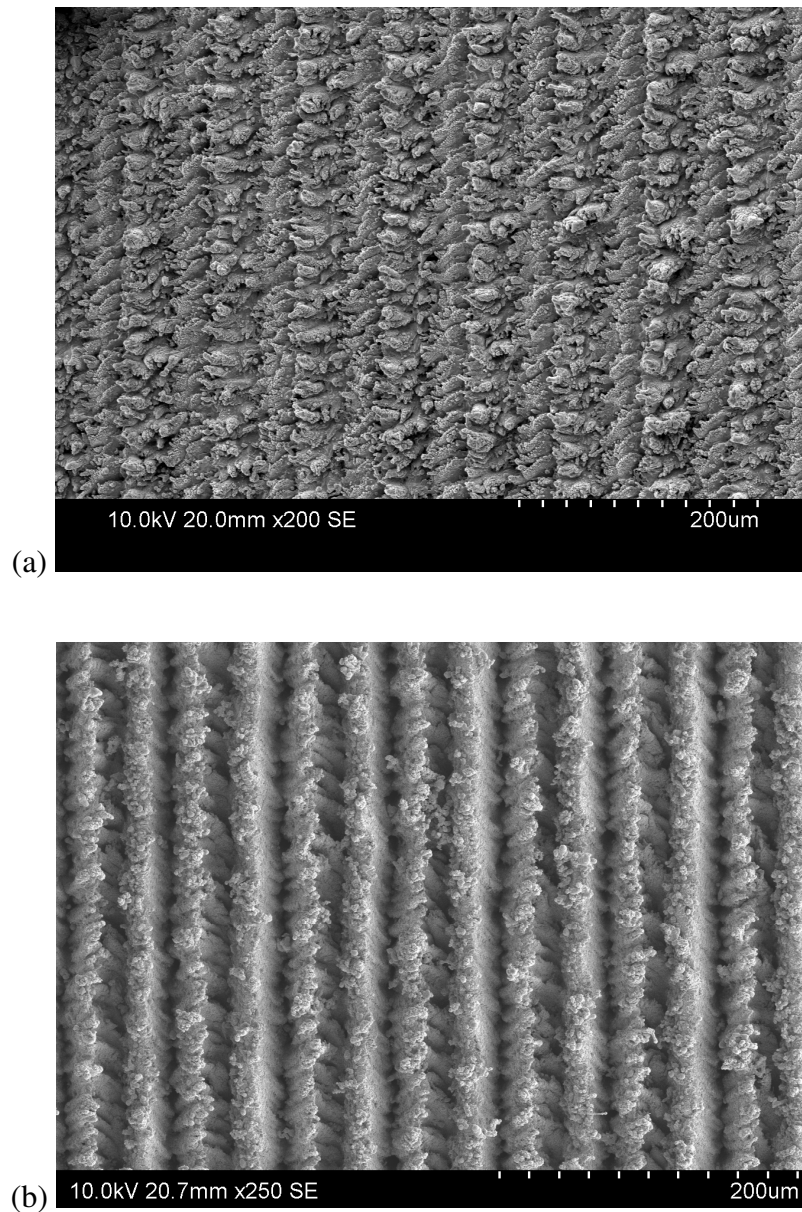


Figure 6.10. SEM Micrographs of Copper surfaces processed under air (A) and Argon (B) atmospheres. The same parameters, 5mm/s, 7.4 J/cm^2 are used to produce each. Differences in surface structure occur due to oxide formation between processing passes.

Previous work [120] has shown that these types of structures form when a Gaussian irradiance profile of a laser beam is such that the central region of the beam allows for ablation while its peripheries only melt the target material, so that the structural surface mobility of the metal is increased. As the products of ablation expand from the ablation site at the centre of the beam path, the force of this expansion pushes molten material

towards the edge of the path along which the beam is travelling. Moreover, to deposit the required number of pulses per spot, multiple passes were made over the surface.

When a sample is processed in air, an oxide layer will be present after a single pass. This oxide layer will then, as we have seen, affect the reflectivity of the surface and the laser material interaction during the second pass and successive passes. Effectively, the oxide layer acts to increase the absorption of laser light. An artefact of this is that after preparation of samples in both atmospheres, the surface of those processed in air is further below the datum of the sample than those processed in Argon. This would suggest that more vaporisation of material would have taken place on surfaces where an oxide layer increased absorption of laser light.

6.3.4 Identification of oxide species.

To understand the nature of the oxide layer present when processing in an air environment, low angle XRD analysis was used to identify the species of oxide present. For comparison, the same analysis was carried out on a sample processed in an Argon environment where it is expected that no oxide formation would be able to take place. The results of this analysis can be seen in Figure 6.11 and Figure 6.12 and their adjacent tables show the corresponding key, chemical compounds and scale factors. It can be seen from analysis of the copper sample processed in air that there are two species of copper oxide present in addition to the substrate material.

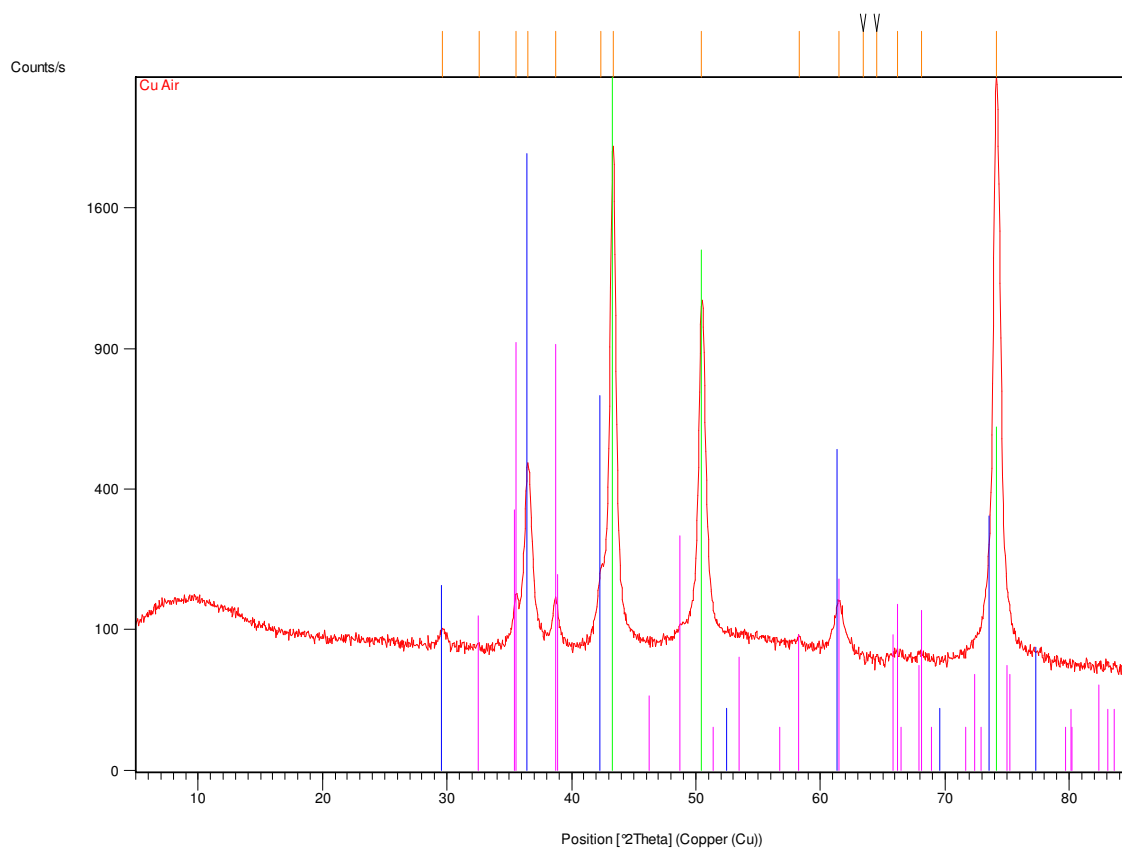


Figure 6.11 XRD data from copper samples processed in an atmosphere of Air.

Compound Name	Chemical Formula	Scale Factor	
Copper	Cu	0.919	■
Cuprite	Cu_{2+1}O	0.144	■
Tenorite	CuO	0.037	■

Table 6-1. Compounds preset on copper samples laser processed in Air.

The most abundant of these is cuprite, a very dark red or black oxide with the chemical formula Cu_2O . The second oxide present is tenorite, CuO . Again, this oxide has a black colour which is in keeping with observations.

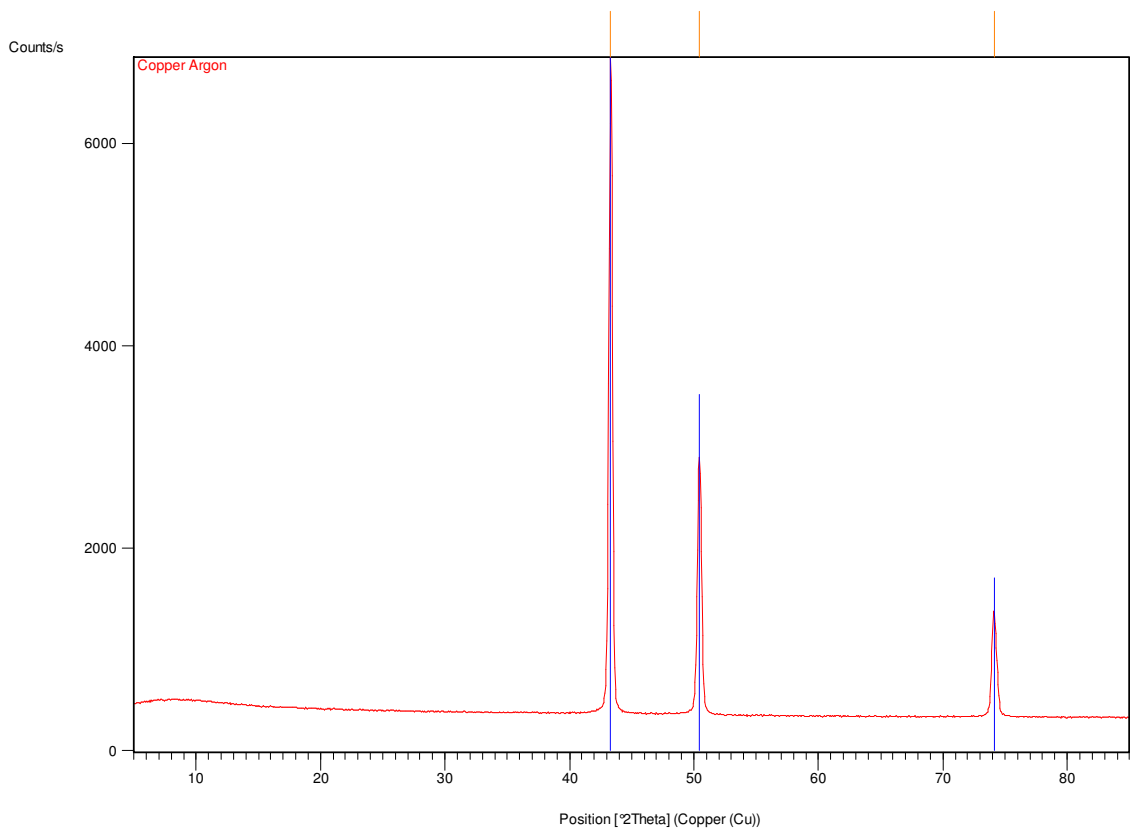


Figure 6.12 XRD data from the analysis of Copper samples which have been laser processed in an Argon atmosphere.

Compound Name	Chemical Formula	Scale Factor	
Copper	Cu	0.962	■

Table 6-2. Compounds present on copper samples laser processed in an Argon atmosphere.

6.3.5 Surface Roughness

Surface roughness can be defined in many ways. Here, it is given as the ratio, r , of the projected surface area to the actual surface area, i.e. a perfectly flat surface would have

the surface roughness, $r=1$. The data available in Figure 6.13 shows that the presence of the reported oxide layer has a substantial influence on the final roughness of the surface. The result is that a consistently higher roughness ratio is obtained for surfaces processed in an argon atmosphere. This change in roughness of different laser processed surfaces can be attributed directly to the gas environment in which they are processed. In Air an oxide layer will form after the first processing pass. On subsequent passes, the increased absorption which this layer facilitates will allow more surface heating to occur and ablation will be less efficient. Conversely, in Argon, each processing pass will be processing on an oxide free surface. Due to the intensity distribution of a Gaussian Beam, the highest beam intensities, and thus heat, are confined to the centre of the beam path. This allows higher aspect ratio grooves to be formed in the surface. These further increase the actual surface area in comparison to those processed in air.

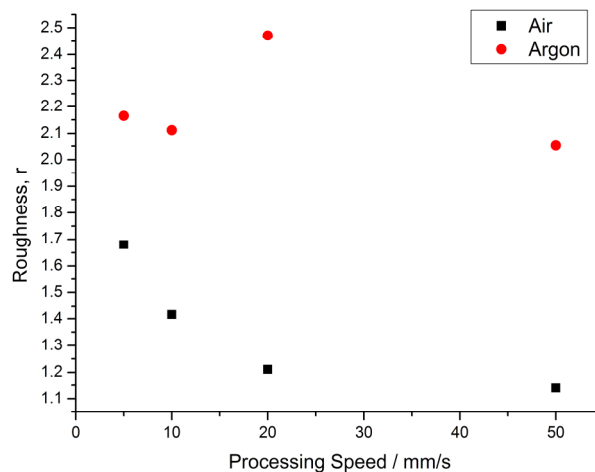


Figure 6.13. The surface roughness ratio of samples processed in Air (left), that is the ratio between the projected and true surface areas, is generally lower than those processed in Argon (right). This is due to the formation of an oxide layer after the first processing pass, leading to the occurrence of more surface heating and less ablation.

6.3.6 Back Reflection

In addition to measuring the bulk reflectivity of the tested samples, the spectrum of light reflected from the sample was measured. The spectra from these measurements can be seen in Figure 6.14.

What is immediately obvious from these two graphs is that the two types of surfaces measured have different absorption characteristics. In the case of surfaces processed in Argon the shape of the reflected spectrum closely resembles that of light reflected from a virgin copper surface. However, for surfaces processed in Air, the shape shows that different wavelengths of light are absorbed more readily than others. Generally, surfaces processed in air absorb more light than those processed in Argon. This is not surprising. Darker surfaces, by definition are more absorbent.

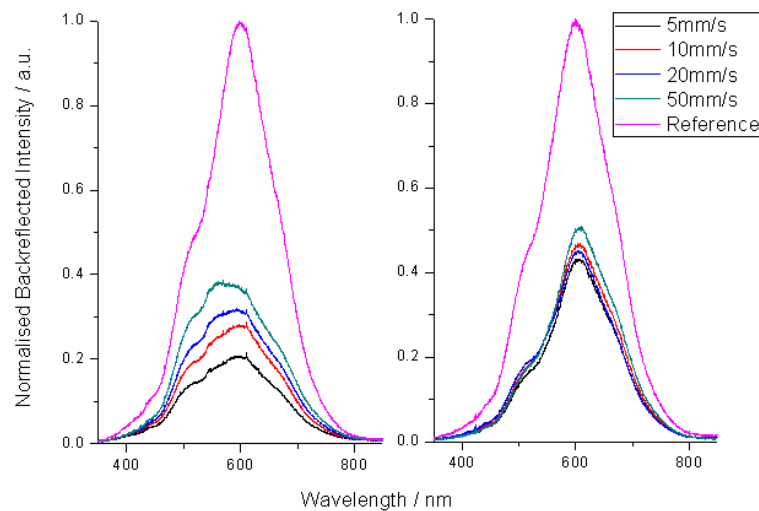


Figure 6.14. As the translation speed increases, it can be seen that the difference in relative backreflections are more pronounced in air than in an argon atmosphere. The light reflected from laser processed surfaces gives a good indication that the presence of an oxide layer improves absorption over the whole spectrum.

6.3.7 Heating of Samples by White Light.

By measuring the Dynamic thermal response of surfaces to a finite impulse (1250 seconds) of illumination, the amount of energy absorbed by the samples could be approximated using the relationship;

$$E=mc\Delta T$$

6.1

where the specific heat capacity, c , was taken to be $391 \text{ J.kg}^{-1}\text{K}^{-1}$ [96]. The thermal energy of four copper samples (two laser processed in Air and Argon respectively, one coated in carbon paint and one untreated) measured during their heating and subsequent cooling can be seen in Figure 6.15.

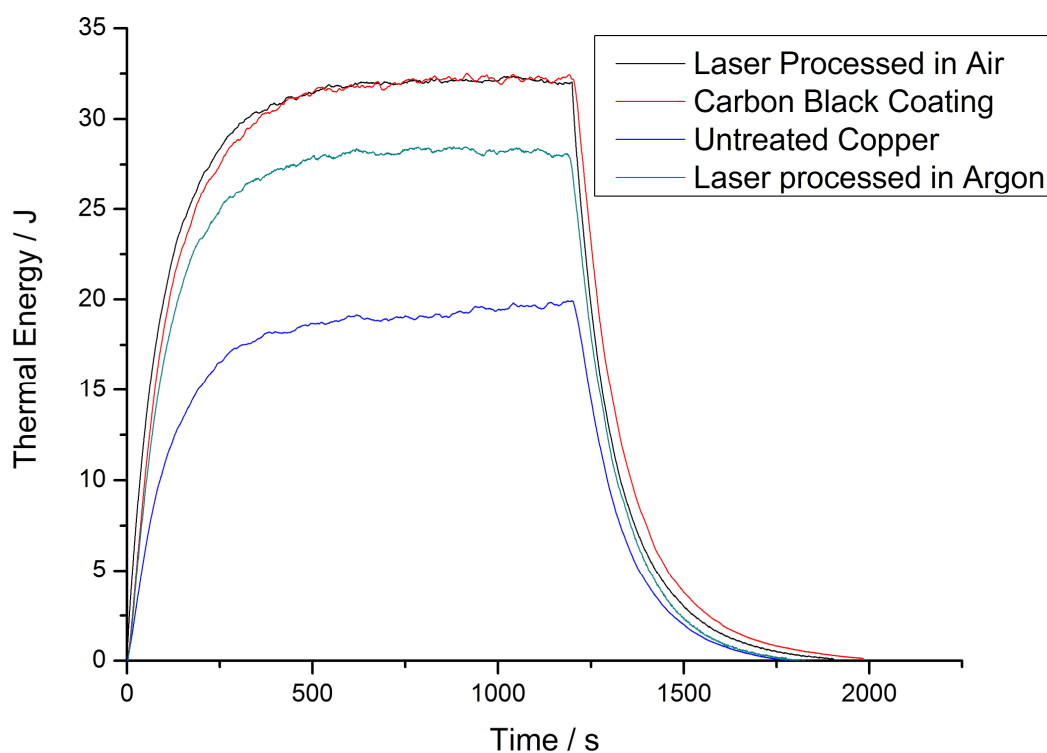


Figure 6.15 Thermal energy of various copper samples in response to an optical impulse.

The highest temperature recorded was approximately 65°C. This is a 45 degree rise from the starting temperature of 20°C. It can be seen from Figure 6.15 that the degree of temperature rise in the various tested surfaces correlates well with those that are most absorbent, as shown by Figure 6.9. As is expected, the lower the surface reflectivity, the more energy is absorbed. The most efficiently absorbing samples are the sample laser processed in air and also the sample coated in carbon paint. Although these two surfaces reach approximately the same steady state energy, the conversion of light into heat is faster for the laser processed sample. This is clear because while the heating of samples begins at the same time and temperature, the energy of the laser processed surface is consistently ahead of the painted surface until the plateau is reached. This faster response is thought to be brought about due to a lack of paint impeding heating. Rather than light having to heat paint, which then heats the copper substrate by conduction, the laser processed surface interacts directly with the incident light.

6.3.8 Conclusions

A study of laser processed copper surfaces for the purposes of investigating reflectivity and heat absorption has been carried out. The observations made provide new insight into producing novel surfaces and topographies pertinent to the research effort for the production of energy, in the form of heat, from solar radiation. The findings of this investigation show that absorption increases with higher roughness ratio values. It is thought that this is due to increased surface area and incoming light experiencing an increased number of reflections due to surface geometry. In addition to this, the surface chemistry also has a distinct effect on reflectivity. Surfaces processed in inert

environments display higher reflectivity than those processed in air. On copper, the formation of an oxide layer, an artefact of processing in Air, gives a black, absorbent optical surface. This increases absorption of optical EM radiation and findings show that heating due to increased absorption is competitive with conventional ‘black’ coatings. In addition to this, the speed of thermal response is marginally faster.

7 CONCLUSIONS

This PhD has three main points of interest. These are the modification of surface topography on metals with micron and sub-micron feature sizes, the modification of wettability and the modification of reflectivity. This chapter is intended to give a summary of the results of these investigations. Firstly, the formation of these topographical structures will be discussed first before moving on to their applications.

It has been found that the types of structures which can be produced by self-assembled methods of laser processing vary widely. Depending on parameters such as the laser power, processing speed, laser pulse duration and the number of pulses applied, the surface topography produced can vary greatly. Experiments concentrated on the production of microstructures by processing stainless steel (AISI 304) samples. This processing was completed using the fundamental (1064nm) and frequency doubled (532nm) output from DPSS Nd:YVO₄ lasers. These systems had a pulse duration of 7ns and repetition rate of 30kHz.

Results have shown that at fluences marginally above the ablation threshold of the target material a reasonably large amount of molten material is formed at the same time as ablation takes place. This is due to the Gaussian intensity profile of the laser beams used. As expanding ablation products interact with the molten material, differences in surface tension cause instabilities in the melt pool allowing molten material increased surface mobility. Over reasonably large numbers of pulses this results in the formation of structures on the surface on metal targets.

Initial experiments showed that it is possible to produce structures in both liquid and gaseous environments. Although features produced in both environments have a similar shape, their characteristic size is different. In air the feature size is comparable to the laser spot size. It was found that processing in liquid reduced this to approximately half of this value. It is thought that this is due to the cooling effects of a liquid environment decreasing the ability of molten material to flow before it re-solidifies. Further experiments concentrating on the number of pulses necessary to form features found that surfaces with similar topographies could be achieved with as few as 1500 pulses. It was also noted that higher numbers of pulses begin to remove material and produce structures further below the original surface.

Until this point all processing had taken place under conditions where the distance between consecutive laser scan lines (hatch distance) provided a fixed overlap between 30-40%. To try to reduce the time necessary to produce these structures it was decided that an investigation into the effect of changing the hatch distance was required. To do this a similar laser operating at a wavelength of 1064nm was used. When the hatch distance was changed from values of 10 μ m to 60 μ m (laser spot size 50 μ m) it was found that a close correlation was found between the hatch distance and structure period until the hatch distance exceeded the laser spot size. When the hatch distance exceeded the laser spot size areas of the surface between scan lines remained unprocessed.

It has been found that, for stainless steel, operating at a fluence of $\sim 3.5\text{Jcm}^{-2}$ allows the production of highly organised periodic structures. These are formed by a process which depends on a cycle of melting and re-solidification. It was found that at these fluences increasing the scanning speed and hatch distance have important roles to play in the

formation of structures. As speed increases, the cumulative heating effect from laser pulses declines and individual structures become less defined. It was found that well defined structures are formed at a scanning speed of 15 – 25 mm/s.

Another objective of this project was to methodically show that self-assembled structures align themselves to the same direction as incident laser light. It has been demonstrated that this is indeed the case. While processing with samples tilted to angles of 15, 30 and 45 degrees it has been shown that there is excellent correlation between the structure alignment and incident beam angle.

Experiments using femtosecond pulses were found to give surface topography that is drastically different to that produced using nanosecond lasers. Initial experiments found that the threshold fluence for stainless steel processed with 100fs pulses at wavelengths of 800 and 400nm was 0.077 and 0.342 Jcm⁻² respectively. This is much lower than fluences necessary for ablation using ns lasers because although only a small amount of energy is delivered per pulse of fs light, the intensity is extremely high because of the ultrashort pulse duration. Most interestingly it has been shown that femtosecond lasers are excellent at producing sub-wavelength periodic surface structures. These are produced at fluences below the ablation threshold of stainless steel and are produced when the reflected portion of incident radiation is reflected and interferes with the rest of an incoming laser pulse. Where constructive interference takes place, grooves appear and in this way, ripples, orientated perpendicular to the incident beam polarization are formed. It was found that LIPSS structures with mean periods of 295 nm and 600nm were formed at 400 and 800nm respectively. Through the application of techniques learned from producing structures with ns lasers, it has been shown that large areas can

be covered by these surfaces structures with relative ease, producing surfaces with unique properties.

The self assembled microstructures produced using ns laser have been applied to the modification of wettability on metals with some surprising results. Common methods of producing superhydrophobic surfaces can rely on processes which involve harmful chemicals and complicated processes. The use of lasers to produce superhydrophobic surfaces on stainless steel is thought to be a cleaner and simpler method of producing these surfaces.

It has been found that it entirely possible to modify the contact angle of stainless steel surfaces by laser surface topography modification. Considering that untreated stainless steel has a contact angle of $\sim 70^\circ$, it can be concluded that surface topography induces composite wetting of the surfaces. This means that a water droplet is suspended by the tips of surface topography and air is trapped in the remaining voids. It has been found that contact angles of 140° are easily achievable using this technique and in some special cases contact angles of 155° have been recorded. Confirmation that composite wetting has been induced on the surface of stainless steel can be taken from the change of contact angle depending on the angle of surface topography. Mentioned earlier, these surfaces have structures at 85, 60 and 45 degrees to the surface. Measuring their contact angle shows that surfaces with more surface area exposed to a water droplet have lower contact angles. This is in keeping with the Cassie-Baxter relationship [102].

One of the major developments of this project has been the investigation of how contact angles change over time on laser processed surfaces. Initial measurements of contact angles after laser processing seemed erratic. This was until it was noted that in the days

and weeks after laser processing the contact angle of laser processed stainless steel changes in a predictable way. Results show that over a period of 30 days, contact angles on stainless steel rise from 0° (total wetting) to around 140° , at which point they become stable. Through analysis of the surfaces using XRD it has been shown that an oxide layer of Magnetite, Fe_3O_4 , is formed on the surface of stainless steel after laser processing. This confirms reported results gained by x-ray photospectrometry (XPS) measurements in 2009 [117].

The modification of reflectivity was the final application investigated during this project. The impetus for this work was due to observations that the appearance of metal surfaces was always much darker when surface structures had been applied using lasers. To test the assumption that these new surfaces are absorbing more light at optical wavelengths, measurements of reflectivity and temperature change during and after exposure to concentrated white light were made.

The reflectivity of two metals was studied before and after laser processing using the same DPSS laser operating at 532nm as earlier experiments with a fluence of 2.8 Jcm^{-2} and scanning speed of 25mm/s. These were stainless steel (AISI 304) and copper. Copper was chosen because of obvious applications this type of surface could have in solar thermal energy applications. Having a high heat capacity yet being highly reflective at infrared wavelengths make copper an ideal candidate for enhanced absorption. Reflectivity measurements of stainless steel and copper after laser processing showed that reflectivity was greatly decreased. It has been shown that there are two reasons for this. It has been shown that both surface topography and chemistry contribute to enhanced optical absorption. By laser processing in an atmosphere of

Argon, any oxide layer formed during laser processing in air was denied the opportunity to form. From this surface an indication of the effect of surface roughness in comparison to both roughness and absorption enhancement by surface chemistry changes was established. By allowing the surfaces to be heated by white light, a comparison of their efficiency at absorbing energy from light was determined. It was found that both characteristics improve absorption by decreasing reflectivity but the colour of the surface, caused in this case by surface chemistry change is most important. It was found that surface roughness increases absorption by diffusing light over the surface and effectively stopping specular reflection. As incident light is scattered along the surface the number of reflections it encounters increases and reflectivity is decreased by over 70% across the whole spectral range measured. When an oxide layer is allowed to form during processing it was found that less than 10% of incident light is reflected. Through XRD analysis, it was found that the oxide formed during laser processing on copper is Cuprite (Cu_2O) and Tenorite (CuO).

Although many results have been found from the work done during this project, as with all scientific endeavours, further questions are raised. These are discussed in the following chapter.

8 FUTURE WORK

In this PhD study, a number of techniques have been developed and the formation of self-organised, periodic micro and nanoscale topography on various metals has been demonstrated. Continuation of fundamental research into the formation of these structures should be considered. Later developments in this project have shown that the formation of sub-wavelength structures over large areas is possible. As yet, the applications of these surfaces are not known.

Many aspects of this project are the beginning of the use of these new surfaces for real world applications. However there are still a number of details which need further investigation. Developing surfaces which increase water contact angle is probably the most promising result of this project. It has been shown that the change in surface chemistry greatly affects surface wettability but the reasons for this change are still not yet fully understood. The phenomenon of the time effect on wettability of laser-textured metallic surfaces has only been reported recently for the first time [125]. It was explained by the formation of Fe-oxides and continuous carbon decomposition occurring on the surface with time. However, we found that this time effect occurred not only on stainless steels (containing iron to form Fe-oxides), but also Ti alloys and pure Cu. More interestingly, it has also been noted to occur on Ti alloys after laser cleaning (without formation of oxides). Therefore we believe that in other explanations there are significant aspects that have been neglected. It is proposed that work be undertaken to determine the reasons for this time effect. It is believed that the exposure of laser textured surfaces in air will allow hydrocarbon contaminants deposited on the surface to increase hydrophobic behaviour. It is proposed that XPS (X-ray photoelectron

spectroscopy) is employed to measure the change of carbon contents with time. To help engineers produce functional superhydrophobic materials, the understanding of the influence of surface chemistry on the wettability of metals is important. Additionally, investigation into the corrosion properties of these new materials should be considered. It is obvious that the increase of surface area which occurs during laser processing could have a detrimental effect on the corrosion of surfaces. If applications in the real world are to be developed, robust, long lifetime surfaces are crucial.

The observations of laser-textured copper surface for the purposes of investigating reflectivity and heat absorption have provided a new insight into producing novel surface structures pertinent to the research effort for the production of energy. It has been shown that both surface roughness and the absorbance of a surface have a part to play in increasing optical absorption. It is proposed that further development of work done here would create a surface which has a high roughness and incorporates the absorbing properties of surface oxides such as cuprite. In addition to this, further investigation of the oxides formed during laser processing, using XPS would give a clearer view of the mechanisms in action. With a high thermal heat capacity, copper is already used in commercial solar thermal applications. One development which could be pursued as a direct continuation of this project is the laser processing of copper in two gaseous environments. If a sample is first processed in argon to develop high surface roughness and subsequently processed in air to form an absorbent oxide layer it is believed that almost total absorption of incident light will occur. In a world which is slowly being weaned off non-renewable energy solutions, such as fossil fuels, the development of new technologies to improve the generation of energy from freely available energy sources are important. This project has touched upon the generation of

thermal energy using laser processed surfaces for the conversion of solar radiation into heat. Development of these ideas has already begun but integration of these optically absorbent surfaces into current technological solutions needs to be completed.

REFERENCES

1. J.F.V. Vincent, D.L.M., *Systematic technology transfer from biology to engineering*. Phil. Trans. R. Soc. Lond. A, 2002. **360**: p. 159-173.
2. Baeyer, H.C.V., *The lotus effect*. The Sciences: Journal of the New York Academy of Sciences, 2000: p. 12-15.
3. Ball, P., *Life's lessons in design*. Nature, 2001. **409**(6818): p. 413-416.
4. Barthlott, W. and C. Neinhuis, *Purity of the sacred lotus, or escape from contamination in biological surfaces*. Planta, 1997. **202**(1): p. 1-8.
5. Neinhuis, C. and W. Barthlott, *Characterization and Distribution of Water-repellent, Self-cleaning Plant Surfaces*. Annals of Botany, 1997. **79**(6): p. 667-677.
6. Hirota, K., Y. Tsukiyama, and T. Yasuumi, *Precision blanking of thin sheet metals with the help of chemical etching*. Journal of Materials Processing Technology, 2008. **201**(1-3): p. 209-213.
7. Coulson, S.R., et al., *Super-Repellent Composite Fluoropolymer Surfaces*. The Journal of Physical Chemistry B, 2000. **104**(37): p. 8836-8840.
8. Chen, W., et al., *Ultrahydrophobic and Ultralyophobic Surfaces:â€™ Some Comments and Examples*. Langmuir, 1999. **15**(10): p. 3395-3399.
9. Bico, J. and et al., *Pearl drops*. EPL (Europhysics Letters), 1999. **47**(2): p. 220.
10. Maiman, T.H., *Stimulated Optical Radiation in Ruby*. Nature, 1960. **187**(4736).
11. Steen, W.M., *Laser material processing*. 2003: Springer-Verlag London.
12. Daniel, C., F. Mücklich, and Z. Liu, *Periodical micro-nano-structuring of metallic surfaces by interfering laser beams*. Applied Surface Science, 2003. **208-209**: p. 317-321.
13. Gower, M.C., *Industrial Applications of Pulsed Lasers to Materials Microprocessing*. SPIE Vol., 1998.
14. Dyer, P.E., S.D. Jenkins, and J. Sidhu, *Development and origin of conical structures on XeCl laser ablated polyimide*. Applied Physics Letters, 1986. **49**(8): p. 453-455.
15. Guosheng, Z., P.M. Fauchet, and A.E. Siegman, *Growth of spontaneous periodic surface structures on solids during laser illumination*. Physical Review B, 1982. **26**(10): p. 5366.

-
16. Bensaoula, A., et al., *Arrays of 3D micro-columns generated by laser ablation of Ta and steel: modelling of a black body emitter*. Applied Physics A: Materials Science & Processing, 2004. **79**(4): p. 973-975.
 17. Dolgaev, S.I., et al., *Formation of conical microstructures upon laser evaporation of solids*. Applied Physics A: Materials Science & Processing, 2001. **73**(2): p. 177-181.
 18. Borowiec, A. and H.K. Haugen, *Subwavelength ripple formation on the surfaces of compound semiconductors irradiated with femtosecond laser pulses*. Applied Physics Letters, 2003. **82**(25): p. 4462-4464.
 19. Tan, B. and K. Venkatakrishnan, *A femtosecond laser-induced periodical surface structure on crystalline silicon*. Journal of Micromechanics and Microengineering, 2006. **16**(5): p. 1080-1085.
 20. Milonni, P.W. and J.H. Eberly, *Lasers*. 1988: Wiley.
 21. Silfvast, W.T., *Laser fundamentals*. 1996, Cambridge: Cambridge University Press. 521.
 22. Rizvi, N.H., *Femtosecond Laser Micromachining: Current Status and Applications*. RIKEN Review, 2003. **50**: p. 107.
 23. Momma, C., et al., *Short-pulse laser ablation of solid targets*. Optics Communications, 1996. **129**(1-2): p. 134-142.
 24. Ameer-Beg, S., et al., *Femtosecond laser microstructuring of materials*. Applied Surface Science, 1998. **129**: p. 875-880.
 25. Ferreira, P., *General relativity: Gravitational waves*, in *New Scientist*. 2010.
 26. McEvoy, J.P. and O. Zarate, *Introducing Quantum Theory*. 1999, London: Icon Books
 27. *The Penguin Dictionary of Physics*. 2000, London: Market House Books Ltd.
 28. Krane, K., *Modern Physics*. 1996: John Wiley & Sons, Inc. .
 29. Einstein, A., *On the Quantum Theory of Radiation*. Journal of Physics Z, 1917: p. 121 - 128.
 30. J.Wilson and J.F.B. Hawkes, *Laser - Principles and Applications*. 1987, London: Prentice Hall.
 31. Einstein, A., *On the Quantum Theory of Radiation*. Journal of Physics Z, 1917: p. 121-128.
-

-
32. Saleh, B.E.A. and M.C. Teich, *Fundamentals of Photonics*. 1991, New York: John Wiley & Sons.
 33. Ready, J.F., *Industrial applications of lasers*. 1978, LONDON: Academic Press limited.
 34. Siegman, A.E., *Laser beams and resonators: Beyond the 1960s*. Selected Topics in Quantum Electronics, IEEE Journal of, 2000. **6**(6): p. 1389-1399.
 35. Duffin, W.J., *Electricity and Magnetism*. 1990, London: McGraw-Hill.
 36. Hecht, E. and A. Zajac, *Optics / Eugene Hecht, with contributions by Alfred Zajac*. 1987, Reading, Mass. :: Addison-Wesley Pub. Co.
 37. Hecht, J., *The laser Guidebook*, ed. S. Edition. 1992, New York: McGraw-Hill.
 38. Li, A.G.F.a.T., *Resonant modes in an optical maser*. Bell Syst. Tech. J., 1961. **40**: p. 453.
 39. Kogelnik, H. and T. Li, *Laser Beams and Resonators*. Appl. Opt., 1966. **5**(10): p. 1550-1567.
 40. CVI and Melles-Griot, *All Things photonic (The CVI Melles Griot Technical Guide)*. Vol. 2.
 41. Ion, J.C., *Laser Processing of Engineering Materials*. 2005, Oxford: Elsevier Butterworth-Heinemann.
 42. 11146, I.S., *Lasers and laser-related equipment – Test methods for laser beam widths, divergence angles and beam propagation ratios*. 2005.
 43. Greivenkamp, J.E., *Field Guide to Geometrical Optics*. SPIE Field Guides, ed. J.E. Greivenkamp. 2004, Washington: SPIE - The International Society for Optical Engineering.
 44. M.Bass, *Handbook of Optics*. Vol. 1/2. 1995, United States: McGRAW-HILL.
 45. *Advances in laser materials processing technology: Technology, research and application*, ed. J.P. J Lawrence, D K Y Low, E Toyserkani. 2010, Cambridge: Woodhead Publishing Limited.
 46. Dyer, P.E., *Excimer laser polymer ablation: twenty years on*. Applied Physics A: Materials Science & Processing, 2003. **77**(2): p. 167-173.
 47. I.W. Boyd and R.B. Jackman, *Photochemical processing of electronic materials*. 1992, London: Academic Press. 532.
 48. D. Bäuerle, *Laser Processing and Chemistry*. 3rd ed. 2000, Berlin: Springer.
-

-
49. Srinivasan, R., E. Sutcliffe, and B. Braren, *Ablation and Etching of Polymethylmethacrylate by Very Short (160 Fs) Ultraviolet (308 nm) Laser Pulses*. Applied Physics Letters, 1987. **51**(16): p. 1285-1287.
 50. J.E. Andrew, et al., Appl. Phys. Lett, 1983. **43**(8): p. 717-719.
 51. Dyer, P.E. and J. Sidhu, *Excimer laser ablation and thermal coupling efficiency to polymer films*. Journal of Applied Physics, 1985. **57**(4): p. 1420-1422.
 52. Dyer, P.E., *Laser Ablation of Polymers, in Photchemical Processing of Electronic Materials*, ed. I.W. Boyd, Jackman, R. B. 1992, London: Academic.
 53. Sutcliffe, E. and R. Srinivasan, *Dynamics of Uv Laser Ablation of Organic Polymer Surfaces*. Journal of Applied Physics, 1986. **60**(9): p. 3315-3322.
 54. Koren, G., *Temporal Measurements of Photofragment Attenuation at 248 Nm in the Laser Ablation of Polyimide in Air*. Applied Physics Letters, 1987. **50**(16): p. 1030-1032.
 55. A. Latif, M.S.A., M.A. Aleem, M.S. Rafique and M. Khaleeq-Ur-Rahman *Influence of number of laser shots on laser induced microstructures on Ag and Cu targets*. . Laser Particles and Beams, 2009. **27**: p. 129-136.
 56. Dolgaev, S.I., et al., *Growth of large microcones in steel under multipulsed Nd:YAG laser irradiation*. Applied Physics A: Materials Science & Processing, 2006. **83**(3): p. 417-420.
 57. Dolgaev, S.I., et al., *Laser-assisted growth of microstructures on spatially confined substrates*. Applied Surface Science, 2007. **253**(19): p. 7987-7991.
 58. Kazakevich, P.V., A.V. Simakin, and G.A. Shafeev, *Formation of periodic structures by laser ablation of metals in liquids*. Applied Surface Science, 2006. **252**(13): p. 4457-4461.
 59. Gedvilas, M., G. Račiukaitis, and K. Regelskis, *Self-organization in a chromium thin film under laser irradiation*. Applied Physics A: Materials Science & Processing, 2008. **93**(1): p. 203-208.
 60. Murthy, N.S., et al., *Self-assembled and etched cones on laser ablated polymer surfaces*. Journal of Applied Physics, 2006. **100**(2): p. 023538-12.
 61. Barnier, F., et al., *Fibre optic jacket removal by pulsed laser ablation*. Journal of Physics D-Applied Physics, 2000. **33**(7): p. 757-759.
 62. Dyer, P.E. and R.J. Farley, *Periodic Surface-Structures in the Excimer Laser Ablative Etching of Polymers*. Applied Physics Letters, 1990. **57**(8): p. 765-767.
-

-
63. Lazare, S. and V. Granier, *Ultraviolet-Laser Photoablation of Polymers - a Review and Recent Results*. Laser Chemistry, 1989. **10**(1): p. 25-40.
 64. Lippert, T., *Laser application of polymers*. Polymers and Light, 2004. **168**: p. 51-246.
 65. Dyer, P.E., S.D. Jenkins, and J. Sidhu, *Novel Method for Measuring Excimer Laser Ablation Thresholds of Polymers*. Applied Physics Letters, 1988. **52**(22): p. 1880-1882.
 66. Koynov, S., M.S. Brandt, and M. Stutzmann, *Black nonreflecting silicon surfaces for solar cells*. Applied Physics Letters, 2006. **88**(20): p. 203107-3.
 67. B.G.I. Dance, A.L.B., *Surfi-Sculpt A New Electron Beam Processing Technology*, in *8th International Conference on Electron Beam technologies*. 2006: Varna.
 68. Bekesi, J., et al., *Fabrication of large-area grating structures through laser ablation*. Applied Physics A: Materials Science & Processing, 2008. **93**(1): p. 27-31.
 69. Li, X. and et al., *Fabrication of a two-dimensional periodic microflower array by three interfered femtosecond laser pulses on Al:ZnO thin films*. New Journal of Physics. **12**(4): p. 043025.
 70. Dyer, P.E., J. Mackay, and C.D. Walton, *Diffraction modelling of laser ablation using transmission masks*. Optics Communications, 2004. **240**(4-6): p. 391-399.
 71. P.E. Dyer, S.M.M., C.D. Walton, M. Ersoz, P.D.I. Fletcher, V.N. Paunov, Appl. Phys. A 2003. **77**: p. 391-394.
 72. Hirano, M., K.-i. Kawamura, and H. Hosono, *Encoding of holographic grating and periodic nano-structure by femtosecond laser pulse*. Applied Surface Science, 2002. **197-198**: p. 688-698.
 73. Klein-Wiele, J.-H. and P. Simon, *Fabrication of periodic nanostructures by phase-controlled multiple-beam interference*. Applied Physics Letters, 2003. **83**(23): p. 4707-4709.
 74. M. Hirano, K., Kawamura, H. Hosono, Appl. Surf. Sci 2002. **197-198**: p. 688-698.
 75. Costache, F., M. Henyk, and J. Reif, *Surface patterning on insulators upon femtosecond laser ablation*. Applied Surface Science, 2003. **208-209**: p. 486-491.
 76. Groenendijk, M. and J. Meijer, *Microstructuring using femtosecond pulsed laser ablation*. Journal of Laser Applications, 2006. **18**(3): p. 227-235.
-

-
77. Nayak, B.K. and M.C. Gupta, *Self-organized micro/nano structures in metal surfaces by ultrafast laser irradiation*. Optics and Lasers in Engineering, **48**(10): p. 940-949.
 78. Nayak, B.K. and M.C. Gupta, *Ultrafast laser-induced self-organized conical micro/nano surface structures and their origin*. Optics and Lasers in Engineering, **48**(10): p. 966-973.
 79. Sipe, J.E., et al., *Laser-induced periodic surface structure. I. Theory*. Physical Review B, 1983. **27**(2): p. 1141.
 80. Hsu, E.M., et al., *Periodic surface structures on gallium phosphide after irradiation with 150 fs--7 ns laser pulses at 800 nm*. Applied Physics Letters, 2007. **91**(11): p. 111102-3.
 81. Bolle, M., et al., *Submicron Periodic Structures Produced on Polymer Surfaces with Polarized Excimer Laser Ultraviolet-Radiation*. Applied Physics Letters, 1992. **60**(6): p. 674-676.
 82. Clark, S.E. and D.C. Emmony, *Ultraviolet-Laser-Induced Periodic Surface-Structures*. Physical Review B, 1989. **40**(4): p. 2031-2041.
 83. Clark, S.E., N.C. Kerr, and D.C. Emmony, *Anomalous Laser-Induced Periodic Surface-Structures*. Journal of Physics D-Applied Physics, 1989. **22**(4): p. 527-534.
 84. Wagner, R., et al., *Subwavelength ripple formation induced by tightly focused femtosecond laser radiation*. Applied Surface Science, 2006. **252**(24): p. 8576-8579.
 85. WYKO, *Surface Profilers Technical Reference Manual*. P/N 980-085. 1999, United States of America: Veeco Metrology Group.
 86. Hesse, M., M. Meier, and B. Zeeh, *Spectroscopic Methods in Organic Chemistry*. 1997, Georg Thieme Verlag Stuttgart: New York.
 87. Azároff, L.V.R.K., N. Kato, R. J. Weiss, A. J. C. Wilson, R. A. Young, *X-ray Diffraction*. 1974: McGraw-Hill.
 88. *Small Angle X-ray Scattering*, ed. K.O. Glatter O. 1982: Academic Press.
 89. Vorobyev, A.Y. and C. Guo, *Enhanced absorptance of gold following multipulse femtosecond laser ablation*. Physical Review B, 2005. **72**(19): p. 195422.
 90. Vorobyev, A.Y. and C. Guo, *Femtosecond laser structuring of titanium implants*. Applied Surface Science, 2007. **253**(17): p. 7272-7280.
-

-
91. Lazic, V., et al., *Efficient plasma and bubble generation underwater by an optimized laser excitation and its application for liquid analyses by laser-induced breakdown spectroscopy*. Spectrochimica Acta Part B: Atomic Spectroscopy, 2007. **62**(12): p. 1433-1442.
 92. Cabalín, L.M. and J.J. Laserna, *Experimental determination of laser induced breakdown thresholds of metals under nanosecond Q-switched laser operation*. Spectrochimica Acta Part B: Atomic Spectroscopy, 1998. **53**(5): p. 723-730.
 93. Momma, C., et al., *Short-pulse laser ablation of solid targets*. Optics Communications, 1996. **129**(1-2): p. 134-142.
 94. Brailovsky, A.B., S.V. Gaponov, and V.I. Luchin, *Mechanisms of melt droplets and solid-particle ejection from a target surface by pulsed laser action*. Applied Physics A: Materials Science & Processing, 1995. **61**(1): p. 81-86.
 95. Dunning-Davies, J., *Mathematical Methods for Mathematicians, Physical Scientists and Engineers*. 2003, Chichester, UK: Horwood.
 96. J. H. Lienhard IV, J.H.L.V., *A Heat Transfer Textbook*. 3 ed. 2002, Cambridge, U.S.A: Phlogiston Press.
 97. Young, T., *An Essay on the Cohesion of Fluids*. Philosophical Transactions of the Royal Society of London, 1805. **95**: p. 65-87.
 98. Girifalco, L.A. and R.J. Good, *A Theory for the Estimation of Surface and Interfacial Energies. I. Derivation and Application to Interfacial Tension*. The Journal of Physical Chemistry, 1957. **61**(7): p. 904-909.
 99. Nakajima, A., K. Hashimoto, and T. Watanabe, *Recent Studies on Super-Hydrophobic Films*. Monatshefte für Chemie / Chemical Monthly, 2001. **132**(1): p. 31-41.
 100. Nishino, T., et al., *The Lowest Surface Free Energy Based on $\hat{a}^{\sim}CF_3$ Alignment*. Langmuir, 1999. **15**(13): p. 4321-4323.
 101. Wenzel, R.N., *RESISTANCE OF SOLID SURFACES TO WETTING BY WATER*. Industrial & Engineering Chemistry, 1936. **28**(8): p. 988-994.
 102. Cassie, A.B.D. and S. Baxter, *Wettability of porous surfaces*. Transactions of the Faraday Society, 1944. **40**: p. 546-551.
 103. Patankar, N.A., *On the Modeling of Hydrophobic Contact Angles on Rough Surfaces*. Langmuir, 2003. **19**(4): p. 1249-1253.
 104. Liu, B. and F.F. Lange, *Pressure induced transition between superhydrophobic states: Configuration diagrams and effect of surface feature size*. Journal of Colloid and Interface Science, 2006. **298**(2): p. 899-909.
-

-
105. Onda, T., et al., *Super-Water-Repellent Fractal Surfaces*. Langmuir, 1996. **12**(9): p. 2125-2127.
106. R. E. Johnson Jr., R.H.D., *Contact Angle, Wettability and Adhesion*, in *Advances in Chemistry series*, F.M. Fowkes, Editor. 1964, American Chemical Society, Washington D. C. p. 112–135.
107. Neinhuis, C. and W. Barthlott, *Characterization and Distribution of Water-repellent, Self-cleaning Plant Surfaces*. Ann Bot, 1997. **79**(6): p. 667-677.
108. A. Latif, M.S.A., M.A. Aleem, M.S. Rafique and M. Khaleeq-Ur-Rahman *Influence of number of laser shots on laser induced microstructures on Ag and Cu targets. Laser and Particle Beams*, 27, pp 129-136 doi:10.1017/S0263034609000196 Laser Particles and Beams, 2009. **27**: p. 129-136.
109. Lafuma, A. and D. Quere, *Superhydrophobic states*. Nat Mater, 2003. **2**(7): p. 457-460.
110. Cheng, Y.-T. and D.E. Rodak, *Is the lotus leaf superhydrophobic?* Applied Physics Letters, 2005. **86**(14): p. 144101-3.
111. Morra, M., E. Occhiello, and F. Garbassi, *Contact angle hysteresis in oxygen plasma treated poly(tetrafluoroethylene)*. Langmuir, 1989. **5**(3): p. 872-876.
112. Wu, Y., et al., *Characteristics of ultra water-repellent thin films prepared by combined process of microwave plasma-enhanced CVD and oxygen-plasma treatment*. Thin Solid Films, 2002. **407**(1-2): p. 45-49.
113. Bartell FE, S.J., J Phys Chem, 1953. **57**.
114. Kubiak, K.J., et al., *Wettability versus roughness of engineering surfaces*. Wear. **In Press, Corrected Proof**.
115. Lewington, T.A., et al., *bodycote International Prize Paper Competition: Shortlisted Characterisation of Alkyl Phosphonic Acid Monolayers Self Assembled on Hydrated Surface of Aluminium*. Surface Engineering, 2002. **18**: p. 228-232.
116. Catalin, F., C. James, and R.A. Morgan, *Characterisation of the surface chemistry of magnesium exposed to the ambient atmosphere*. Surface and Interface Analysis, 2006. **38**(10): p. 1363-1371.
117. Kietzig, A.-M., S.G. Hatzikiriakos, and P. Englezos, *Patterned Superhydrophobic Metallic Surfaces*. Langmuir, 2009. **25**(8): p. 4821-4827.
118. Zhang, C.-l., et al., *Studies on the decomposition of carbon dioxide into carbon with oxygen-deficient magnetite: I. Preparation, characterization of magnetite*,
-

-
- and its activity of decomposing carbon dioxide*. Materials Chemistry and Physics, 2000. **62**(1): p. 44-51.
119. Abdolvand, A., et al., *Formation of highly organised, periodic microstructures on steel surfaces upon pulsed laser irradiation*. Applied Physics A: Materials Science & Processing, 2009. **95**(2): p. 447-452.
120. Lloyd, R., et al., *Laser-assisted generation of self-assembled microstructures on stainless steel*. Applied Physics A: Materials Science & Processing, 2008. **93**(1): p. 117-122.
121. Wu, C., et al., *Near-unity below-band-gap absorption by microstructured silicon*. Applied Physics Letters, 2001. **78**(13): p. 1850-1852.
122. Park, H.K., C.P. Grigoropoulos, and A.C. Tam, *OPTICAL MEASUREMENTS OF THERMAL-DIFFUSIVITY OF A MATERIAL*. International Journal of Thermophysics, 1995. **16**(4): p. 973-995.
123. Bertolotti, M., et al., *Analysis of the photothermal deflection technique in the surface reflection scheme: Theory and experiment*. Journal of Applied Physics, 1998. **83**(2): p. 966-982.
124. Whitehead, D.J., et al., *Monitoring laser cleaning of titanium alloys by probe beam reflection and emission spectroscopy*. Applied Physics A-Materials Science & Processing, 2008. **93**(1): p. 123-127.
125. Wu, B., et al., *Superhydrophobic surfaces fabricated by microstructuring of stainless steel using a femtosecond laser*. Applied Surface Science, 2009. **256**(1): p. 61-66.

APPENDIX A: PUBLICATIONS

To date two publications have been produced from work carried out for this PhD. They are given here in their published format.

A1: *Laser-assisted generation of self-assembled microstructures on stainless steel.*

R. Lloyd, A. Abdolvand, M. Schmidt, P. Crouse, D. J. Whitehead, Z. Liu, L. Li

Applied Physics A: Materials Science & Processing, 2008. **93**(1): p. 117-122.

A2: *Formation of highly organised, periodic microstructures on steel surfaces upon pulsed laser irradiation.*

A. Abdolvand, R. Lloyd, M. Schmidt, D. J. Whitehead, Z. Liu, L. Li.

Applied Physics A: Materials Science & Processing, 2009. **95**(2): p. 447-452.

Laser-assisted generation of self-assembled microstructures on stainless steel

Robert Lloyd · Amin Abdolvand · Marc Schmidt · Philip Crouse · David Whitehead · Zhu Liu · Lin Li

Received: 12 October 2007 / Accepted: 4 March 2008 / Published online: 31 May 2008
© Springer-Verlag 2008

Abstract Utilising a Nd:YVO₄ laser (wavelength of 532 nm, pulse duration of 8 ns, repetition rate of 30 kHz) and a Nd:YAG laser (wavelength of 1064 nm, pulse duration of 7 ns, repetition rate of 25 kHz), it was found that during the pulsed laser ablation of metal targets, such as stainless steel, periodic nodular microstructures (microcones) with average periods ranging from ~30 to ~50 µm were formed. This period depends on the number of accumulated laser pulses and is independent of the laser wavelength. It was found that the formation of microcones could occur after as little as 1500 pulses/spot (a lower number than previously reported) are fired onto a target surface location at laser fluence of ~12 J/cm², intensity of ~1.5 GW/cm². The initial feedback mechanism required for the formation of structures is attributed to the hydrodynamic instabilities of the melt. In addition to this, it has been shown that the structures grow along the optical axis of the incoming laser radiation. We demonstrate that highly regular structures can be produced at various angles, something not satisfactorily presented on metallic surfaces previously. The affecting factors such as incident angle of the laser beam and the structures that can be formed when varying the manner in which the

laser beam is scanned over the target surface have also been investigated.

PACS 42.55.Xi · 61.66.Dk · 81.65.Cf

1 Introduction

The use of lasers for the direct writing of microfeatures is common practice in the field of materials processing [1–14]. The formation of laser-induced surface structures with a period approximately equal to the laser wavelength is well understood [5, 6]. However, the use of lasers to produce self-assembled structures is a less exploited area, and the mechanisms responsible for their growth are still under discussion. The microstructures developed under multi-pulse laser irradiation have usually a somewhat higher period (typically tens of micrometers) [7]. Microstructures have been observed in many materials under inert and reactive ambient gases, with laser wavelengths from UV to IR and laser pulse durations from nanosecond to femtosecond. In some cases, such as pulsed laser deposition of thin films they appear at the bottom of craters after laser ablation processes. In other cases, they grow from the surface of the target, e.g. in surface modification treatment at various laser fluences. The latter results from the melting of a surface layer and a low vapourisation rate depending on the intensity of the source and number of accumulated pulses. Over the past several years, there have been several reports of laser generated self-assembled structures on metals [9–12], semiconductors [8–11], and polymers [13, 14]. Unlike conical structures that have been reported on laser machined polymer surfaces, the process by which microcones and alike are produced on a metallic substrates is a melt flow dominated process rather than vaporisation–redeposition process [8–10]. Previous results

R. Lloyd (✉) · A. Abdolvand · M. Schmidt · P. Crouse · D. Whitehead · L. Li
Laser Processing Research Centre, School of Mechanical, Aerospace and Civil Engineering, The University of Manchester, Manchester M60 1QD, UK
e-mail: robert.lloyd@postgrad.manchester.ac.uk

A. Abdolvand
e-mail: amin.abdolvand@manchester.ac.uk

R. Lloyd · Z. Liu
Corrosion and Protection Centre, School of Materials, The University of Manchester, Manchester M60 1QD, UK

have shown that when a large number of laser pulses (10^5) at laser intensities in the order of 10^6 W/cm² are delivered to metal targets, self-assembled arrays of microstructures, with a period of ~ 70 μm , can be formed [8, 9]. This value was much smaller than the laser spot size of ~ 300 μm used for these experiments, and was also far from the initial capillary wave period. Initial impetus for this work came from similar studies of structure formation in liquid environments [10].

This paper intends to show a methodical approach to the different types of structures that can be produced by firing relatively large numbers of pulses (10^2 – 10^4 pulses) at metallic targets, specifically stainless steel. We show that at high laser intensities, in the order of $\sim 1.5 \times 10^9$ W/cm² and after as little as 1500 pulse/spot are fired onto the target, regular microstructures can be formed. The formations of these structures are attributed to the hydrodynamic instabilities of the melt produced on the surface during laser heating. It is also reported that the axis of the self-assembled structures are oriented along the direction of the laser beam. It results in the formation of highly regular structures at various angles on the metal surface owing to the good beam quality of the source. This has been shown to some degree in [7], where silicon microcones were produced by laser machining in an SF₆ environment. As formation of microstructures is not exclusively produced in exotic gas environments, it would seem reasonable that they could be produced in an air environment. The production of such features is believed to have applications as black body sources [15], and in the fields of surface wettability, and microbiology.

2 Experimental details

For the first set of experiments, a Nd:YVO₄ laser system ($\lambda = 532$ nm, $\tau = 8$ ns, with a repetition rate of 30 kHz) was used to process Stainless Steel (AISI 304) samples in air environments (at room temperature and normal atmospheric pressure). The laser beam with a near Gaussian intensity distribution ($M^2 \sim 1.5$) was focused onto the surface with spot diameter of ~ 50 μm . For these experiments laser fluence of ~ 12 J/cm², intensity of ~ 1.5 GW/cm², was used. The laser beam was raster scanned over the surface of the target using a computer controlled galvo-scanning system equipped with a flat field lens. The hatch distance, the distance between adjacent raster scans, was 25 μm resulting in $\sim 50\%$ beam overlap between consecutive scans. Due to the laser repetition rate and the scan velocity multiple passes were required in order that the desired number of pulses at each spot on the target surface were achieved. The dependence of structure formation on the total number of pulses fired at the target was investigated by changing the number of passes from one (1500 pulses/spot) to seven (10500 pulses/spot).

For the next set of experiments Nd:YAG laser system ($\lambda = 1064$ nm, $\tau = 7$ ns, with a repetition rate of

25 kHz) was used. Once again the laser beam with a near Gaussian intensity distribution ($M^2 \sim 1.5$) was focused onto the surface with spot diameter of ~ 50 μm . For these experiments only a laser fluence of ~ 3 J/cm², intensity of ~ 0.43 GW/cm², was used to process the samples in air environments (at room temperature and normal atmospheric pressure). It has been noted that the structures are formed aligned towards the incoming laser beam. Although it has been previously indicated, a systematic study to produce microstructures, which are aligned with the laser beam, on metallic surface does not seem to have been reported. It was calculated that the depth of focus, the distance either side of the beam waist over which the beam diameter grows by 5%, at a wavelength of 1064 nm was $\sim \pm 400$ μm . This allowed the target to be tilted so that processing could take place within a regime where the laser beam parameters would stay relatively uniform. Three incident angles of 75, 60, and 45 degrees were used. These structures were processed in both the parallel line scanning and the cross hatching regimes. The target was processed so that ~ 2500 pulses were fired at a single target site in the line scanning regime, and hence 5000 pulses were fired per spot in the cross hatching regime.

3 Results and discussion

Raster scanning of a 532 nm laser beam over a stainless steel target produced the microstructures that can be seen in Fig. 1e. This occurred after ~ 10500 pulses had been applied per spot. Here, the period of the microstructures, measured as the average separation between tips, is ~ 50 μm , close to the laser spot size on the target. It was not mentioned in previous reports, that it is possible to produce these structures by applying as few as 1500 pulses/spot, as can be seen in Fig. 1d. It was found that an increase in the number of pulses per spot, from 1500 to 10500 (Fig. 1a, b, c, and d), results in the increase of the period of the microstructure, from ~ 30 μm to ~ 50 μm , respectively, with intermediate values being ~ 34 μm for 4500 pulses/spot (Fig. 1c), and ~ 41 μm for 7500 pulses/spot (Fig. 1b). This affects the number density of the structures. The number density of the cones decreases as the number of pulses fired per spot increases. Thus, the increase in the period of the microstructures suggests the growth of some cones at the expense of others. It can be seen from Fig. 2 that as the number of pulses applied to a target surface are increased, the period of the microstructure increases in a parabolic manner. This would suggest that there will be a practical limit to the period of the microstructure. After this point, only ablation of the surface would take place and the structures would appear further below the original surface. It was also observed that when the number of pulses per spot is kept constant the

Fig. 1 Scanning electron microscopy (SEM) images (view tilt 45°) of the target sites where the number of pulses per spot, N_T , have been changed (laser wavelength 532 nm, intensity 1.5 GW/cm^2 , beam spot diameter $\sim 50 \mu\text{m}$, distance between the subsequent lines $\sim 25 \mu\text{m}$). From top to bottom, N_T is (a) 10500, (b) 7500, (c) 4500, and (d) 1500, with average tip-to-tip distance of $\sim 50, 41, 35$, and $30 \mu\text{m}$, respectively. Inset (e)—view tilt 75° is the enlarged part of the Fig. 1a. Exposed areas look like black regions on a bright steel surface

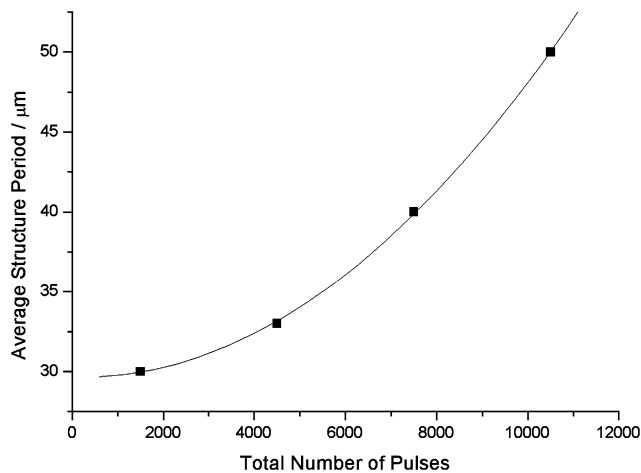
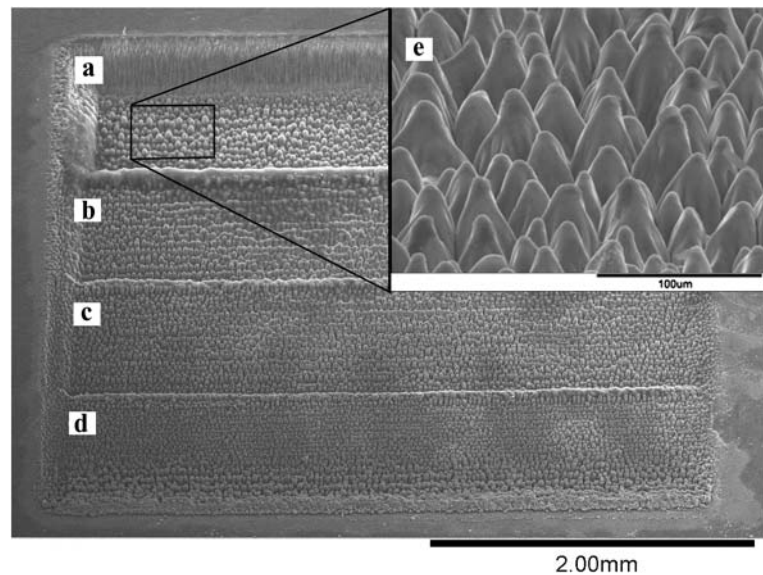


Fig. 2 Graph showing the increase of microstructure period as the total number of pulses fired at the target increases

height of the microcones increases with the laser fluence, while the total number of cones decreases. In the experiment under discussion, the major change that occurs in the surface is the position of the microcones in relation to the original surface. As can be seen from Fig. 1, as more pulses are applied, the structures are formed further below the original surface. This is attributed to the ablation of the material. One may consider evaporation and redeposition of the ablated material as a dominant mechanism since a large number of pulses at high laser fluence are accumulated in this case. However, the smooth surface of the microcones with well-defined apex angle suggests melt displacement as the dominant growth mechanism in these experiments.

It is believed that there are two driving forces behind this material movement. The first of these is the pressure of the expanding ablation products, which are produced at the cen-

tre of the laser beam. Owing to the high intensity and good beam quality of the source, ablation occurs at the centre of the laser beam, which is above the ablation threshold of the material. At the edges of the beam, melting occurs. Interaction of the melt with the pressure in the near-surface plasma layer results in hydrodynamic instabilities of the melt. Development of the instability requires that a large number of laser pulses fired onto the target. It is known that in the absence of definite polarisation of the laser beam and spatial modulation of the radiation intensity (in our case achieved owing to the good beam quality of the source) melt instability in the field of ablation plume pressure results in the growth of large-scale surface structures with a characteristic period of $\sim 20\text{--}30 \mu\text{m}$ [16]. In the range of irradiation parameters here (intensities in the range of $\sim 10^8\text{--}10^{10} \text{ W/cm}^2$, and pulse durations in the range of $<30 \text{ ns}$), formation of these structures is due to a spatial modulation of the pressure in the near-surface plasma layer, followed by melt outflow from pits to humps and subsequent solidification. It is believed that these large-scale surface structures and capillary wave instabilities (aperiodically unstable capillary waves) in the vicinity of plume pressure would act as precursors to the formation of microcones. These waves would alter the reflectivity of the target surface and hence introducing a non-uniform temperature distribution on the target. The non-uniform temperature melt will then give rise to gradients in the surface tension of the molten material. The surface tension of liquids decreases with temperature and they tend to be pulled from hotter regions towards cooler ones. In this case, after initial steps, >1000 pulses/spot and development of the first microcones, more heating occurs at locations that are orientated normal to the incoming laser beam, i.e. the tips of the micro-cones and the inter-cone areas. This results in the general effect that any parts of the surface, which are

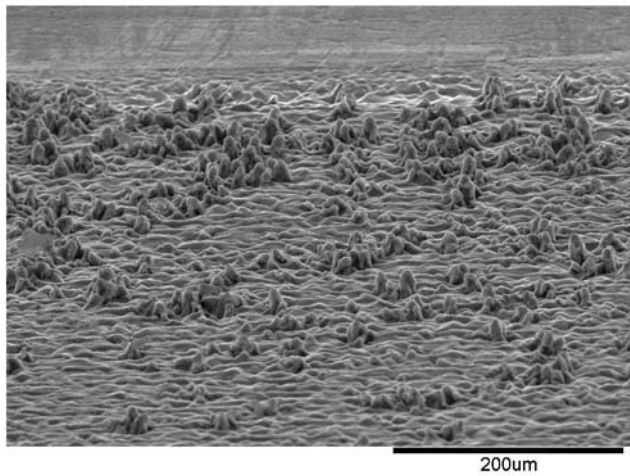


Fig. 3 SEM image (view tilt 75°) of the Stainless Steel surface after only 165 pulses are applied per spot (laser wavelength 532 nm, intensity 1.5 GW/cm², beam spot diameter ~50 μm, distance between the subsequent lines ~25 μm)

not orientated normal to the beam, will be cooler and therefore have a higher surface tension, i.e. the sidewalls of the micro-cones. Due to the small cross-section of the tips they do not absorb much of the laser energy. We can thus conclude that the inter-cone areas acquire the highest temperature due to the fact that they are oriented perpendicular to the laser beam. They are also exposed, and hence absorb the laser irradiation reflected by the sidewalls of the micro-cones. This indicates that the surface tension in these areas has the lowest value on the target material. This results in the development of new structures until a certain number of pulses per spot have been fired onto the target, in our case 1500, and the surface is covered by microcones.

It has to be pointed out that at lower laser fluences the morphology of the surface also evolves with the number of pulses fired onto the target. Figure 3 shows the surface of the target after only 165 pulses/spot are applied laser fluence of 3 J/cm² (intensity of ~0.38 GW/cm²). It can be seen that at the initial stage the structures are formed from the surface relief. It was earlier suggested that capillary waves on the melted target surface are precursors to the formation of three-dimensional periodic structures [17]. Later, a feedback mechanism responsible for the growth of such structures from capillary waves was suggested [8].

So far, the method of scanning the laser beam over the sample had been simple raster scanning. To try and improve the quality of the microstructures that were produced, a cross hatched scanning method was adopted using the Nd:YAG laser system (intensity of ~0.43 GW/cm²). It was noticed that this technique results in the production of highly regular arrays of microfeatures on the surface of a metallic sample. Analysis of further studies of this technique will be the subject of a subsequent paper.

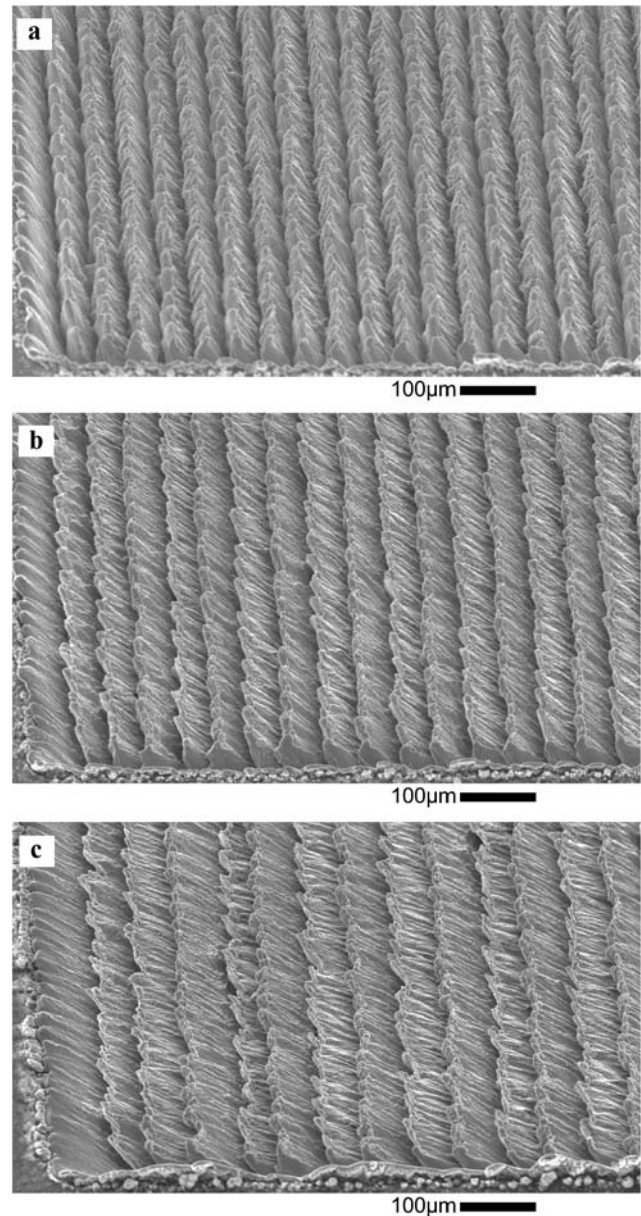


Fig. 4 SEM images (view tilt 30°) of the surface at incident beam angles of (a) 75°, (b) 60°, and (c) 45° using the following parameters: Laser wavelength 1064 nm, intensity 0.43 GW/cm², and 2500 pulses/spot

When a stainless steel target was tilted and processed within the depth of focus of the laser system used, structures were formed (Fig. 4a, b, and c). The incident beam angles in Fig. 4a, b, and c were 75, 60, and 45 degrees, respectively. This gives a good agreement with the final angles of the structures. For this experiment, ~2500 pulses were applied per spot. It was noted that the development of individual structures is slower the shallower the incident angle of the laser beam. This is because the actual area that the focused beam covers increases due to foreshortening at shallower incident angles, thus decreasing the laser fluence.

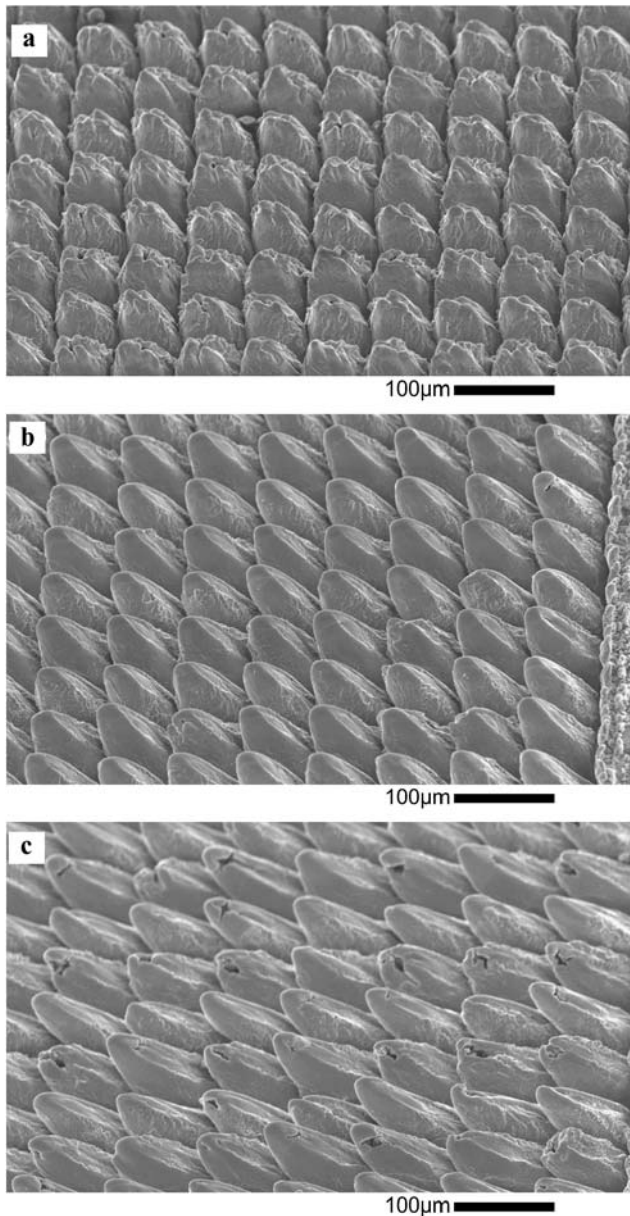


Fig. 5 SEM images (view tilt 30°) of the surface at incident beam angles of (a) 75°, (b) 60°, and (c) 45° using the following parameters: Laser wavelength 1064 nm, intensity 0.43 GW/cm², and 5000 pulses/spot

This is due to the dependence of the laser fluence on the cosine of the incident angle. Eventually, structuring would stop as the fluence at the target drops below that required to effectively process the surface. Applying the cross hatching technique, it is possible to produce the structures shown in Fig. 5a, b, and c. Here, approximately 5000 pulses per spot are fired onto the target. The structures shown were produced at the same incident angles as those in Fig. 4; however, the scanning pattern and hatch distance were varied to produce regular arrays of structures aligned with the incoming laser beam. It can be seen uniform and evenly spaced

microfeatures are produced. In addition to this, the effect of varying the incident beam angle allows the accurate control of structure angles on a micron scale.

4 Conclusion

It is shown that raster-scan multipulse irradiation of steel at 532 and 1064 nm in air produces microcone arrays with spatial periods ranging from 30 to 50 μm, depending on the number of pulses fired onto the target surface for constant intensity. Regular arrays of microcones with average tip-to-tip distances of ~30 μm for 1500 pulses/spot to ~50 μm for 10500 pulses/spot at intensity of 1.5 GW/cm² were produced. The initial feedback mechanism required for the formation of structures is attributed to the hydrodynamic instabilities of the melt.

There are several other outcomes from this work that should be noted if it is desirable to form this type of structure. Firstly, it is not necessary to deposit 10^4 + pulses. Using the correct combination of laser intensity, hatch distance, number of pulses/spot it has been shown that it is possible to produce microstructures by applying as few as 1500–2000 pulses per spot. This greatly decreases the amount of time and effort, which is needed to microstructure a given metallic surface. It was found that the structures produced do align themselves with the incident laser beam; however, the production of such features requires more pulses the further away from the normal incidence.

To avoid the reliance on self-assembly, it is possible to control not only the size but also the arrangement of microstructures by changing the way the laser beam is scanned over the target. Choosing a cross hatching pattern will produce microfeatures between the scan lines. The size and form of these features is largely dependant on the focal spot size of the laser. This will have to be tested from the results and analysis of further studies, and will be the subject of a subsequent paper.

Acknowledgements The Authors would like to thank Teruo Hashimoto for assistance in obtaining some of the SEM images. This work conducted by the Northwest Laser Engineering Consortium (NWLEC) funded by the Northwest Development Agency (NWDA) of the United Kingdom.

References

1. T.J. Bastow, *Nature* **222**, 1058 (1969)
2. J. Heitz, J.D. Pedarnig, D. Bauerle, G. Petzow, *Appl. Phys. A* **65**, 259 (1997)
3. D.J. Krajnovich, J.E. Vazquez, *J. Appl. Phys.* **73**, 3001 (1993)
4. J.F. Silvain, H. Niino, S. Ono, S. Nakaoka, A. Yebe, *Appl. Surf. Sci.* **141**, 25 (1999)
5. J.E. Sipe, J.F. Young, J.S. Preston, H.M. van Driel, *Phys. Rev. B* **27**, 1141 (1983)

6. S.A. Akhmanov, V.I. Emelyanov, N.I. Koroteev, V.N. Seminogov, *Sov. Phys. Usp.* **147**, 674 (1985)
7. S.R. Foltyn, in *Pulsed Laser Deposition of Thin Films*, ed. by D.B. Christy, G.K. Huber (Wiley, New York, 1994)
8. S.I. Dolgaev, S.V. Lavrishev, A.A. Lyalin, A.V. Simakin, V.V. Voronov, G.A. Shafeev, *Appl. Phys. A* **73**, 117 (2000)
9. S.I. Dolgaev, J.M. Fernandez-Pradas, J.L. Morenza, P. Serra, G.A. Shafeev, *Appl. Phys. A* **83**, 417 (2006)
10. P.V. Kazakevich, A.V. Simakin, G.A. Shafeev, *Appl. Surf. Sci.* **252**, 4457 (2006)
11. A. Bensaoula, C. Boney, R. Pillai, G.A. Shafeev, A.V. Simakin, D. Starikov, *Appl. Phys. A* **79**, 973 (2004)
12. S.I. Dolgaev, N.A. Kirichenko, A.V. Simakin, G.A. Shafeev, *Appl. Surf. Sci.* **253**, 7987 (2007)
13. P.E. Dyer, S.D. Jenkins, J. Sidhu, *Appl. Phys. Lett.* **49**, 453 (1986)
14. N.S. Murthy, R.D. Prabhu, J.J. Martin, L. Zhou, R.L. Headrick, *J. Appl. Phys.* **100**, 023538 (2006)
15. D. Starikov, C. Boney, R. Pillai, A. Bensaoula, G.A. Shafeev, A.V. Simakin, *Infrared Phys. Technol.* **45**, 159 (2004)
16. A.B. Brailovsky, A.B. Ezersky, I.A. Dorofeev, V.A. Ermakov, V.I. Luchin, V.E. Semenov, *J. Tech. Phys.* **61**, 129 (1991)
17. S.I. Dolgaev, S.V. Lavrishev, A.A. Lyalin, A.V. Simakin, V.V. Voronov, G.A. Shafeev, *Phys. Vib.* **3**, 231 (1999)

Formation of highly organised, periodic microstructures on steel surfaces upon pulsed laser irradiation

Amin Abdolvand · Robert W. Lloyd ·
Marc J.J. Schmidt · David J. Whitehead · Zhu Liu ·
Lin Li

Received: 21 July 2008 / Accepted: 16 September 2008
© Springer-Verlag 2008

Abstract We present results on the growth of highly organised, reproducible, periodic microstructure arrays on a stainless steel substrate using multi-pulsed Nd:YAG (wavelength of 1064 nm, pulse duration of 7 ns, repetition rate of 25 kHz, beam quality factor of $M^2 \sim 1.5$) laser irradiation in standard atmospheric environment (room temperature and normal pressure) with laser spot diameter of the target being $\sim 50 \mu\text{m}$. The target surface was irradiated at laser fluence of $\sim 2.2 \text{ J/cm}^2$ and intensity of $\sim 0.31 \times 10^9 \text{ W/cm}^2$, resulting in the controllable generation of arrays of microstructures with average periods ranging from ~ 30 to $\sim 70 \mu\text{m}$, depending on the hatching overlap between the consecutive scans. The received tips of the structures were either below or at the level of the original substrate surface, depending on the experimental conditions. The peculiarity of our work is on the utilised approach for scanning the laser beam over the surface. A possible mechanism for the formation of the structures is proposed.

PACS 42.62.-b · 81.65.-b · 52.38.Mf · 81.40.-z

A. Abdolvand (✉) · R.W. Lloyd · M.J.J. Schmidt ·
D.J. Whitehead · L. Li
Laser Processing Research Centre, School of Mechanical,
Aerospace and Civil Engineering, The University of Manchester,
Manchester M60 1QD, UK
e-mail: amin.abdolvand@manchester.ac.uk

R.W. Lloyd · Z. Liu
Corrosion and Protection Centre, School of Materials,
The University of Manchester, Manchester M60 1QD, UK

Present address:
A. Abdolvand
School of Engineering, Physics and Mathematics, University
of Dundee, Dundee DD1 4HN, UK

1 Introduction

Researchers within the laser materials processing community are familiar with the conical and periodic structures that can be produced on various surfaces when the intensity of the laser beam is near or at the damage threshold of the material. An interesting topic in this field is the study of laser-assisted formation of microstructures on material surfaces. Indeed, the formation of microstructures on the surface of metals, ceramics and semiconductors, utilising various pulse laser durations and wavelengths, have been reported [1–6]. In surface modification treatments, where a range of laser fluences lead to melting of a surface layer and a low vaporisation rate, growth of protruding structures (microcones) from the target surface have been observed. In particular, recently, growth of large microcones in steel under multi-pulsed laser irradiation has been reported [7]. In the range of radiation parameters employed by the authors (a pulse duration of $\tau \sim 300 \text{ ns}$ and intensity of $I \sim 10^6 \text{ W/cm}^2$ at 1064 nm line of Nd:YAG laser) the formation of microstructures on metallic surfaces, such as steel, was attributed to the melt flow produced by surface tension gradients resulting from temperature non-uniformity on the surface. The fully developed microcones exhibited an average separation between tips of $\sim 70 \mu\text{m}$, much less than the employed beam spot diameter ($\sim 300 \mu\text{m}$) on the target and far from the surface relief originated by the capillary waves with a period of $\sim 10\text{--}20 \mu\text{m}$. For other materials, such as semiconductors, the effect of vaporisation–redeposition has been used to explain the growth of microstructures, which also exhibited periods much larger than the laser wavelength [8, 9]. Generally, it is common for the microstructures developed under multi-pulse laser irradiation to have periods larger than the laser wavelength [10].

In this paper, we explore experimental conditions required for the formation of highly organised, periodic microstructures on a steel target upon multi-pulsed laser irradiation at 1064 nm in air. The microstructures exhibited an average separation between tips ranging from 30 to 70 μm , depending on the hatching overlap between consecutive scans. The tips of the generated structures are at the level of the original substrate or below, depending on the experimental conditions. To the authors' knowledge, the irradiation parameters employed (pulse duration of $\tau = 7$ ns and intensity of $I \sim 0.3 \times 10^9$ W/cm²) as well as the utilised approach for scanning the laser beam over the sample surface have not been reported before. The fabrication of such organised, periodic and highly reproducible microstructures on metallic surfaces is believed to have applications in the fields of surface wettability modification, and microbiology [11].

2 Experimental

The experiments were performed using stainless steel plates (AISI 304), 1 mm in thickness. The plates were first ultrasonically cleaned with ethanol and deionised water to remove organic contamination. A Nd:YAG laser (Laservall Violino EU Marker) at $\lambda = 1064$ nm, $\tau = 7$ ns and repetition rate of 25 kHz was utilised for irradiation of the samples in standard atmospheric environment (room temperature and normal pressure). The laser beam with a near Gaussian intensity distribution ($M^2 \sim 1.5$) was focused onto the surface. The beam spot diameter on the surface was approximately 50 μm . The depth of focus ($\text{DOF} = \pm 0.08\pi f^2 / M^2 \lambda$) [12], i.e. the distance either side of the beam waist over which the beam diameter grows by 5%, is calculated to be ~ 400 μm . This large DOF results in negligible change of the spot size on the target, providing a uniform ablation trace throughout the experiments.

For these experiments laser fluence of 2.2 J/cm², intensity of $\sim 0.31 \times 10^9$ W/cm², was used. The damage threshold of the material was previously reported to be < 2 J/cm² [13]. The laser beam was raster scanned over the surface of the target at a velocity of 10 mm/s, using a computer controlled galvo-scanner equipped with a flat field lens system. The hatch distance d , i.e. the distance between adjacent raster scans, was varied for each experiment. Essentially, the overlap between consecutive scans was decreased from 40% of the laser spot diameter ($d = 30$ μm), to no overlap ($d = 70$ μm), in steps of 20% ($\Delta d = 10$ μm). Consecutive scans were performed over each area (1 mm²) so that the required number of pulses had accumulated.

Two different scanning regimes were employed for the experiments, namely horizontal line scanning (results shown in Fig. 2) and cross hatched scanning (shown in Fig. 3). In the horizontal line scanning regime (HLSR) the laser was

scanned only in the X-direction (Fig. 2(a)–(e)) and the hatch distance was varied between the lines as described above. In the cross hatching regime (CHR) the laser was scanned over the surface in two directions (X and Y) to form a grid pattern (Fig. 3(a)–(e)), with the total number of pulses fired onto the target surface being twice as many as in the HLSR. The hatch distance was varied in the same manner as for the HLSR in both directions. The surface morphology of the samples was examined using a Hitachi S3400N scanning electron microscope (SEM).

3 Results and discussion

Figure 1 shows the total number of pulses fired per mm² of the target surface versus the hatch distance for both HLSR and CHR. As it can be seen from Fig. 1, the number of pulses decreased as the overlap between consecutive scans was increased. Figure 2 shows the results of the HLSR. Comparing Figs. 2(a) and 2(e) as the extremes provided, it is evident that increasing the hatch distance between the consequent lines, from 30 to 70 μm , and hence decreasing the number of pulses given per area, from ~ 83250 to ~ 35700 , resulted in much lower levels of ablation. Figures 2(c), 2(d) and 2(e) represent the situation where there were no overlaps between the scanned lines. In these pictures, ablation of the material in the scanned path can be clearly seen.

As can be seen in Figs. 2(c), 2(d) and 2(e), some structures have been formed at the edge of the beam. These structures can also be observed in Figs. 2(a) and 2(b) where the distances between the consequent lines are 30 and 40 μm , respectively. It was found that for higher levels of overlap between the lines (< 30 μm) only substantial ablation of the materials occurred with the consequence of no defined structure.

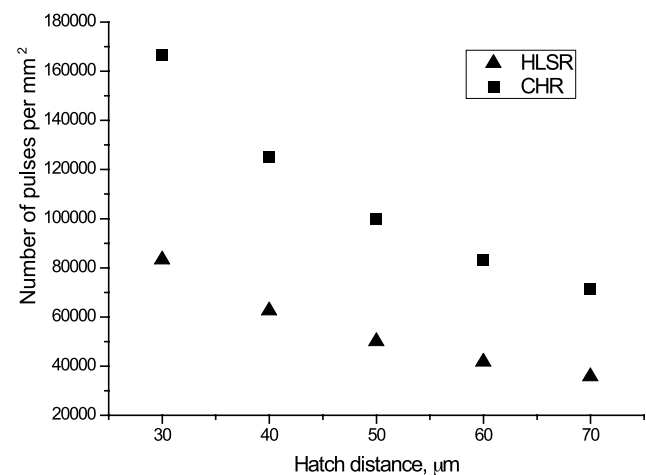


Fig. 1 Graph showing the total number of pulses per mm² fired onto the target surface as a function of the hatch distance for both horizontal line-scanning regime (HLSR) and crossed hatching regime (CHR)

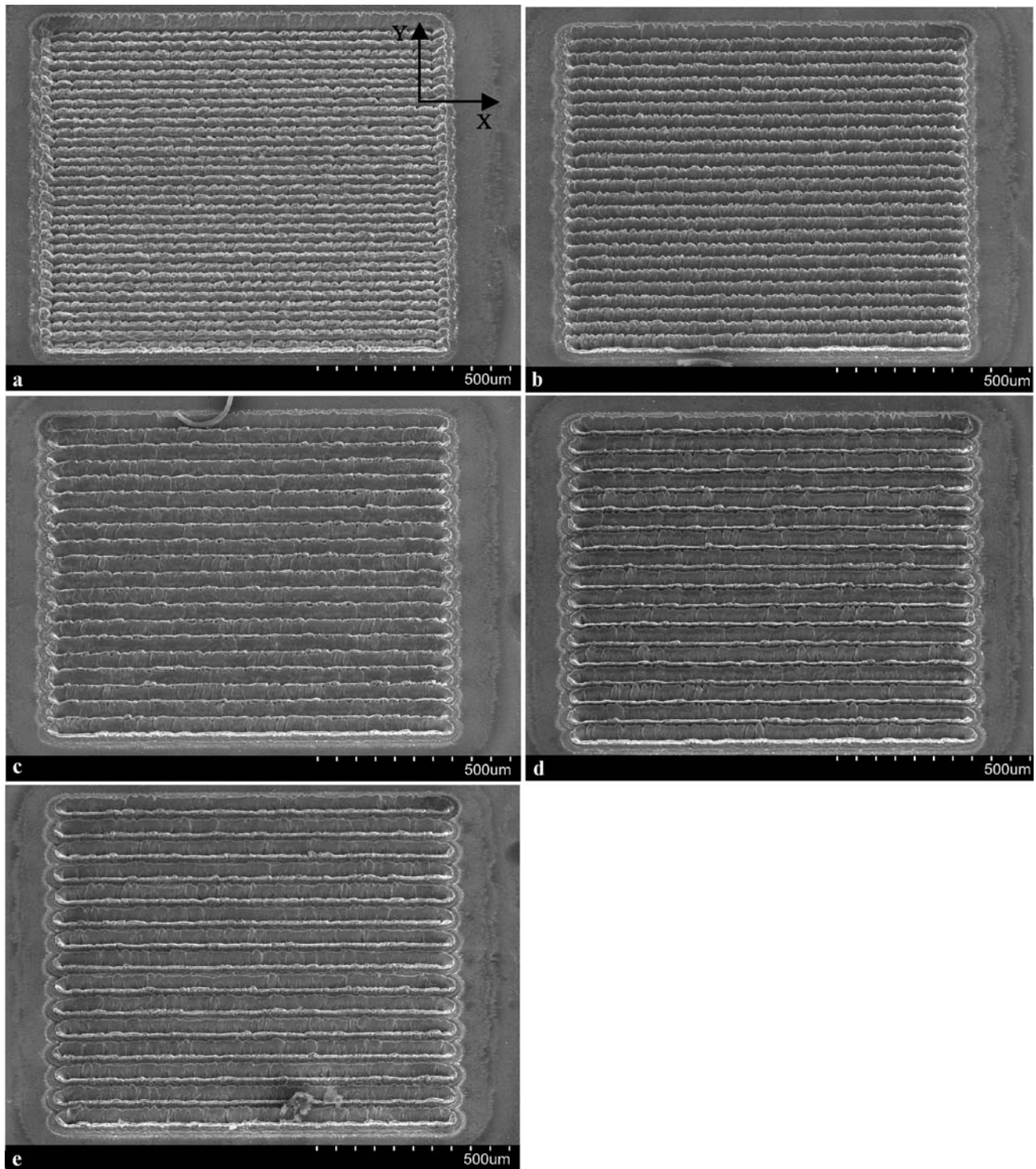


Fig. 2 SEM picture of the steel surface after laser irradiation in the horizontal line-scanning regime (HLSR). The hatch distance was varied between the scanned lines from 30 μm (a)

to 70 μm (e) in steps of 10 μm . The hatch distances are 30, 40, 50, 60, and 70 μm for (a), (b), (c), (d), (e), respectively

Irradiation of the material in CHR resulted in the formation of structures as shown in Fig. 3. These structures appear to be highly organised, as can be identified in Figs. 3(a)–(e), corresponding to the number of pulses per area of between

~ 166500 and ~ 62500 , respectively. Despite the large number of pulses applied, the heights of the structures from Fig. 3(b) onward are always equal to the ablated layer thickness. Here the distance between the consequent scans were

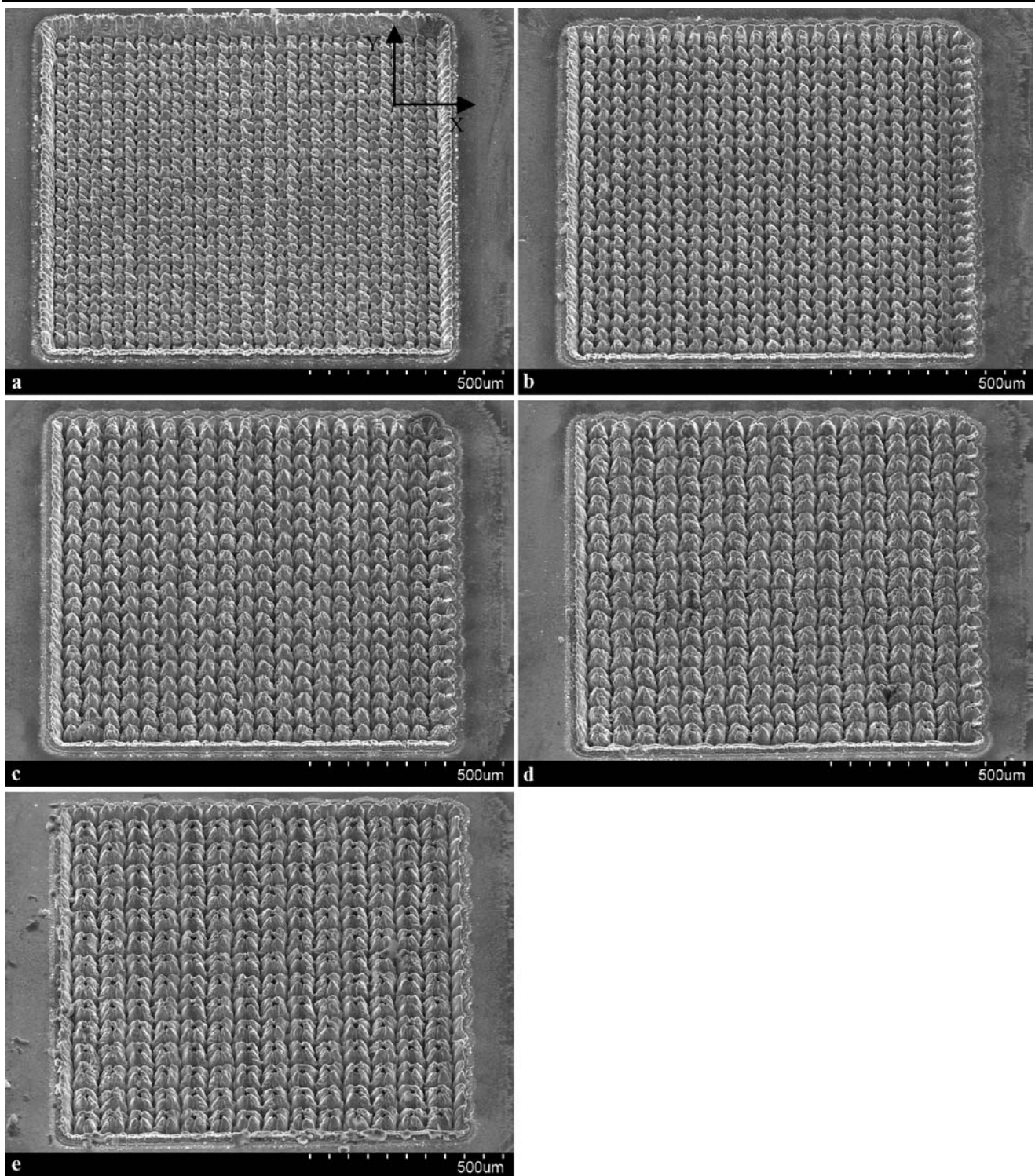


Fig. 3 SEM picture of the steel surface after laser irradiation in the crossed hatching regime (CHR). The laser scanned over the surface in two directions, X and Y , to form a grid pattern. The hatch distance was fixed between the scanned lines for each area

in both X and Y , and varied for each area from 30 μm (a) to 70 μm (e) in steps of 10 μm . The hatch distances are 30, 40, 50, 60, and 70 μm for (a), (b), (c), (d), and (e), respectively

increased from 40 μm (Fig. 3(b)) to 70 μm (Fig. 3(e)), in both X - and Y -directions. Figure 4 shows the average struc-

ture period versus the hatch distance. It follows a linear trend, hence suggesting that as the hatch distance increase

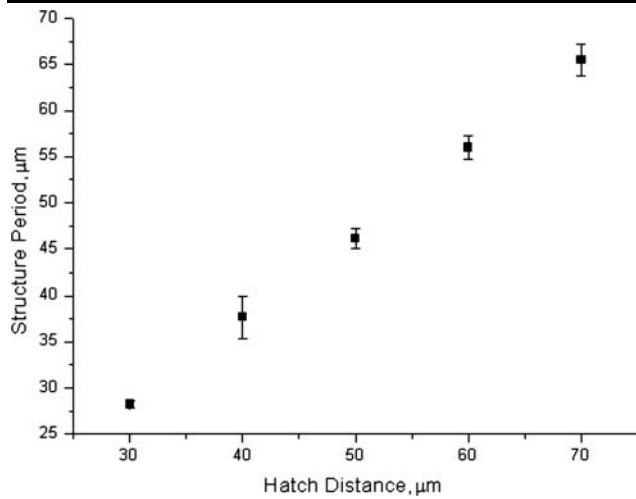


Fig. 4 Graph showing the increase of microstructure period (see Figs. 3(a)–(e)) as the hatch distance increases

(total number of pulses fired onto the target decrease) larger microstructures appear at the expense of the extinction of other, smaller ones.

Once again it was found that increasing the overlap between the scanned lines (hatch distance $< 30 \mu\text{m}$) only resulted in the substantial ablation of the material. No well-defined structures have been formed in these cases.

We consider that for the plasma produced during our high intensity nanosecond pulse laser irradiation (intensity in the order of $\sim 10^9 \text{ W/cm}^2$ and $\tau = 7 \text{ ns}$) deposition of laser energy is non-local and occurs below the critical electron density of $N_c \sim 9.7 \times 10^{20} \text{ cm}^{-3}$ (the critical electron density is taken equal to $1.1 \times 10^{21} / \lambda_l^2 \text{ cm}^{-3}$, where λ_l is the laser wavelength in microns [14]). The nonlocalised absorption of the radiation results in the heat transport to the target and hence makes accurate energy deposition difficult. The absorption of the laser radiation occurs via inverse bremsstrahlung. The duration of the ablation can be considered to be close to the duration of the laser pulse. The heat diffusion length, $l_T \sim 2(D\tau)^{1/2}$ [15], where D is the heat diffusivity (here taken to be approximately equal to $0.04 \text{ cm}^2 \text{ s}^{-1}$) and τ is the laser beam dwell time ($\tau = 7 \text{ ns}$), was calculated to be approximately $33 \mu\text{m}$. This value is fairly close to the laser spot radius on the target ($\sim 25 \mu\text{m}$). Hence, the lateral heat flow can be substantially confined.

It is proposed that the driving force behind the material removal is the pressure of the expanding ablation products which are produced at the centre of the laser beam interaction site. Owing to the high intensity and good beam quality of the source, ablation would occur at the centre of the laser beam, which is above the ablation threshold of the material. This would release an expanding volume of partially ionised plasma and some quantities of vapour. At the periphery of the beam, melting is likely occurring instead. The lifetime of the melt pool is in approximately the same order

of magnitude as the time between pulses (\sim tens of μs) [16], which will result in an interaction of the persistent melt with the pressure in the near-surface plasma/vapour layer. This will induce a hydrodynamic instability of the melt. In the absence of definite polarisation of the laser beam and spatial modulation of the radiation intensity (in our experiments, the large DOF maintained a high irradiance owing to the good beam quality of the laser), melt instability in the field of ablation plume pressure results in the growth of large-scale surface structures [17]. In the range of irradiation parameters used here (pulse duration of 7 ns and intensity in the order of 10^9 W/cm^2), the formation of these structures is induced through a spatial modulation of the pressure in the near-surface plasma layer, followed by melt outflow from pits to humps and subsequent solidification [17]. It has to be pointed out that during the lifetime of the molten phase the structures are damped due to the viscous nature of the liquid. Upon resolidification, the actual shape of the surface freezes. They then act as precursors to the formation of microcones by altering the reflectivity of the target surface, and hence introducing a non-uniform temperature distribution on the target. It can be seen from Fig. 4 that the period of the surface structures is fairly close to the distance between the adjacent traces (hatch distance). We believe that increasing the hatch distance results in the less efficient damping of the structures during the lifetime of the molten surface, with consequence of increasing the average period of the structures.

4 Summary

In conclusion, a practical route towards microstructuring of metallic surfaces is proposed. Periodic, highly organised, reproducible microstructures were formed upon pulsed laser irradiation of steel. Changing the overlap between consecutive scans of the target surface as well as scanning the laser beam in both horizontal and vertical directions resulted in the formation of arrays of microstructures with various shapes and average periods ranging from 30 to $70 \mu\text{m}$. High intensity and good beam quality of the laser source considerably facilitated the uniform processing/ablation/removal of the material.

The feasibility of using the fabricated structures for applications in microbiology and surface wettability are currently being explored, the results of which are subject of a subsequent publication.

Acknowledgements This work was conducted under the aegis of the Northwest Laser Engineering Consortium (NWLEC), funded by the Northwest Development Agency (NWDA) of the United Kingdom. NWLEC is formed as a collaboration between the University of Manchester and the University of Liverpool.

The authors wish to thank G. Broadhead of Laser Lines IM Ltd for the generous loan of the Violino laser system for the period of the experimental work.

References

1. R. Kelly, J.E. Rothenberg, Nucl. Instrum. Methods B **7/8**, 755 (1985)
2. H.U. Krebs, O. Beremert, Appl. Phys. Lett. **62**, 2341 (1993)
3. E. György, A. Pérez del Pino, P. Serra, J.L. Morenza, J. Mater. Res. **18**, 2228 (2003)
4. V. Oliveira, R. Vilar, J. Mater. Res. **18**, 1123 (2003)
5. A.J. Pedraza, J.D. Fowlkes, D.H. Lowndes, Appl. Phys. Lett. **74**, 2322 (1999)
6. T.H. Her, R.F. Finlay, C. Wu, S. Deliwala, E. Manzur, Appl. Phys. Lett. **73**, 1673 (1998)
7. S.I. Dolgaev, J.M. Fernandez-Pradas, J.L. Morenza, P. Serra, G.A. Shafeev, Appl. Phys. A **83**, 417 (2006)
8. E. György, A. Pérez del Pino, P. Serra, J.L. Morenza, J. Mater. Res. **20**, 62 (2005)
9. A.J. Pedraza, J.D. Fowlkes, D.H. Lowndes, Appl. Phys. Lett. **77**, 3018 (2000)
10. S.R. Foltyn, in *Pulsed Laser Deposition of Thin Films*, ed. by D.B. Christy, G.K. Huber (Wiley, New York, 1994)
11. N. Mirhosseini, P.L. Crouse, M.J.J. Schmidt, L. Li, D. Garrod, Appl. Surf. Sci. **253**, 7738 (2007)
12. W.M. Steen, *Laser Material Processing*, 3rd edn. (Springer, London, 2003)
13. A. Dupont, P. Caminat, P. Bournot, J.P. Gauchon, J. Appl. Phys. **78**, 2022 (1995)
14. C. Momma, B.N. Chichkov, S. Nolte, F. von Alvensleben, A. Tunnermann, H. Welling, B. Wellegenhausen, Opt. Commun. **129**, 134 (1996)
15. D. Bäuerle, *Laser Processing and Chemistry*, 3rd edn. (Springer, Berlin, 2000)
16. Z. Kantor, Zs. Geretovszky, T. Szorenyi, Appl. Surf. Sci. **154–155**, 78 (2000)
17. A.B. Brailovsky, A.B. Ezersky, I.A. Dorofeev, V.A. Ermakov, V.I. Luchin, V.E. Semenov, J. Tech. Phys. **61**, 129 (1991)